Controlling Properties of Energetic Materials Using Tailored Additives

by

Shelby Taylor Noel Nicolau

A dissertation submitted in partial fulfillment
of the requirements for the degree of
Doctor of Philosophy
(Chemistry)
in the University of Michigan
2025

Doctoral Committee:

Professor Adam J. Matzger, Chair
Professor Julie Biteen
Professor Jinsang Kim
Professor Anne McNeil

Shelby T. Nicolau

snicolau@umich.edu

ORCID iD: 0000-0002-0705-8577

© Shelby T. Nicolau 2025

Dedication

For my parents, Rick and Heather Nicolau

Acknowledgements

To my family, thank you for your continued support, love, and motivation for every goal I have set out to achieve; this was a long goal, and at times difficult, but it never felt unattainable with you all cheering me on. To Professor Matzger, thank you for your support and encouragement that I can do anything I set my mind to. Thank you for pushing me (and all lab members) to be truly the best scientists that we can be and setting the bar for excellence quite high, while also giving me the space to learn when some barriers to success are just mentally placed along the way. I could not have experienced a more enriching and fun PhD. To the Matzger Group, past and present, thank you for making lab one of my favorite places to be. To my SMART mentor, Claron Ridge, thank you for welcoming me into your work family and personal family, and continually showing me that research should always be both important and fun. To my undergraduate research advisor, Lucas Thompson, and life advisor, Kate Buettner, thank you for inspiring my love for chemistry and research and the pursuit of this PhD. And a special thank you to those close friends who kept me going these last five years: Yekaterina (Kate) Fyodorova, Andrew Bennett, Kristen Kelsall, Leila Foroughi, Cassidy Carey, and Courtney Ward.

Table of Contents

Dedication ii

Acknowledgements iii

List of Tables vii

List of Figures xi

List of Appendices xvii

Abstract xviii

Chapter 1 Introduction 1

1.1 Energetic Materials and Classifications 1

1.2 Primary vs. Secondary Explosives 2

1.3 The Development of Explosives 3

1.4 Connecting Explosive Performance and Sensitivity: Molecular Structure 4

1.5 Molecular Organic Solids 5

1.6 Crystal Engineering 8

1.7 A Tailored Additive Approach: Thesis Outlined 9

1.8 References 12

Chapter 2 Sensitizing Explosives Through Molecular Doping 18

2.1 Publication of Chapter 18

2.2 Introduction 18

2.3 Results and Discussion 20

2.4 Conclusion 33

2.5 Experimental Details 34

2.5.1 Sample Preparation 34
2.5.2 Two-Dimensional Powder X-ray Diffraction 34
2.5.3 Transmission Infrared Microspectroscopy 35
2.5.4 Raman Microspectroscopy 35
2.5.5 Impact Sensitivity 36
2.6 Acknowledgements 37
2.7 References 37
Chapter 3 An Evaluation of Resolution, Accuracy, and Precision in FT-IR Spectroscopy 41
3.1 Publication of Chapter 41
3.2 Introduction 41
3.3 Results and Discussion 44
3.4 Conclusion 62
3.5 Experimental Details 64
3.5.1 Sample preparation 64
3.5.2 FT-IR 64
3.6 Acknowledgements 65
3.7 References 65
Chapter 4 Controlling Energetic Crystal Morphology Using Tailored Polymeric Additives 69
4.1 Publication of Chapter 69
4.2 Introduction 69
4.3 Results and Discussion 72
4.4 Conclusion 84
4.5 Experimental Details 85
4.5.1 Materials 85
4.5.2 Crystallizations 86

4.5.3 Optical Microscopy 86
4.5.4 Single Crystal Indexing 87
4.5.5 ^{1}H NMR Spectroscopy 87
4.6 Acknowledgements 88
4.7 References 88
Chapter 5 Conclusion and Future Directions 93
5.1 References 97
Appendices 99

List of Tables

Table 3-1 Peak accuracy (cm^{-1})[Ɨ] for 9 PS NIST calibration peaks collected on four FT-IR instruments at 4 cm^{-1} spectral resolution. [Ɨ]Wavenumbers were determined in OMNIC using the standard peak picking function. 49

Table 3-2 Peak positions (cm^{-1})[Ɨ] for PS collected on a Nicolet iS50 FT-IR at variable spectral resolutions. [Ɨ]Wavenumbers were determined in OMNIC using the standard peak picking function. [ǂ]NR denotes peak that were unresolved at said resolution..... 52

Table 3-3. Peak position (cm^{-1}) as a function of resolution for PS as assessed by calculating the difference in assigned peak value from the value determined at 0.5 cm^{-1} (e.g. $\Delta 32$ cm^{-1} = $peak_{0.5cm-1} - peak_{32cm-1}$). [ǂ]NR denotes peak that were unresolved at said resolution. 52

Table 3-4 Peak positions (cm^{-1})[Ɨ] for APAP collected on a Nicolet iS50 FT-IR at variable spectral resolutions. [Ɨ]Wavenumbers were determined in OMNIC using the standard peak picking function. [ǂ]NR denotes peak that were unresolved at said resolution..... 54

Table 3-5 Peak position (cm^{-1}) as a function of resolution for APAP as assessed by calculating the difference in assigned peak value from the value determined at 0.5 cm^{-1} (e.g. $\Delta 32$ cm^{-1} = $peak_{0.5cm-1} - peak_{32cm-1}$). [ǂ]NR denotes peak that were unresolved at said resolution. 54

Table 3-6 Peak positions (cm^{-1})[Ɨ] of PS bands collected on a Nicolet iS50 FT-IR at variable spectral resolutions. [Ɨ]Wavenumbers were determined in OMNIC using the standard peak picking function. *Peak pick value varies noticeably from the center of the peak. 60

Table 3-7 Peak position (cm^{-1})[Ɨ] as a function of resolution for PS bands collected on a Nicolet iS50 FT-IR, as assessed by calculating the difference in assigned peak value from the value determined at 0.5 cm^{-1} (e.g. $\Delta 32$ cm^{-1} = $peak_{0.5cm-1} - peak_{32cm-1}$). 61

Table B-1 Peak accuracy (cm^{-1}) for 9 PS NIST calibration peaks collected on four instruments at 4 cm^{-1} spectral resolution. Analysis was completed in the native instrument software using standard peak-picking parameters. [a]NIST values from traceability document provided in Supplementary Reference (1). 104

Table B-2 Peak positions (cm^{-1})[Ɨ] for PS collected on a Bruker Alpha II FT-IR at variable spectral resolutions. [Ɨ]Wavenumbers were determined in OMNIC using the standard peak picking function. [ǂ]NR denotes peak that were unresolved at said resolution..... 106

Table B-3 Peak position (cm^{-1})[Ɨ] as a function of resolution for PS collected on a Bruker Alpha II FT-IR, as assessed by calculating the difference in assigned peak value from the value

determined at 2 cm^{-1} (e.g. Δ32 cm^{-1} = $peak_{2cm-1}$ – $peak_{32cm-1}$). ǂSee Table B-2 for raw data. ǂNR denotes peak that were unresolved at said resolution. 106

Table B-4 Peak positions (cm^{-1})ǂ of PS collected on a PerkinElmer Frontier FT-IR at variable spectral resolutions. ǂWavenumbers were determined in OMNIC using the standard peak picking function. ǂNR denotes peak that were unresolved at said resolution..... 108

Table B-5 Peak position (cm^{-1})ǂ as a function of resolution for PS collected on a PerkinElmer Frontier FT-IR, as assessed by calculating the difference in assigned peak value from the value determined at 0.5 cm^{-1} (e.g.Δ32 cm^{-1} = $peak_{0.5cm-1}$ – $peak_{32cm-1}$). ǂSee Table B-4 for raw data. ǂNR denotes peak that were unresolved at said resolution. 108

Table B-6 Peak positions (cm^{-1})ǂ of PS collected on a Shimadzu IRTracer-100 FT-IR at variable spectral resolutions. ǂWavenumbers were determined in OMNIC using the standard peak picking function. ǂNR denotes peak that were unresolved at said resolution. 110

Table B-7 Peak position (cm^{-1})ǂ as a function of resolution for PS collected on a Shimadzu IRTracer-100 FT-IR, as assessed by calculating the difference in assigned peak value from the value determined at 0.5 cm^{-1} (e.g. Δ16 cm^{-1} = $peak_{0.5cm-1}$ – $peak_{16cm-1}$). ǂSee Table B-6 for raw data. ǂNR denotes peak that were unresolved at said resolution. 110

Table B-8 Peak positions (cm^{-1})ǂ of APAP collected on a Bruker Alpha II FT-IR at variable spectral resolutions. ǂWavenumbers were determined in OMNIC using the standard peak picking function. ǂNR denotes peak that were unresolved at said resolution..... 112

Table B-9 Peak position (cm-1)ǂ as a function of resolution for APAP collected on a Bruker Alpha II FT-IR, as assessed by calculating the difference in assigned peak value from the value determined at 2 cm^{-1} (e.g. Δ32 cm^{-1} = $peak_{2cm-1}$ – $peak_{32cm-1}$). ǂSee Table B-8 for raw data. ǂNR denotes peak that were unresolved at said resolution. 112

Table B-10 Peak positions (cm^{-1})ǂ of APAP collected on a PerkinElmer Frontier FT-IR at variable spectral resolutions. ǂWavenumbers were determined in OMNIC using the standard peak picking function. ǂNR denotes peak that were unresolved at said resolution. 114

Table B-11 Peak position (cm^{-1})ǂ as a function of resolution for APAP collected on a PerkinElmer Frontier FT-IR, as assessed by calculating the difference in assigned peak value from the value determined at 0.5 cm^{-1} (e.g. Δ32 cm^{-1} = $peak_{0.5cm-1}$ – $peak_{32cm-1}$). ǂSee Table B-10 for raw data. ǂNR denotes peak that were unresolved at said resolution..... 114

Table B-12 Peak positions (cm^{-1})ǂ of APAP collected on a Shimadzu IRTracer-100 FT-IR at variable spectral resolutions. ǂWavenumbers were determined in OMNIC using the standard peak picking function. ǂNR denotes peak that were unresolved at said resolution. *Denotes water interference..... 116

Table B-13 Peak position (cm^{-1})ǂ as a function of resolution for APAP collected on a Shimadzu IRTracer-100 FT-IR, as assessed by calculating the difference in assigned peak value from the value determined at 0.5 cm^{-1} (e.g.Δ16 cm^{-1} = $peak_{0.5cm-1}$ – $peak_{16cm-1}$). ǂSee Table B-12 for raw data. ǂNR denotes peak that were unresolved at said resolution. *Denotes water interference. . 116

Table B-14 Peak positions (cm^{-1})[Ɨ] of PS collected on a Bruker Alpha II FT-IR at variable spectral resolutions. [Ɨ]Wavenumbers were determined in OPUS using the standard peak picking function. [ǂ]NR denotes peak that were unresolved at said resolution..... 117

Table B-15 Peak position (cm^{-1})[Ɨ] as a function of resolution for PS collected on a Bruker Alpha II FT-IR, as assessed by calculating the difference in assigned peak value from the value determined at 2 cm^{-1} (e.g. $\Delta 32\ cm^{-1} = peak_{2cm-1} - peak_{32cm-1}$). [Ɨ]See Table B-14 for raw data. [ǂ]NR denotes peak that were unresolved at said resolution. 117

Table B-16 Peak positions (cm^{-1})[Ɨ] of PS collected on a PerkinElmer Frontier FT-IR at variable spectral resolutions. [Ɨ]Wavenumbers were determined in Spectrum using the standard peak picking function. [ǂ]NR denotes peak that were unresolved at said resolution..... 118

Table B-17 Peak position (cm^{-1})[Ɨ] as a function of resolution for PS collected on a PerkinElmer Frontier FT-IR, as assessed by calculating the difference in assigned peak value from the value determined at 0.5 cm^{-1} (e.g. $\Delta 32\ cm^{-1} = peak_{0.5cm-1} - peak_{32cm-1}$). [Ɨ]See Table B-16 for raw data. [ǂ]NR denotes peak that were unresolved at said resolution. 118

Table B-18 Peak positions (cm^{-1})[Ɨ] of PS collected on a Shimadzu IRTracer-100 FT-IR at variable spectral resolutions. [Ɨ]Wavenumbers were determined in LabSolutions using the standard peak picking function. [ǂ]NR denotes peak that were unresolved at said resolution. 119

Table B-19 Peak position (cm^{-1})[Ɨ] as a function of resolution for PS collected on a Shimadzu IRTracer-100 FT-IR, as assessed by calculating the difference in assigned peak value from the value determined at 0.5 cm^{-1} (e.g. $\Delta 16\ cm^{-1} = peak_{0.5cm-1} - peak_{16cm-1}$). [Ɨ]See Table B-18 for raw data. [ǂ]NR denotes peak that were unresolved at said resolution. 119

Table B-20 Peak positions (cm^{-1})[Ɨ] of APAP collected on a Bruker Alpha II FT-IR at variable spectral resolutions. [Ɨ]Wavenumbers were determined in OPUS using the standard peak picking function. [ǂ]NR denotes peak that were unresolved at said resolution..... 120

Table B-21 Peak position (cm^{-1})[Ɨ] as a function of resolution for APAP collected on a Bruker Alpha II FT-IR, as assessed by calculating the difference in assigned peak value from the value determined at 0.5 cm^{-1} (e.g. $\Delta 32\ cm^{-1} = peak_{0.5cm-1} - peak_{32cm-1}$). [Ɨ]See Table B-20 for raw data. [ǂ]NR denotes peak that were unresolved at said resolution. 120

Table B-22 Peak positions (cm^{-1})[Ɨ] of APAP collected on a PerkinElmer Frontier FT-IR at variable spectral resolutions. [Ɨ]Wavenumbers were determined in Spectrum using the standard peak picking function. [ǂ]NR denotes peak that were unresolved at said resolution. 121

Table B-23 Peak position (cm^{-1})[Ɨ] as a function of resolution for APAP collected on a PerkinElmer Frontier FT-IR, as assessed by calculating the difference in assigned peak value from the value determined at 0.5 cm^{-1} (e.g. $\Delta 32\ cm^{-1} = peak_{0.5cm-1} - peak_{32cm-1}$). [Ɨ]See Table B-22 for raw data. [ǂ]NR denotes peak that were unresolved at said resolution..... 121

Table B-24 Peak positions (cm^{-1})[Ɨ] of APAP collected on a Shimadzu IRTracer-100 FT-IR at variable spectral resolutions. [Ɨ]Wavenumbers were determined in LabSolutions using the

standard peak picking function. ǂNR denotes peak that were unresolved at said resolution. *Denotes water interference. 122

Table B-25 Peak position (cm^{-1})ǂ as a function of resolution for APAP collected on a Shimadzu IRTracer-100 FT-IR, as assessed by calculating the difference in assigned peak value from the value determined at 0.5 cm^{-1} (e.g. $\Delta 16cm^{-1} = peak_{0.5cm-1} - peak_{16cm-1}$). ǂSee Table B-24 for raw data. ǂNR denotes peak that were unresolved at said resolution. *Denotes water interference. . 122

Table B-26 Peak positions (cm^{-1})ǂ of PS bands collected on a Bruker Alpha II FT-IR at variable spectral resolutions. ǂWavenumbers were determined in OMNIC using standard peak picking function. ǂNR denotes peak that were unresolved at said resolution. *Peak pick value varies noticeably from the center of the peak..... 124

Table B-27 Peak position (cm^{-1})ǂ as a function of resolution for PS bands collected on a Bruker Alpha II FT-IR, as assessed by calculating the difference in assigned peak value from the value determined at 2 cm^{-1} (e.g. $\Delta 32$ $cm^{-1} = peak_{2cm-1} - peak_{32cm-1}$). ǂSee Table B-26 for raw data. ǂNR denotes peak that were unresolved at said resolution. *Peak pick value varies noticeably from the center of the peak. 125

Table B-28 Peak positions (cm^{-1})ǂ of PS bands collected on a Bruker Alpha II FT-IR at variable spectral resolutions. ǂWavenumbers were determined in OPUS using standard peak picking function. ǂNR denotes peak that were unresolved at said resolution.*Peak pick value varies noticeably from the center of the peak..... 126

Table B-29 Peak position (cm^{-1})ǂ as a function of resolution for PS bands collected on a Bruker Alpha II FT-IR, as assessed by calculating the difference in assigned peak value from the value determined at 2 cm^{-1} (e.g. $\Delta 32$ $cm^{-1} = peak_{2cm-1} - peak_{32cm-1}$). ǂSee Table B-28 for raw data. ǂNR denotes peak that were unresolved at said resolution. *Peak pick value varies noticeably from the center of the peak. 127

Table B-30 Peak position (cm^{-1})ǂ of PS bands collected on a Nicolet iS50 FT-IR at variable scan numbers. Spectral resolution was 4 cm^{-1}. ǂWavenumbers were determined in OMNIC using the standard peak picking function..... 128

List of Figures

Figure 1.1 Energetic materials are classified into three categories: propellants, pyrotechnics, and explosives. Some factors that influence their classification include reaction rate and combustive behavior (deflagration vs. detonation). 2

Figure 1.2 Common secondary explosives (representing major classes) are PETN (nitrate esters), RDX (nitramines), and TNT (nitroaromatics). Common primary explosives are lead styphnate and lead azide. 3

Figure 1.3 The development of explosives has seen improvement of sensitivity and performance since earliest discovery, but the introduction of new, competitive materials has become stagnant. Efforts recently have looked to cocrystallization and tailored additives (this thesis) for developing materials with improved properties. 4

Figure 1.4 A solid that assembles with long-range order is defined as crystalline, whereas short-range order is defined as amorphous. Regimes also exist in between with varying degrees of crystallinity, or mixed phase. 5

Figure 1.5 A molecule can assemble into multiple unique crystal forms, a phenomenon known as polymorphism. 6

Figure 1.6 Crystal morphology can impact properties directly related to energetic materials, like sensitivity, or more broadly applicable like packing density and processability. 7

Figure 1.7 Two or more components can be assembled in a stoichiometric ratio into a single crystal that is held together by intermolecular interactions. These interactions are comprised of structural units termed “supramolecular synthons” that promote molecular recognition. 8

Figure 1.8 A solute can be crystallized in the presence of additive to form a crystal where the additive either adsorbs onto the surface or incorporates into the lattice. 9

Figure 2.1 Increased sensitivity to impact was imparted to three melt-castable explosives by molecular doping with cyanuric triazide. 18

Figure 2.2 a) During crystallization, a dopant can be inserted into a host crystal in low concentrations without impacting the packing of the crystal lattice (molecular doping). b) CTA (red box) was evaluated for the ability to sensitize a series of melt-castable host energetics (grey box). 20

Figure 2.3 a) PXRD patterns of pure TNT, pure CTA, and various loadings of CTA into TNT (grey boxes emphasize unique diffraction peaks of CTA). b) A maximum molecular dopant

loading is extrapolated based on peak area ratios of the two CTA peaks to a TNT reference peak. 22

Figure 2.4 PXRD patterns of pure DNAN, pure CTA, and various loadings of CTA into DNAN (grey boxes emphasize unique diffraction peaks of CTA). The inset image represents maximum dopant loading extrapolation based on peak area ratios of three CTA peaks to a DNAN reference peak..... 23

Figure 2.5 PXRD patterns of pure TNAZ, pure CTA, and various loadings of CTA into TNAZ (grey boxes emphasize unique diffraction peaks of CTA). The inset image represents maximum dopant loading extrapolation based on peak area ratios of three CTA peaks to a TNAZ reference peak. 24

Figure 2.6 Transmission infrared spectroscopy collection mode of TNT (host compound) saturates mid-infrared regions when compared to an ATR collection. CTA is an excellent model dopant because it possesses strong and unique vibrational stretches in the overtone region of the host which are not saturated in transmission mode. 25

Figure 2.7 a) TNT melt cast with 1% CTA mapped using transmission IR microspectroscopy to verify CTA incorporation into host. b) Peak ratio profiling is used to check for CTA present throughout the entire sample. The uniform color distribution of the profile represents a uniform peak area ratio of the CTA region of interest to a TNT overtone (highlighted in grey boxes). c) A 1% spectrum reveals shifts in CTA primary bands that support molecular doping. 26

Figure 2.8 DNAN melt cast with 2% CTA is mapped using transmission IR microspectroscopy to verify CTA incorporation into host. Peak ratio profiling is used to check for CTA present throughout the entire sample. The uniform color distribution of the profile represents uniform peak area ratios of the CTA region of interest to DNAN overtone (highlighted in grey boxes). A representative 2% spectrum is analyzed for shifts in CTA primary bands to further support molecular doping. 27

Figure 2.9 TNAZ melt cast with 1% CTA is mapped using transmission IR microspectroscopy to verify CTA incorporation into host. Peak ratio profiling is used to check for CTA present throughout the entire sample. The uniform color distribution of the profile represents uniform peak area ratios of the CTA region of interest to TNAZ overtones (highlighted in grey boxes). A representative 1% spectrum is analyzed for shifts in CTA primary bands to further support molecular doping. 27

Figure 2.10 a) Raman spectra of TNT vs CTA, with the peak of interest highlighted by a grey box. b) Mapping of 1% vs. 10% CTA in TNT shows distribution of CTA (red) across melt. c) Representative spectra are shown for each loading based on regions of average CTA signal (black) and high CTA signal (red). 28

Figure 2.11 Raman spectra of TNAZ vs CTA, with peak of interest highlighted by a grey box. Mapping of 1% vs. 10% CTA in TNAZ shows distribution of CTA across melt. Representative spectra are shown for each loading based on regions of average CTA signal (color-coded black) and high CTA signal (color-coded red). Additional CTA peaks (*) can be found in higher concentration areas. 30

Figure 2.12 Raman spectra of DNAN vs CTA, with peak of interest highlighted by a grey box. Mapping of 1% vs. 2% vs. 10% CTA in DNAN shows distribution of CTA across melt. Representative spectra are shown for each loading based on regions of average CTA signal (color-coded black) and high CTA signal (color-coded red). Additional CTA peaks (*) can be found in higher concentration areas. 31

Figure 2.13 Impact sensitivity of pure vs. CTA-loaded compounds reported as Dh50, the drop height where there is a 50% probability of detonation. 33

Figure 3.1 An experimental study of polystyrene and acetaminophen determined resolution and instrument variation have minor effects on well-resolved peak positions. 41

Figure 3.2 Spectral resolution effect on resolving polystyrene (PS) peaks collected by transmission FT-IR. (a) Full spectral window with varied spectral resolutions from 32 – 0.5 cm^{-1}. Boxes highlight zoomed in regions for b and c. (b) PS region with poorly resolved peaks at low resolutions (32, 16 cm^{-1}). (c) PS region with well resolved peaks at all resolutions. 46

Figure 3.3 Spectral resolution effect (32 – 0.5 cm^{-1}) on resolving acetaminophen (APAP) peaks useful for polymorph differentiation. One (a) single band at 1610 cm^{-1} (denoted by *) and (b) three resolved bands at 1260, 1243, and 1226 cm^{-1} denote Form I, only accomplished at spectral resolutions of 8 cm^{-1} or higher. 47

Figure 3.4 Transmission FT-IR of PS collected on a Shimadzu IRTracer-100 of a saturated peak with sidelobe generation at spectral resolutions higher than 8 cm^{-1}, increasing error in peak position at ~3025 cm^{-1}. 49

Figure 3.5 Transmission FT-IR spectra of PS collected on a Nicolet iS50 with varied spectral resolutions from 32 – 0.5 cm^{-1}. Numbering denotes peaks in analysis. 51

Figure 3.6 Transmission FT-IR spectra of APAP collected on a Nicolet iS50 with varied spectral resolutions from 32 – 0.5 cm^{-1}. Numbering denotes peaks in analysis. 53

Figure 3.7 Region of intense water vapor interference with APAP bands. Data was collected on a Shimadzu IRTracer-100 FT-IR. 56

Figure 3.8 Spectral resolution effect (32 – 0.5 cm^{-1}) on resolving saturated PS peaks (highlighted with boxes). Transmission FT-IR spectra were collected on the Nicolet iS50. 58

Figure 3.9 ATR FT-IR spectra of PS collected on a Nicolet iS50 with varied spectral resolutions from 32 – 0.5 cm^{-1}. Numbering denotes peaks in analysis. 59

Figure 3.10 Increased spectral resolution can lead to deceptive shifts in peak positions for saturated bands using the standard peak picking function. This is evident by deviation between the picked values and the apparent center of PS peak 14 near ~ 700 cm^{-1}. Additionally, scrutiny of peak shape can also be needed at increased spectral resolution to discern when an apparent band is likely two overlapping peaks, as evident with Peak 13 near ~755 cm^{-1}. Transmission FT-IR plot shown in OMNIC. 62

Figure 3.11 In addition to resolution, peak position variation can be influenced by (a) instrument design, (b) absorbance saturation, (c) water vapor interference, and (d) spectral noise. 63

Figure 4.1 Polymeric additives were designed to interact face selectively to control the shape of several energetics crystals. 69

Figure 4.2 Chemical structures of selected (a) explosives and (b) additives. 72

Figure 4.3 BFDH morphology of β-HMX. Computed with Mercury software 2024.1.0 (Build 401958) using cif from reference code OCHTET24. 73

Figure 4.4(a) Morphology control of HMX with the additive poly(vinylpyrrolidone) (PVP) in acetonitrile. (b) Single crystal indexing of HMX morphologies. (c) Proposed PVP-crystal face interactions, demonstrated with (011) slice. 75

Figure 4.5 Proton NMR indicates that no polymer (P4VP) is detected within the crystal lattice of the morphology-modified energetic (HNFX) crystals upon dissolution of the highest additive concentration tested..... 76

Figure 4.6 (a) Morphology control of HNFX with the additive poly(vinylpyrrolidone) (PVP) in ethanol. (b) Single crystal indexing of HNFX morphologies. (c) Proposed PVP-crystal face interactions, demonstrated with (2-10) slice. 77

Figure 4.7 Tethering the pyrrolidone moiety to a polymeric backbone imparts similar morphology changes at lower concentrations compared to the monomeric form. 77

Figure 4.8 Electrostatic potential maps illustrating increased fluorine content in a structure provides more neutral charge character, improving halogen-bonding capability. Spartan '24 v1.2.0 was used to calculate the electrostatic potential map. Equilibrium geometries were optimized by Density Functional Theory (B3LYP) calculations with the 6-31G* basis set. 78

Figure 4.9 (a) Morphology control of HNFX with the additive poly(4-vinylpyridine) (P4VP) in either ethanol (EtOH) or benzyl alcohol (BnOH). (b) Single crystal indexing of HNFX morphologies. (c) Proposed P4VP-crystal face interactions, demonstrated with (1-1-1) slice. ... 79

Figure 4.10 BFDH morphology prediction of HNFX (JURHOT) packed with space-filling molecules. We hypothesize that the preferential interaction of the polymer (P4VP) to the c-axis is likely due to the accessibility of the difluoramines, extending further on the crystal faces and covering a larger relative amount of the crystal face compared to competing interactions. 79

Figure 4.11 HNFX retained its needle morphology when recrystallized from benzyl alcohol with polystyrene additive. 80

Figure 4.12 (a) Morphology control of NQ with the additive poly(2-vinylpyridine N-oxide) (P2VPNO) in water. (b) Single crystal indexing of NQ morphologies. (c) Proposed P2VPNO-crystal face interactions, demonstrated with (111) slice. 82

Figure 4.13 The thin HNFX control needle was modified to a much thicker needle, changing the aspect ratio when recrystallized from benzyl alcohol with P2VPNO. 83

Figure 4.14 (a) Morphology control of HNFX with the additive poly(2-vinylpyridine N-oxide) (P2VPNO) in ethanol. (b) Single crystal indexing of HNFX morphologies. (c) Proposed P2VPNO-crystal face interactions, demonstrated with (110) slice, to emphasize low concentration change. 83

Figure 4.15 Electrostatic potential maps for the motifs of poly(2-vinylpyridine N-oxide) and poly(4-vinylpyridine) (demonstrated as pyridine N-oxide and pyridine, respectively) illustrate a similar propensity for halogen-bonding with fluorine based on the regions of very positive and very negative potentials. Spartan '24 v1.2.0 was used to calculate the electrostatic potential map. Equilibrium geometries were optimized by Density Functional Theory (B3LYP) calculations with the 6-31G* basis set. 84

Figure 5.1 Potential primary explosive dopants. 94

Figure A.1 Secondary energetics crystallized from melt. Each adopts a known form as shown by comparison to simulated PXRD patterns (peak setting FWHM: 0.2) corresponding to the Cambridge Structural Database (CSD) reference codes listed. 100

Figure A.2 A representative 2D-powder pattern collected using Gandolfi moves for powders to minimize effects of preferred orientation (sample shown is 10% CTA in TNT). 1D-powder patterns were extracted using CrysAlisPro v42.75a for analysis. 101

Figure A.3 Raman mapping of 1% vs. 10% CTA in TNT that shows distribution of CTA across melt. Representative spectra are shown for each loading based on regions of average CTA signal (color-coded black) and high CTA signal (color-coded red). In addition to the main CTA peak identified in average signal (grey box), additional CTA peaks (*) can be found in higher concentration areas. 102

Figure B.1 Transmission FT-IR spectra of PS collected on a Bruker Alpha II with varied spectral resolutions from 32 – 2 cm^{-1}. Numbering denotes peaks in analysis. 105

Figure B.2 Transmission FT-IR spectra of PS collected on a PerkinElmer Frontier with varied spectral resolutions from 32 – 0.5 cm^{-1}. Numbering denotes peaks in analysis. 107

Figure B.3 Transmission FT-IR spectra of PS collected on a Shimadzu IRTracer-100 with varied spectral resolutions from 16– 0.5 cm^{-1}. Numbering denotes peaks in analysis. 109

Figure B.4 Transmission FT-IR spectra of APAP collected on a Bruker Alpha II with varied spectral resolutions from 32 – 0.5 cm^{-1}. Numbering denotes peaks in analysis. 111

Figure B.5 Transmission FT-IR spectra of APAP collected on a Perkin Elmer Frontier with varied spectral resolutions from 32 – 0.5 cm^{-1}. Numbering denotes peaks in analysis. 113

Figure B.6 Transmission FT-IR spectra of APAP collected on a Shimadzu IRTracer-100 with varied spectral resolutions from 32 – 0.5 cm^{-1}. Numbering denotes peaks in analysis. 115

Figure B.7 ATR FT-IR spectra of PS collected on a Bruker Alpha II with varied spectral resolutions from 32 – 2 cm^{-1}. Numbering denotes peaks in analysis..... 123

Figure C.1 Workflow for selecting additives, based on HMX cocrystal interaction screening. 130

Figure C.2 Two HMX cocrystals (REFCODES) with pyrrolidone-based coformers were used to select the additive poly(vinylpyrrolidone) (PVP). The shortest contacts (highlighted in blue) suggest that dominant interactions will be the additive carbonyl with the energetic ring hydrogens (CH_2) and the carbonyl-adjacent CH_2 with the energetic nitro (NO_2) group..... 130

Figure C.3 Two HMX cocrystals (REFCODES) with N-oxide-based coformers were used to select the additive poly(2-vinylpyridine N-oxide) (P2VPNO). The shortest contacts (highlighted in blue) suggest that dominant interactions will be the additive N-oxide with the energetic ring hydrogens (CH_2). Note, a third HMX/N-oxide cocrystal does exist (ETOCOH) but no coordinates are available..... 131

List of Appendices

Appendix A: *From Chapter 2* – Sensitizing Explosives Through Molecular Doping 100

A.1 Supplementary Data 100

Appendix B: *From Chapter 3* – An Evaluation of Resolution, Accuracy, and Precision in FT-IR Spectroscopy 103

B.1 Additional Experimental Details 103

B.2 Supplementary Information..... 103

B.3 Supplementary References 129

Appendix C: *From Chapter 4* – Controlling Energetic Crystal Morphology Using Tailored Polymeric Additives.....130

C.1 Supplementary Data 130

Abstract

Many of the explosives that dominate modern day energetic formulations were developed nearly 100 years ago. Despite the importance of the field, spanning from military to civilian applications like mining and construction, new energetics rarely enter the field due to rigid requirements for manufacturability and safety. Advancements in high explosives rely heavily on meeting criteria for both safety and effectiveness, balancing two general properties known as energetic sensitivity and performance. While predicting sensitivity and performance of an explosive in nontrivial, a core theme influencing them both is molecular structure. Molecular structure alone does not dictate energetic properties, but how the molecule assembles into a solid form with varying arrangements and degrees of crystallinity is influential. Assembly of molecular organic solids relies on molecular recognition, driven by intermolecular interactions. These interactions are important for controlling crystallinity, polymorphism, and crystal morphology, all of which are entangled with the control of energetic properties. Therefore, crystal engineering, which utilizes molecular recognition to design solid forms, has become an important approach to target new and/or improved materials. Specifically, additive-based strategies are useful because they can be used to promote, retard, or inhibit nucleation and growth of crystals by either a surface adsorption mechanism or through incorporation into the crystal lattice. Herein, both additive mechanisms are explored for controlling properties of energetic materials. In Chapter 2, molecular doping, where the additive is incorporated into a host crystal without altering the crystal lattice, is investigated to generate energetic materials with modified properties. With a judicious choice of dopant, increased sensitivity to impact was imparted to three melt-castable explosives by doping with cyanuric triazide. Chapter 3 introduces positional error in infrared spectroscopy peaks as being historically overestimated. Typical error at 4 cm^{-1} resolution is on the order of 1 cm^{-1}, which is important to understand when discussing additive incorporation and other nuances to crystallinity. Contrary to the current literature, resolution and

instrument variation have minor effects on peak positions, but key sources of error include band saturation, water interference and spectral noise. In Chapter 4, a design strategy for morphology control of energetic crystals is presented, using soluble polymeric additives that mimic dominant interactions observed in related cocrystals. By tethering the tailored functionality on a polymeric backbone, the additive interacts face selectively to control the crystal shape without detectable incorporation into the crystal lattice. Morphology modifications were made in both desirable (needle-to-block) and undesirable (block-to-needle) directions, offering control to study a critical feature correlated to explosive sensitivity. Overall, this thesis contributes broadly to the field of crystal engineering through the design of two additive-based crystallization strategies, while specifically demonstrating for explosives that property modification is possible; this offers new opportunities for exerting control over critical energetic materials properties, thus facilitating advancements in explosive materials discovery and fielding.

Chapter 1 Introduction

This thesis develops crystal engineering as a tool to alter materials properties, specifically within the field of energetic materials. Many of the topics and techniques discussed herein, however, are applicable more broadly to solid state chemistry. Nonetheless, this thesis bridges crystallization, supramolecular chemistry, and analytical chemistry to better understand structure-property relationships for explosives.

1.1 Energetic Materials and Classifications

By definition, an energetic material is a compound (or mixture of substances) that contains both fuel and oxidizer that reacts readily to release energy and gas. These materials result in exothermic reactions that are self-sustaining, maintained without atmospheric oxygen, and can be initiated using external stimuli (e.g., thermal, mechanical, or electrostatic ignition sources).[1] Energetic materials are classified into further categories: explosives, propellants, and pyrotechnics (Figure 1.1). While one energetic compound may be utilized across multiple categories (e.g., nitroguanidine as an explosive *and* propellant), the main difference between these categories are reaction rates and output response of either the individual compound or formulated substances. Although all exhibit strong exothermic reactions, propellants have the slowest reaction rates, followed by pyrotechnic reactions with intermediary rates, and explosives exhibiting the quickest reactions.[1] Chemical reactions may result in a deflagration, where the reaction is presented as a flame that propagates at less than the speed of sound, as is often the case for propellants. Explosives, however, undergo conditions that transition a deflagration into a

detonation, where the reaction is propagated through the material with a shock-wave that reaches faster than the speed of sound for the given medium; this type of event is known as a deflagration-to-detonation transition (DDT). Again, pyrotechnics are associated somewhere between. Herein, the target energetic material of discussion will be explosives.

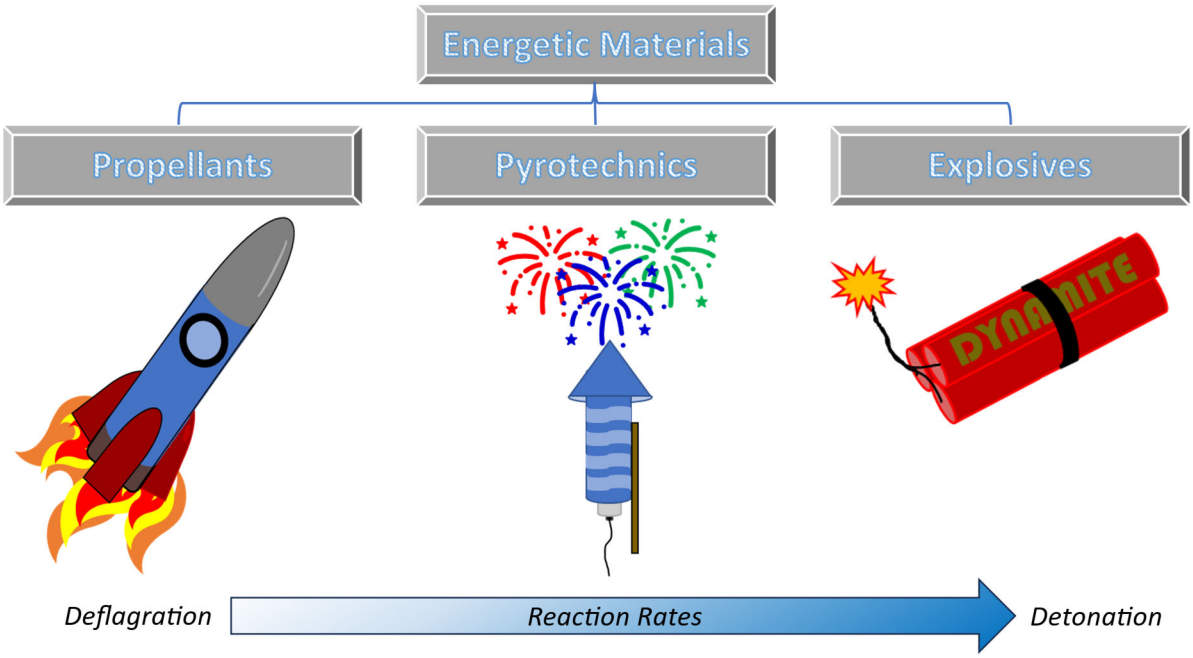


Figure 1.1 Energetic materials are classified into three categories: propellants, pyrotechnics, and explosives. Some factors that influence their classification include reaction rate and combustive behavior (deflagration vs. detonation).

1.2 Primary vs. Secondary Explosives

Explosives can be categorized further based on their transitions to detonation, the ease at which they are initiated by external stimuli (sensitivity), and performance. Primary explosives exhibit a very rapid transition to detonation compared to secondary explosives. They are also much more sensitive to external stimuli like heat, impact, friction, and electrostatic discharge. Secondary explosives, often referred to as high explosives, are much less sensitive, relying on the shockwave of a primary explosive to initiate the secondary explosive.[1] They are also generally higher performing than primary explosives and make up the bulk of an explosive formulation. Common primary and secondary explosives are shown in Figure 1.2.

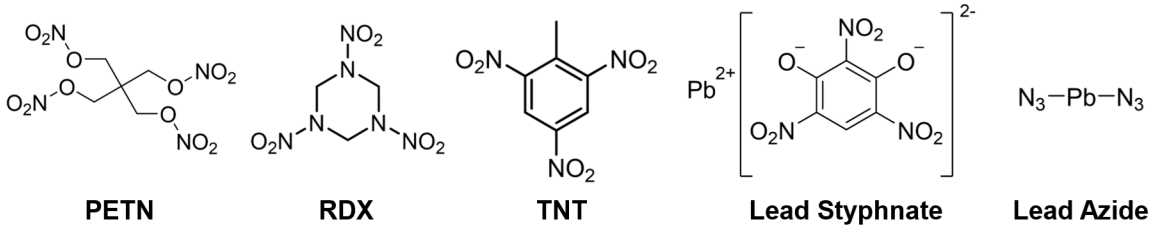


Figure 1.2 Common secondary explosives (representing major classes) are PETN (nitrate esters), RDX (nitramines), and TNT (nitroaromatics). Common primary explosives are lead styphnate and lead azide.

1.3 The Development of Explosives

Despite the pivotal role explosives play in advancing military, mining, and construction efforts, new explosives are introduced at a glacial place. While this is in part due to the rigid requirements for manufacturability and safety, current explosives in the field have actually set the bar quite high in terms of performance properties, sensitivity, and cost associated with established manufacturing infrastructure (Figure 1.3).[2] The well-known secondary energetic, 2,4,6-trinitrotoluene (TNT)[3–5], was first synthesized in 1863 and is still widely used today despite its relatively modest performance, because it can be produced at low cost and has a low melting point that allows melt casting into munitions.[6] The introduction of 1,3,5,7-tetranitro-1,3,5,7-tetrazocane (HMX) and 1,3,5-trinitro-1,3,5-triazinane (RDX) were crucial in advancing explosive performance while still maintaining secondary sensitivity levels, and to date, many explosive formulations are based on these three legacy explosives.[7] Advancements in the high explosive field will rely heavily on achieving balance between performance and sensitivity.[8–11] Additionally, for primary explosive development, balancing sensitivity with toxicity is needed, as the instability and rapid detonation characteristics of primaries are often achieved through heavy metal incorporation.[12,13]

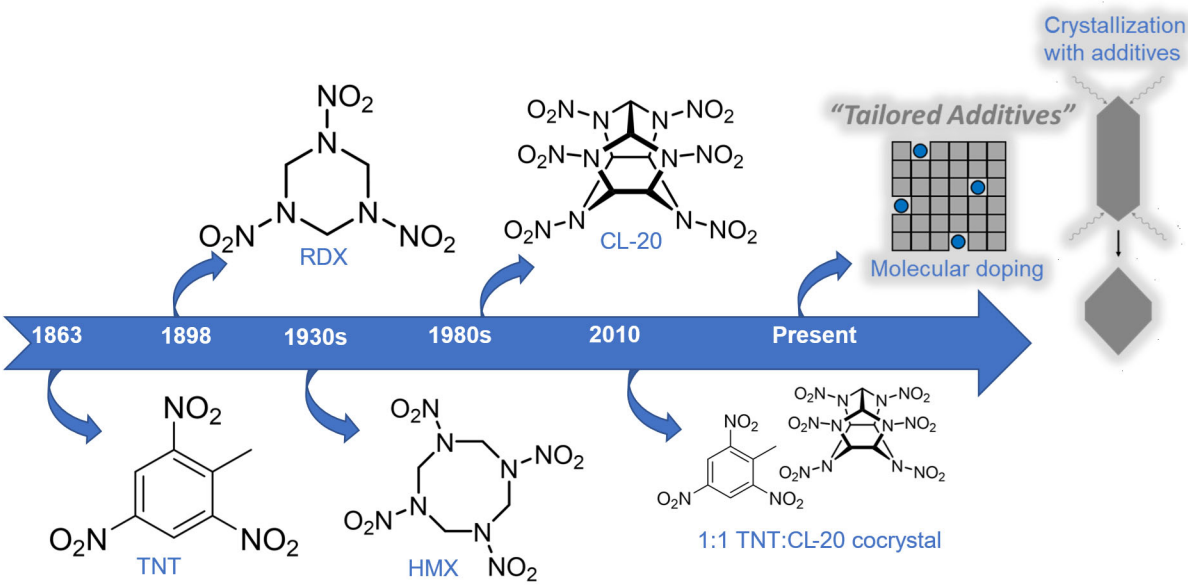


Figure 1.3 The development of explosives has seen improvement of sensitivity and performance since earliest discovery, but the introduction of new, competitive materials has become stagnant. Efforts recently have looked to cocrystallization and tailored additives (this thesis) for developing materials with improved properties.

1.4 Connecting Explosive Performance and Sensitivity: Molecular Structure

Performance is a general term used to describe the detonation events of an explosive, but it is typically quantified through characteristics termed detonation velocity, detonation pressure, and heat of explosion.[9] Sensitivity refers to the degree in which an explosive can be initiated by an external stimuli, like impact, friction, electrostatic discharge, heat, and shock.[11] Predicting performance and sensitivity of an explosive is nontrivial, because these properties are controlled by factors that span from the molecular scale (explosophores and trigger linkages)[14–16] to the mesoscale (voids and hot spots)[17,18]. While several criteria have been proposed to correlate the two (e.g. heat of explosion, oxygen balance, density)[9,10,19,20], the common theme connecting energetic properties like performance and sensitivity is molecular structure.[15,21–23]

Molecular structure emphasizes covalent atomic connectivity, and at the simplest level can influence explosive properties simply based on the design of CHNO rich frameworks and functional groups to control the ratio of fuel and oxidizer. For example, common frameworks

include aliphatic, cyclic, aromatic, and nitrogen heterocycles with nitro-, nitramine-, and azido-functional groups.[1,11,15] However, molecular structure alone does not dictate energetic properties. How the molecule assembles into a solid form (crystal packing), with varying arrangements (polymorphism) and/or degrees of crystallinity, is also influential. Herein, our discussion will pertain to molecular organic solids, although some topics may also be applicable to ionic solids.

1.5 Molecular Organic Solids

If a solid has assembled molecules in such a way that the packing forms an infinite three-dimensional array, the material is said to be crystalline. The range of that order, however, determines the degree of crystallinity; materials with short-range order are classified as amorphous as opposed to long-range order for fully crystalline materials, but there does exist a regime in between where the degree of crystallinity can vary (Figure 1.4).[24,25] The specific application typically dictates the solid form needed, with many pharmaceuticals desiring amorphous state to improve bioavailability with higher solubility and dissolution rates than the crystalline drug.[26] However, for explosives, crystalline materials are more desired for their higher density, storing more potential energy and in turn more explosive power within a defined space.[11]

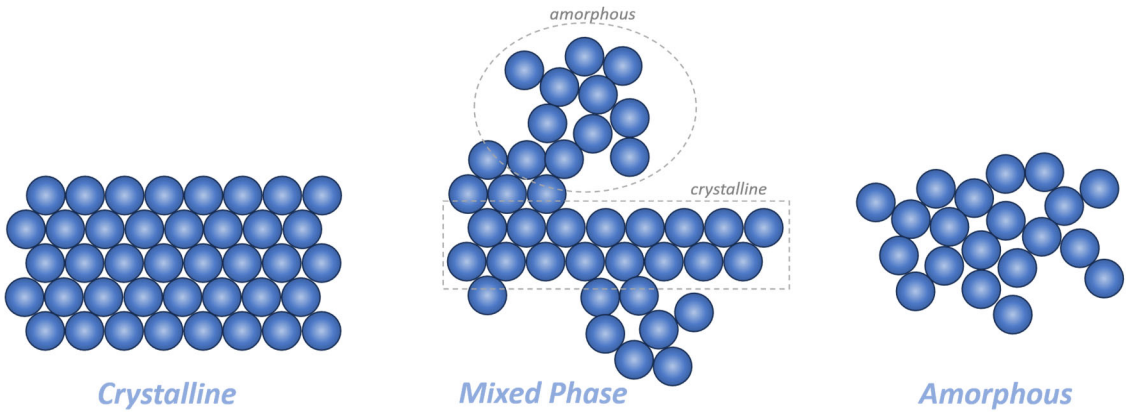


Figure 1.4 A solid that assembles with long-range order is defined as crystalline, whereas short-range order is defined as amorphous. Regimes also exist in between with varying degrees of crystallinity, or mixed phase.

Molecular crystals are held together by weak, intermolecular interactions including hydrogen bonding, van der Waals, and dipole-dipole interactions.[27] Individual molecules are arranged into specific patterns or packing motifs in the crystal lattice to minimize their free energy, driven largely by structure.[24] Some compounds can exhibit multiple unique crystal forms, or polymorphism (Figure 1.5). A polymorph exists as two or more crystalline phases that have different arrangements or conformations of the molecules in the crystal lattice.[25,28,29] As a result, physical and chemical properties are unique to each polymorph. For example, HMX occurs in three different polymorphs – α, β, and δ (and sometimes reported as four if the hydrate γ is considered) – with varying degrees of sensitivity and stability.[30,31] Often, evidence of polymorphism will be present as a compound with changes in materials properties and/or morphology, although it is important to note that multiple morphologies is not direct evidence itself of polymorphism (see Chapter 4).[32,33]

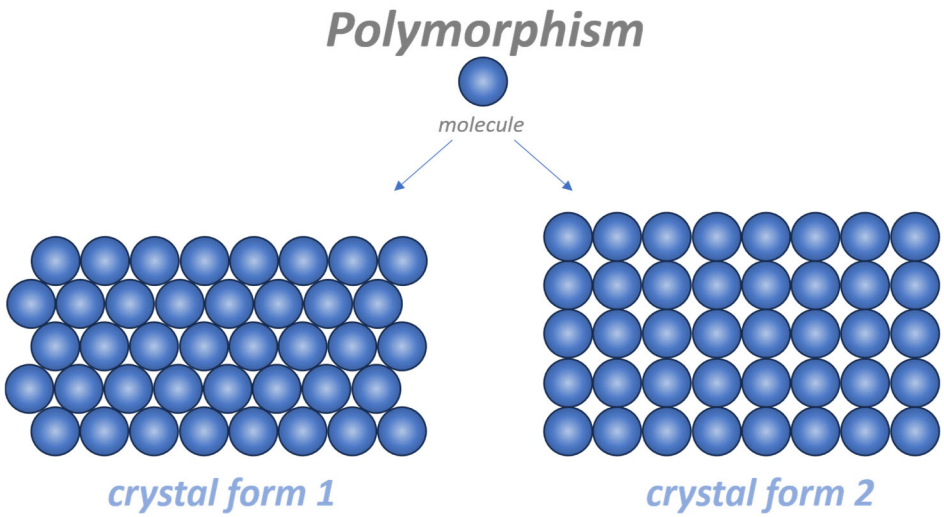


Figure 1.5 A molecule can assemble into multiple unique crystal forms, a phenomenon known as polymorphism.

While molecular structure does not directly control the morphology, or shape, of a crystal, it does influence the shape and orientation of crystal faces based on the molecular arrangement or polymorph. Morphology is determined by the relative growth rates of faces

exposed on the crystal surface and is defined by the slowest growing faces.[24,34] Mathematical modeling is a useful tool for predicting crystal morphology, with several models utilized in the field (Bravais-Friedel-Donnary-Harker (BFDH), Attachment Energy (AE), etc.) built around important factors like growth kinetics, surface energy, and adsorption layers.[35] However, it is difficult to fully replicate the complexity of crystal growth and nucleation when accounting for both kinetics and thermodynamics, as well as many external factors (complex solvent systems, impurities, etc.) present in the crystallization. Experimentally, crystal morphology is commonly controlled by employing changes in solvent, temperature, and supersaturation, with the principle that growth rates are modified by solvation.[34] Understanding how to engineer a crystal of specific morphology is useful for controlling not only the entangled molecular properties, sensitivity being most notable among these, but also properties related to processability, flowability, and packing density which are relevant to all material properties (Figure 1.6). As a result, crystal engineering has become an increasingly important field to better understand in general how crystal structures emerge from molecular structure and what techniques can be used to engineer crystals with new properties.[27]

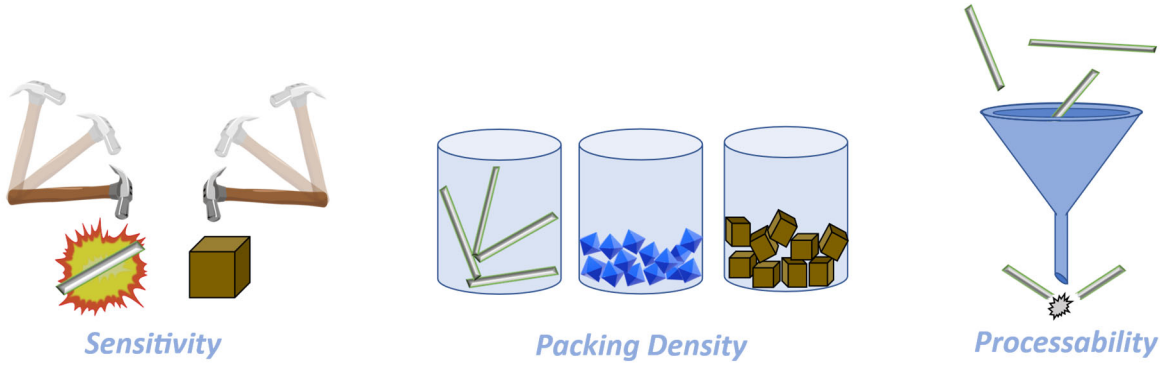


Figure 1.6 Crystal morphology can impact properties directly related to energetic materials, like sensitivity, or more broadly applicable like packing density and processability.

1.6 Crystal Engineering

The basis for crystal engineering strategies is grounded from molecular structure and intermolecular interactions. To approximate how these factors influence crystal growth from the molecular level, "supramolecular synthons" are often used. Supramolecular synthons are structural units that are formed by likely intermolecular interactions.[27,36] This is a process based on molecular recognition, and there exists a substantial body of literature for traditionally successful synthons, largely driven by hydrogen bonding.[36,37] Application of this synthon approach is utilized when engineering crystals through cocrystallization: a strategy that assembles multicomponent molecular crystals in defied stoichiometric ratios (Figure 1.7).[38] Pharmaceutical cocrystallization has seen extensive improvements to physiochemical properties (stability, solubility, bioavailability, etc.)[38–44], exploiting common motifs derived from carboxylic acids, amides, and alcohols. Cocrystals have recently been applied in the field of energetic materials, with successful modifications to sensitivity, stability, hygroscopicity, and performance[45–57]; however, this process follows a much more trial-and-error approach given that these compounds lack traditionally successful synthons for hydrogen bonding.[58–60]

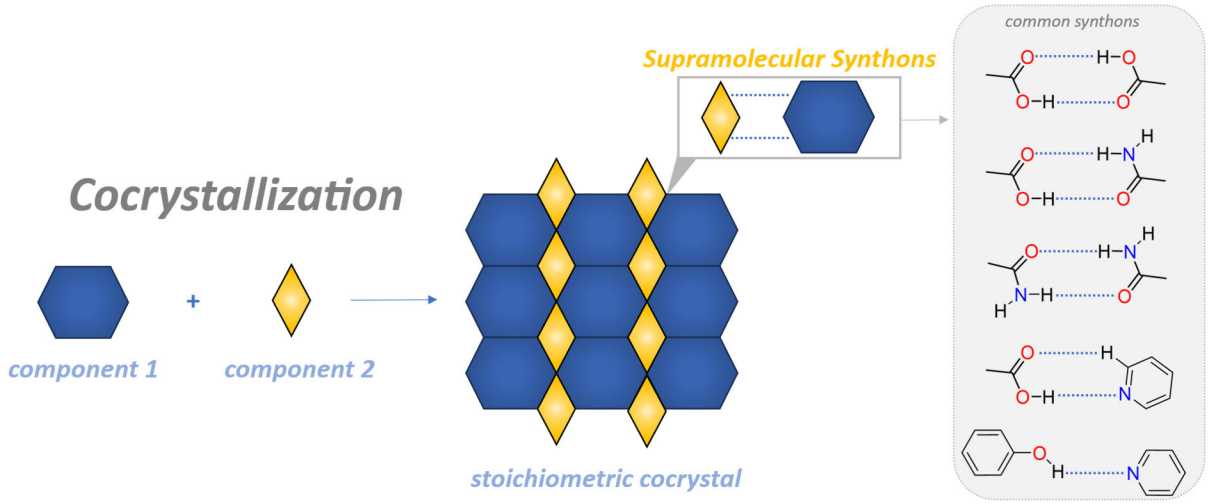


Figure 1.7 Two or more components can be assembled in a stoichiometric ratio into a single crystal that is held together by intermolecular interactions. These interactions are comprised of structural units termed "supramolecular synthons" that promote molecular recognition.

Continuing the theme of molecular recognition, additive-based strategies have also proven useful for engineering crystals with new properties because they can promote, retard, or inhibit nucleation and growth.[61] Crystallization with additives usually proceeds with either a surface adsorption mechanism or lattice incorporation (Figure 1.8).[62] The latter example is often described as an impurity incorporation if introduced unintentionally (through reaction byproducts, contamination, etc.).[24,63,64] However, intentionally doping crystals with specific molecules in the lattice is a useful strategy in semiconductor materials chemistry to modify conductivity[65,66] and may be extensible to other fields with tuning of dopant choice. Additives used to target the surface-directed mechanism can be used in both soluble and insoluble forms. Insoluble additives act like scaffolds or templates for crystal growth but generally limit interactions to one crystal face (e.g. polymer-induced heteronucleation)[67–70], whereas soluble additives[71–79] have the potential to access more faces, particularly when polymeric additives are used over small molecules.

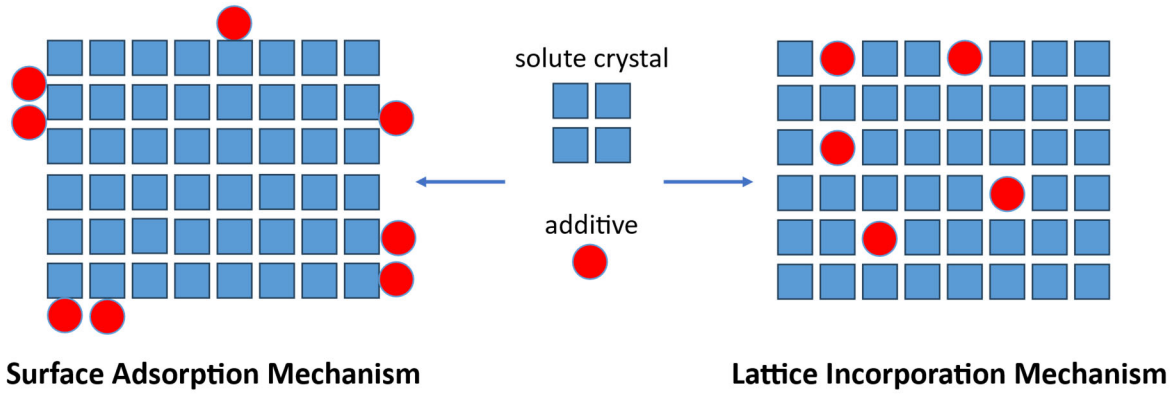


Figure 1.8 A solute can be crystallized in the presence of additive to form a crystal where the additive either adsorbs onto the surface or incorporates into the lattice.

1.7 A Tailored Additive Approach: Thesis Outlined

Herein, additive-based crystallization strategies are utilized to control energetic properties including morphology, packing density, and sensitivity. These crystal engineering successes are

realized by tailoring the additive to the molecular structure and/or desired properties of the energetic.

In *Chapter 2*, an impact-sensitive primary explosive, cyanuric triazide (CTA), was selected as the dopant to test if less impact sensitive secondary explosives could gain increased sensitization to impact when CTA is inserted into their crystal lattices.[80] Molecular doping was successful in sensitizing three melt-castable energetics: 2,4,6-trinitrotoluene (TNT), 2,4-dinitroanisole (DNAN), and 1,3,3-trinitroazetidine (TNAZ). CTA could also be incorporated as a stabilized inclusion to sensitize DNAN further. These results demonstrate how the judicious choice of dopant can lead to specific property improvements, providing a method for creating energetic materials with new properties to access metal-free primary explosives and physical hot spot models for explosive ignition. Molecular doping can operate in the absence of well-defined interactions, particularly when utilizing kinetically driven melt crystallizations, allowing property tuning when cocrystallization and synthon prediction fails. An integral part of the discussion in this chapter focuses on analytically determining if additive incorporation occurred as molecular doping vs. inclusions. Transmission infrared (IR) spectroscopy was utilized to verify doping by monitoring the often-overlooked overtone region of the spectrum. Molecular doping was determined by analyzing peak position shifts in the azide stretching interactions of CTA in the host matrix compared to pure, bulk CTA; this heavily relied on the argument that position accuracy could be known beyond the resolution setting of 4 cm^{-1}. However, positional error in IR spectroscopy is historically overestimated, and the effect of resolution and instrument-to-instrument variation on wavenumber accuracy is not well understood.

In *Chapter 3*, a recommendation of wavenumber accuracy as a function of spectral resolution, accounting for instrument variation among leading manufacturers, is given based on

an experimental study of polystyrene and acetaminophen.[81] For peaks that are well resolved and not saturated, the position can be known within 1.1 cm^{-1} at a spectral resolution of 4 cm^{-1} or higher, and within 2.2 cm^{-1} at 8 cm^{-1} resolution. However, this represents error at the extreme; the peak position can be known within 0.5 cm^{-1} at 4 cm^{-1} spectral resolution and within 0.9 cm^{-1} at 8 cm^{-1} spectral resolution based on the absolute average error (average $|\Delta|$). Other sources of variation are also discussed (e.g., poorly resolved peaks, peak saturation, water interference, spectral noise) to give general recommendations on when IR peak positions can be considered significantly different. Such guidelines are critical for interpreting subtle positional variations, as are often present in different crystal forms of pharmaceuticals.

In *Chapter 4*, a methodology for selecting additives to control the morphology of explosives is demonstrated based on targeting interactions present in cocrystals.[82] Specifically, 1,3,5,7-tetranitro-1,3,5,7-tetrazacyclooctane (HMX) was used as a model compound; three polymers were selected and successfully implemented as soluble, face-selective shape modifiers for HMX, a structurally similar analogue 3,3,7,7-tetrakis(difluoramino)octahydro-1,5-dinitro-1,5-diazocine (HNFX), and nitroguanidine (NQ). These results demonstrate morphology modification in both desirable (needle-to-block) and undesirable (block-to-needle) directions and illustrate a general design approach for crystal shape engineering applicable to energetic materials that lack traditional hydrogen bonding synthons. The ability to tune morphology, without triggering polymorphism, provides a critical tool for understanding how morphology and sensitivity are related for a given explosive form. Additionally, this design strategy for selecting polymeric additives has the potential to be employed outside energetics, especially in areas like pharmaceuticals with a rich library of cocrystals to gain inspiration for additives.

1.8 References

(1) Klapötke, T. M. *Chemistry of High-Energy Materials*; De Gruyter, 2017.

(2) Bennion, J. C.; Matzger, A. J. Development and Evolution of Energetic Cocrystals. *Acc. Chem. Res.* **2021**, *54* (7), 1699–1710. https://doi.org/10.1021/acs.accounts.0c00830.

(3) Krehl, P. O. K. *History of Shock Waves, Explosions and Impact: A Chronological and Biographical Reference*; Springer Science & Business Media, 2008.

(4) Wilbrand, J. Notiz Über Trinitrotoluol. *Justus Liebigs Ann. Chem.* **1863**, *128* (2), 178–179. https://doi.org/10.1002/jlac.18631280206.

(5) Häussermann, C. Über die explosiven Eigenschaften des Trinitrotoluols. *Angew. Chem.* **1891**, *4* (17), 508–511. https://doi.org/10.1002/ange.18910041703.

(6) Ravi, P.; Badgujar, D. M.; Gore, G. M.; Tewari, S. P.; Sikder, A. K. Review on Melt Cast Explosives. *Propellants Explos. Pyrotech.* **2011**, *36* (5), 393–403. https://doi.org/10.1002/prep.201100047.

(7) Meyer, R.; Köhler, J.; Homberg, Ing. A. *Explosives*, 1st ed.; John Wiley & Sons, Ltd, 2007. https://doi.org/10.1002/9783527617043.

(8) Licht, H.-H. Performance and Sensitivity of Explosives. *Propellants Explos. Pyrotech.* **2000**, *25* (3), 126–132. https://doi.org/10.1002/1521-4087(200006)25:3<126::AID-PREP126>3.0.CO;2-8.

(9) Zeman, S.; Jungová, M. Sensitivity and Performance of Energetic Materials. *Propellants Explos. Pyrotech.* **2016**, *41* (3), 426–451. https://doi.org/10.1002/prep.201500351.

(10) Politzer, P.; Murray, J. S. High Performance, Low Sensitivity: Conflicting or Compatible? *Propellants Explos. Pyrotech.* **2016**, *41* (3), 414–425. https://doi.org/10.1002/prep.201500349.

(11) Sabatini, J. J.; Oyler, K. D. Recent Advances in the Synthesis of High Explosive Materials. *Crystals* **2016**, *6* (1), 5. https://doi.org/10.3390/cryst6010005.

(12) Mehta, N.; Oyler, K.; Cheng, G.; Shah, A.; Marin, J.; Yee, K. Primary Explosives. *Z. Für Anorg. Allg. Chem.* **2014**, *640* (7), 1309–1313. https://doi.org/10.1002/zaac.201400053.

(13) Oyler, K. D. Green Primary Explosives. In *Green Energetic Materials*; John Wiley & Sons, Ltd, 2014; pp 103–132. https://doi.org/10.1002/9781118676448.ch05.

(14) Lease, N.; Klamborowski, L. M.; Perriot, R.; Cawkwell, M. J.; Manner, V. W. Identifying the Molecular Properties That Drive Explosive Sensitivity in a Series of Nitrate Esters. *J. Phys. Chem. Lett.* **2022**, *13* (40), 9422–9428. https://doi.org/10.1021/acs.jpclett.2c02701.

(15) Zhou, J.; Zhang, J.; Wang, B.; Qiu, L.; Xu, R.; Sheremetev, A. B. Recent Synthetic Efforts towards High Energy Density Materials: How to Design High-Performance Energetic Structures? *FirePhysChem* **2022**, *2* (2), 83–139. https://doi.org/10.1016/j.fpc.2021.09.005.

(16) Duarte, J. C.; Rocha, R. D. da; Borges, I. Which Molecular Properties Determine the Impact Sensitivity of an Explosive? A Machine Learning Quantitative Investigation of Nitroaromatic Explosives. *Phys. Chem. Chem. Phys.* **2023**, *25* (9), 6877–6890. https://doi.org/10.1039/D2CP05339J.

(17) Field, J. E. Hot Spot Ignition Mechanisms for Explosives. *Acc. Chem. Res.* **1992**, *25* (11), 489–496. https://doi.org/10.1021/ar00023a002.

(18) Bowden, F. P.; Yoffe, A. D. *Initiation and Growth of Explosion in Liquids and Solids*; CUP Archive, 1985.

(19) Marrs, F. W.; Davis, J. V.; Burch, A. C.; Brown, G. W.; Lease, N.; Huestis, P. L.; Cawkwell, M. J.; Manner, V. W. Chemical Descriptors for a Large-Scale Study on Drop-Weight Impact Sensitivity of High Explosives. *J. Chem. Inf. Model.* **2023**, *63* (3), 753–769. https://doi.org/10.1021/acs.jcim.2c01154.
(20) Storm, C. B.; Stine, J. R.; Kramer, J. F. Sensitivity Relationships in Energetic Materials. In *Chemistry and Physics of Energetic Materials*; Bulusu, S. N., Ed.; NATO ASI Series; Springer Netherlands: Dordrecht, 1990; pp 605–639. https://doi.org/10.1007/978-94-009-2035-4_27.
(21) Mathieu, D. Sensitivity of Energetic Materials: Theoretical Relationships to Detonation Performance and Molecular Structure. *Ind. Eng. Chem. Res.* **2017**, *56* (29), 8191–8201. https://doi.org/10.1021/acs.iecr.7b02021.
(22) Politzer, P.; Murray, J. S. Chapter 8 - Some Molecular and Crystalline Factors That Affect the Sensitivities of Explosives. In *Theoretical and Computational Chemistry*; Mathieu, D., Ed.; Molecular Modeling of the Sensitivities of Energetic Materials; Elsevier, 2022; Vol. 22, pp 173–194. https://doi.org/10.1016/B978-0-12-822971-2.00009-7.
(23) Stine, J. R. Molecular Structure and Performance of High Explosives. *MRS Online Proc. Libr.* **1992**, *296* (1), 3–12. https://doi.org/10.1557/PROC-296-3.
(24) Davey, R. J.; Garside, J. *From Molecules to Crystallizers*; Oxford Chemistry Primers; Oxford University Press: Oxford, New York, 2001.
(25) Myerson, A. S.; Ginde, R. 2 - Crystals, Crystal Growth, and Nucleation. In *Handbook of Industrial Crystallization (Second Edition)*; Myerson, A. S., Ed.; Butterworth-Heinemann: Woburn, 2002; pp 33–65. https://doi.org/10.1016/B978-075067012-8/50004-5.
(26) Schittny, A.; Huwyler, J.; Puchkov, M. Mechanisms of Increased Bioavailability through Amorphous Solid Dispersions: A Review. *Drug Deliv.* **2019**, *27* (1), 110–127. https://doi.org/10.1080/10717544.2019.1704940.
(27) Desiraju, G. R. Crystal Engineering: From Molecule to Crystal. *J. Am. Chem. Soc.* **2013**, *135* (27), 9952–9967. https://doi.org/10.1021/ja403264c.
(28) Purohit, R.; Venugopalan, P. Polymorphism: An Overview. *Resonance* **2009**, *14* (9), 882–893. https://doi.org/10.1007/s12045-009-0084-7.
(29) Brog, J.-P.; Chanez, C.-L.; Crochet, A.; M. Fromm, K. Polymorphism, What It Is and How to Identify It: A Systematic Review. *RSC Adv.* **2013**, *3* (38), 16905–16931. https://doi.org/10.1039/C3RA41559G.
(30) Liu, G.; Gou, R.; Li, H.; Zhang, C. Polymorphism of Energetic Materials: A Comprehensive Study of Molecular Conformers, Crystal Packing, and the Dominance of Their Energetics in Governing the Most Stable Polymorph. *Cryst. Growth Des.* **2018**, *18* (7), 4174–4186. https://doi.org/10.1021/acs.cgd.8b00704.
(31) Kohno, Y.; Maekawa, K.; Tsuchioka, T.; Hashizume, T.; Imamura, A. A Relationship between the Impact Sensitivity and the Electronic Structures for the Unique N□N Bond in the HMX Polymorphs. *Combust. Flame* **1994**, *96* (4), 343–350. https://doi.org/10.1016/0010-2180(94)90103-1.
(32) J. Cruz-Cabeza, A.; J. Davey, R.; H. Oswald, I. D.; R. Ward, M.; J. Sugden, I. Polymorphism in p -Aminobenzoic Acid. *CrystEngComm* **2019**, *21* (13), 2034–2042. https://doi.org/10.1039/C8CE01890A.

(33) Saha, B. K.; Nath, N. K.; Thakuria, R. Polymorphs with Remarkably Distinct Physical and/or Chemical Properties. *Chem. Rec.* **2023**, *23* (1), e202200173. https://doi.org/10.1002/tcr.202200173.
(34) Dandekar, P.; Kuvadia, Z. B.; Doherty, M. F. Engineering Crystal Morphology. *Annu. Rev. Mater. Res.* **2013**, *43* (1), 359–386. https://doi.org/10.1146/annurev-matsci-071312-121623.
(35) Gao, Y.; Song, W.; Yang, J.; Ji, X.; Wang, N.; Huang, X.; Wang, T.; Hao, H. Crystal Morphology Prediction Models and Regulating Methods. *Crystals* **2024**, *14* (6), 484. https://doi.org/10.3390/cryst14060484.
(36) Desiraju, G. R. Supramolecular Synthons in Crystal Engineering—A New Organic Synthesis. *Angew. Chem. Int. Ed. Engl.* **1995**, *34* (21), 2311–2327. https://doi.org/10.1002/anie.199523111.
(37) *Molecular Recognition at Crystal Interfaces*. https://doi.org/10.1126/science.253.5020.637.
(38) Schultheiss, N.; Newman, A. Pharmaceutical Cocrystals and Their Physicochemical Properties. *Cryst. Growth Des.* **2009**, *9* (6), 2950–2967. https://doi.org/10.1021/cg900129f.
(39) Duggirala, N. K.; Perry, M. L.; Almarsson, Ö.; Zaworotko, M. J. Pharmaceutical Cocrystals: Along the Path to Improved Medicines. *Chem. Commun.* **2015**, *52* (4), 640–655. https://doi.org/10.1039/C5CC08216A.
(40) Yousef, M. A. E.; Vangala, V. R. Pharmaceutical Cocrystals: Molecules, Crystals, Formulations, Medicines. *Cryst. Growth Des.* **2019**, *19* (12), 7420–7438. https://doi.org/10.1021/acs.cgd.8b01898.
(41) Kavanagh, O. N.; Croker, D. M.; Walker, G. M.; Zaworotko, M. J. Pharmaceutical Cocrystals: From Serendipity to Design to Application. *Drug Discov. Today* **2019**, *24* (3), 796–804. https://doi.org/10.1016/j.drudis.2018.11.023.
(42) Yadav, A. V.; Shete, A. S.; Dabke, A. P.; Kulkarni, P. V.; Sakhare, S. S. Co-Crystals: A Novel Approach to Modify Physicochemical Properties of Active Pharmaceutical Ingredients. *Indian J. Pharm. Sci.* **2009**, *71* (4), 359–370. https://doi.org/10.4103/0250-474X.57283.
(43) Berry, D. J.; Steed, J. W. Pharmaceutical Cocrystals, Salts and Multicomponent Systems; Intermolecular Interactions and Property Based Design. *Adv. Drug Deliv. Rev.* **2017**, *117*, 3–24. https://doi.org/10.1016/j.addr.2017.03.003.
(44) Guo, M.; Sun, X.; Chen, J.; Cai, T. Pharmaceutical Cocrystals: A Review of Preparations, Physicochemical Properties and Applications. *Acta Pharm. Sin. B* **2021**, *11* (8), 2537–2564. https://doi.org/10.1016/j.apsb.2021.03.030.
(45) Foroughi, L. M.; Wiscons, R. A.; Bois, D. R. D.; Matzger, A. J. Improving Stability of the Metal-Free Primary Energetic Cyanuric Triazide (CTA) through Cocrystallization. *Chem. Commun.* **2020**, *56* (14), 2111–2114. https://doi.org/10.1039/C9CC09465B.
(46) Bellas, M. K.; Matzger, A. J. Achieving Balanced Energetics through Cocrystallization. *Angew. Chem. Int. Ed.* **2019**, *58* (48), 17185–17188. https://doi.org/10.1002/anie.201908709.
(47) Landenberger, K. B.; Matzger, A. J. Cocrystal Engineering of a Prototype Energetic Material: Supramolecular Chemistry of 2,4,6-Trinitrotoluene. *Cryst. Growth Des.* **2010**, *10* (12), 5341–5347. https://doi.org/10.1021/cg101300n.

(48) Aakeröy, C. B.; Wijethunga, T. K.; Desper, J. Crystal Engineering of Energetic Materials: Co-Crystals of Ethylenedinitramine (EDNA) with Modified Performance and Improved Chemical Stability. *Chem. – Eur. J.* **2015**, *21* (31), 11029–11037. https://doi.org/10.1002/chem.201501721.
(49) Gamekkanda, J. C.; Sinha, A. S.; Aakeröy, C. B. Cocrystals and Salts of Tetrazole-Based Energetic Materials. *Cryst. Growth Des.* **2020**, *20* (4), 2432–2439. https://doi.org/10.1021/acs.cgd.9b01620.
(50) Landenberger, K. B.; Bolton, O.; Matzger, A. J. Energetic–Energetic Cocrystals of Diacetone Diperoxide (DADP): Dramatic and Divergent Sensitivity Modifications via Cocrystallization. *J. Am. Chem. Soc.* **2015**, *137* (15), 5074–5079. https://doi.org/10.1021/jacs.5b00661.
(51) Liu, Y.; Li, S.; Xu, J.; Zhang, H.; Guan, Y.; Jiang, H.; Huang, S.; Huang, H.; Wang, Z. Three Energetic 2,2′,4,4′,6,6′-Hexanitrostilbene Cocrystals Regularly Constructed by H-Bonding, π-Stacking, and van Der Waals Interactions. *Cryst. Growth Des.* **2018**, *18* (4), 1940–1943. https://doi.org/10.1021/acs.cgd.8b00019.
(52) Bolton, O.; Simke, L. R.; Pagoria, P. F.; Matzger, A. J. High Power Explosive with Good Sensitivity: A 2:1 Cocrystal of CL-20:HMX. *Cryst. Growth Des.* **2012**, *12* (9), 4311–4314. https://doi.org/10.1021/cg3010882.
(53) Bolton, O.; Matzger, A. J. Improved Stability and Smart-Material Functionality Realized in an Energetic Cocrystal. *Angew. Chem.* **2011**, *123* (38), 9122–9125. https://doi.org/10.1002/ange.201104164.
(54) Bennion, J. C.; Siddiqi, Z. R.; Matzger, A. J. A Melt Castable Energetic Cocrystal. *Chem. Commun.* **2017**, *53* (45), 6065–6068. https://doi.org/10.1039/C7CC02636F.
(55) Bennion, J. C.; McBain, A.; Son, S. F.; Matzger, A. J. Design and Synthesis of a Series of Nitrogen-Rich Energetic Cocrystals of 5,5′-Dinitro-2H,2H′-3,3′-Bi-1,2,4-Triazole (DNBT). *Cryst. Growth Des.* **2015**, *15* (5), 2545–2549. https://doi.org/10.1021/acs.cgd.5b00336.
(56) Bellas, M. K.; Matzger, A. J. Peroxosolvate Discovery Method Leads to First Cocrystal with Three Energetic Components. *Chem. Commun.* **2022**, *58* (63), 8806–8809. https://doi.org/10.1039/D2CC02024F.
(57) Landenberger, K. B.; Matzger, A. J. Cocrystals of 1,3,5,7-Tetranitro-1,3,5,7-Tetrazacyclooctane (HMX). *Cryst. Growth Des.* **2012**, *12* (7), 3603–3609. https://doi.org/10.1021/cg3004245.
(58) Kent, R. V.; Wiscons, R. A.; Sharon, P.; Grinstein, D.; Frimer, A. A.; Matzger, A. J. Cocrystal Engineering of a High Nitrogen Energetic Material. *Cryst. Growth Des.* **2018**, *18* (1), 219–224. https://doi.org/10.1021/acs.cgd.7b01126.
(59) Chapman, C. J.; Groven, L. J. Evaluation of Solvate and Co-Crystal Screening Methods for CL-20 Containing Energetic Materials. *J. Energ. Mater.* **2022**, *40* (3), 258–272. https://doi.org/10.1080/07370652.2020.1867936.
(60) Ungnade, H. E.; Roberts, E. M.; Kissinger, L. W. Hydrogen Bonding in Nitro Compounds1. *J. Phys. Chem.* **1964**, *68* (11), 3225–3228. https://doi.org/10.1021/j100793a024.
(61) Song, R.-Q.; Cölfen, H. Additive Controlled Crystallization. *CrystEngComm* **2011**, *13* (5), 1249–1276. https://doi.org/10.1039/C0CE00419G.

(62) Zhu, Y.; Lu, M.; Gao, F.; Zhou, C.; Jia, C.; Wang, J. Role of Tailor-Made Additives in Crystallization from Solution: A Review. *Ind. Eng. Chem. Res.* **2023**, *62* (12), 4800–4816. https://doi.org/10.1021/acs.iecr.2c04025.
(63) Urwin, S. J.; Levilain, G.; Marziano, I.; Merritt, J. M.; Houson, I.; Ter Horst, J. H. A Structured Approach To Cope with Impurities during Industrial Crystallization Development. *Org. Process Res. Dev.* **2020**, *24* (8), 1443–1456. https://doi.org/10.1021/acs.oprd.0c00166.
(64) Capellades, G.; O. Bonsu, J.; S. Myerson, A. Impurity Incorporation in Solution Crystallization: Diagnosis, Prevention, and Control. *CrystEngComm* **2022**, *24* (11), 1989–2001. https://doi.org/10.1039/D1CE01721G.
(65) Jacobs, I. E.; Moulé, A. J. Controlling Molecular Doping in Organic Semiconductors. *Adv. Mater. Deerfield Beach Fla* **2017**, *29* (42). https://doi.org/10.1002/adma.201703063.
(66) Arduca, E.; Perego, M. Doping of Silicon Nanocrystals. *Mater. Sci. Semicond. Process.* **2017**, *62*, 156–170. https://doi.org/10.1016/j.mssp.2016.10.054.
(67) Grzesiak, A. L.; Uribe, F. J.; Ockwig, N. W.; Yaghi, O. M.; Matzger, A. J. Polymer-Induced Heteronucleation for the Discovery of New Extended Solids. *Angew. Chem. Int. Ed.* **2006**, *45* (16), 2553–2556. https://doi.org/10.1002/anie.200504312.
(68) Lang, M.; Grzesiak, A. L.; Matzger, A. J. The Use of Polymer Heteronuclei for Crystalline Polymorph Selection. *J. Am. Chem. Soc.* **2002**, *124* (50), 14834–14835. https://doi.org/10.1021/ja0286526.
(69) Pfund, L. Y.; Price, C. P.; Frick, J. J.; Matzger, A. J. Controlling Pharmaceutical Crystallization with Designed Polymeric Heteronuclei. *J. Am. Chem. Soc.* **2015**, *137* (2), 871–875. https://doi.org/10.1021/ja511106j.
(70) López-Mejías, V.; Kampf, J. W.; Matzger, A. J. Polymer-Induced Heteronucleation of Tolfenamic Acid: Structural Investigation of a Pentamorph. *J. Am. Chem. Soc.* **2009**, *131* (13), 4554–4555. https://doi.org/10.1021/ja806289a.
(71) Staab, E.; Addadi, L.; Leiserowitz, L.; Lahav, M. Control of Polymorphism by 'Tailor-Made' Polymeric Crystallization Auxiliaries. Preferential Precipitation of a Metastable Polar Form for Second Harmonic Generation. *Adv. Mater.* **1990**, *2* (1), 40–43. https://doi.org/10.1002/adma.19900020108.
(72) Bellucci, M. A.; Marx, A.; Wang, B.; Fang, L.; Zhou, Y.; Greenwell, C.; Li, Z.; Becker, A.; Sun, G.; Brandenburg, J. G.; Sekharan, S. Effect of Polymer Additives on the Crystal Habit of Metformin HCl. *Small Methods* **2023**, *7* (6), 2201692. https://doi.org/10.1002/smtd.202201692.
(73) Yu, S.; Wang, Z.; Ma, Y.; Xue, F. Effect of Natural Polymer Additives on Crystal Form and Morphology of Clozapine Anhydrate and Monohydrate. *J. Mol. Liq.* **2022**, *364*, 119985. https://doi.org/10.1016/j.molliq.2022.119985.
(74) Chen, H.; Li, L.; Jin, S.; Chen, S.; Jiao, Q. Effects of Additives on ε-HNIW Crystal Morphology and Impact Sensitivity. *Propellants Explos. Pyrotech.* **2012**, *37* (1), 77–82. https://doi.org/10.1002/prep.201000014.
(75) Luo, Z.; Cui, Y.; Dong, W.; Xu, Q.; Zou, G.; Kang, C.; Hou, B.; Chen, S.; Gong, J. Morphological Diversity of Nitroguanidine Crystals with Enhanced Mechanical Performance and Thermodynamic Stability. *J. Cryst. Growth* **2017**, *480*, 132–140. https://doi.org/10.1016/j.jcrysgro.2017.10.012.
(76) Li, Z.; Shi, P.; Yang, Y.; Sun, P.; Wang, Y.; Xu, S.; Gong, J. Tuning Crystallization and Stability of the Metastable Polymorph of DL-Methionine by a Structurally Similar

Additive. *CrystEngComm* **2019**, *21* (24), 3731–3739. https://doi.org/10.1039/C9CE00009G.
(77) Lechuga-Ballesteros, D.; Rodriguez-Hornedo, N. Growth and Morphology of L-Alanine Crystals: Influence of Additive Adsorption. *Pharm. Res.* **1993**, *10* (7), 1008–1014. https://doi.org/10.1023/A:1018962722691.
(78) Yani, Y.; Chow, P. S.; Tan, R. B. H. Molecular Simulation Study of the Effect of Various Additives on Salbutamol Sulfate Crystal Habit. *Mol. Pharm.* **2011**, *8* (5), 1910–1918. https://doi.org/10.1021/mp200277u.
(79) Hatcher, L. E.; Li, W.; Payne, P.; Benyahia, B.; Rielly, C. D.; Wilson, C. C. Tuning Morphology in Active Pharmaceutical Ingredients: Controlling the Crystal Habit of Lovastatin through Solvent Choice and Non-Size-Matched Polymer Additives. *Cryst. Growth Des.* **2020**, *20* (9), 5854–5862. https://doi.org/10.1021/acs.cgd.0c00470.
(80) Nicolau, S. T.; Matzger, A. J. Sensitizing Explosives Through Molecular Doping. *ChemPlusChem* **2024**, *89* (6), e202300724. https://doi.org/10.1002/cplu.202300724.
(81) Nicolau, S. T.; Matzger, A. J. An Evaluation of Resolution, Accuracy, and Precision in FT-IR Spectroscopy. *Spectrochim. Acta. A. Mol. Biomol. Spectrosc.* **2024**, *319*, 124545. https://doi.org/10.1016/j.saa.2024.124545.
(82) Nicolau, S. T.; Matzger, A. J. Controlling Energetic Crystal Morphology Using Tailored Polymeric Additives. *Cryst. Growth Des.* **2025**, *25* (5), 1667–1674. https://doi.org/10.1021/acs.cgd.5c00049.

Chapter 2 Sensitizing Explosives Through Molecular Doping

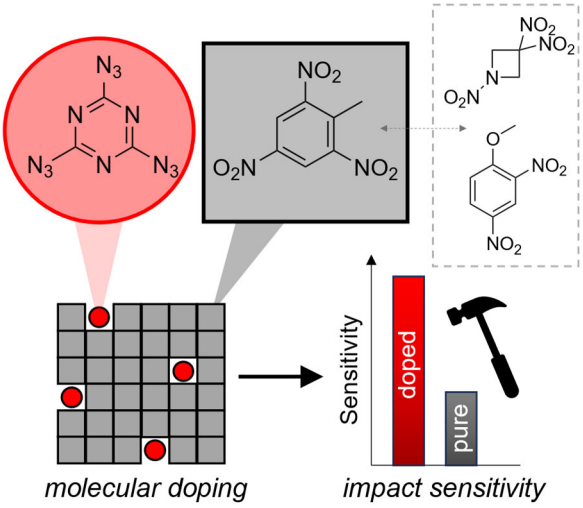


Figure 2.1 Increased sensitivity to impact was imparted to three melt-castable explosives by molecular doping with cyanuric triazide.

2.1 Publication of Chapter

Nicolau, S. T.; Matzger, A. J. Sensitizing Explosives Through Molecular Doping. *ChemPlusChem* **2024**, *89* (6), e202300724. https://doi.org/10.1002/cplu.202300724.

2.2 Introduction

Cocrystals are multicomponent molecular crystals that are generally assembled in defined ratios and are held together by intermolecular interactions.[1] Cocrystals have seen extensive use in pharmaceutical solid form engineering, improving physiochemical properties including stability, solubility, and bioavailability.[2–5] The success of this technique in the context of pharmaceuticals is owed to the substantial development in understanding of supramolecular synthons governing cocrystal formation. Common motifs exploit carboxylic acids, amides, and alcohols to influence hydrogen bonding, with associated π-π stacking and/or Van der Waals interactions.[6–10] More

recently, cocrystallization has been extended to the field of energetic materials (explosives, propellants, and pyrotechnics) to modulate impact sensitivity, thermal stability, chemical stability, and hygroscopicity.[11–14] However, most of these compounds lack traditionally successful synthons that arise from hydrogen bonding interactions because energetics are dominated primarily by nitro groups that have a weak propensity for hydrogen bonding.[15] Notwithstanding the fact that some energetics do exist with more reliable synthons[16,17], and that energetic cocrystal synthons are becoming better understood (e.g., nitro-π interactions and nontraditional nitro-hydrogen bonding[18,19]), predicting molecules that are likely to cocrystallize with each other still remains a challenge and follows a trial-and-error approach.[20,21] Here, an alternative strategy to alter energetic properties is explored suited to cases where cocrystal formation does not readily occur.

Molecular doping, where a dopant is inserted into a host crystal at low concentration without impacting the packing in the crystal lattice (Figure 2.2a), is a potentially general method for property modification. This type of multicomponent crystal design is advantageous when compared to cocrystallization because doping proceeds in the absence of specific interactions; impurity incorporation is a common phenomenon that is influenced by solubility, crystal growth rates, and chemical similarity.[22–24] Because components can be combined in a molecular crystal to alter solid-state properties via cocrystallization, it was hypothesized that a dopant with a targeted property could do the same to its host compound. To test this notion, the very impact sensitive energetic cyanuric triazide (CTA) was selected as the dopant to test if less sensitive energetics could gain the sensitivity of a more sensitive energetic by molecular doping.

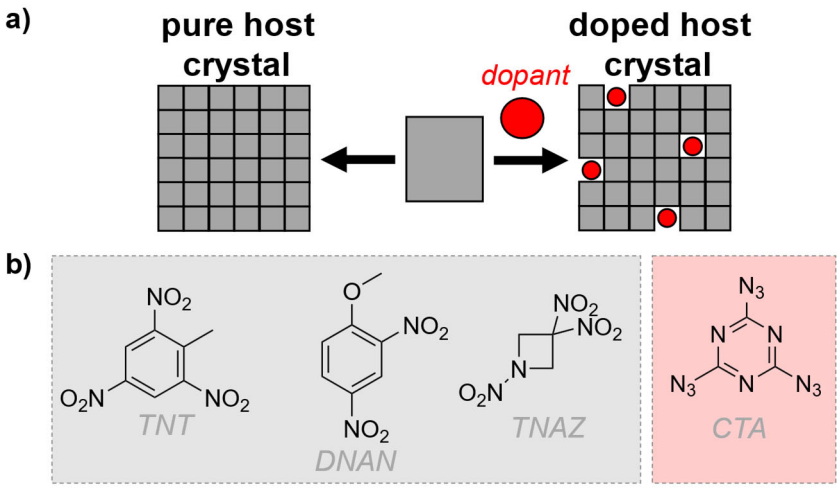


Figure 2.2 a) During crystallization, a dopant can be inserted into a host crystal in low concentrations without impacting the packing of the crystal lattice (molecular doping). b) CTA (red box) was evaluated for the ability to sensitize a series of melt-castable host energetics (grey box).

To determine if the dopant is incorporated into the host crystal lattice, two approaches were utilized: transmission infrared (IR) microspectroscopy and powder X-ray diffraction (PXRD). CTA possesses strong and unique vibrational stretches in the overtone region of the host, associated with its azide functionality that we exploit to validate incorporation.[25] This information supplements the PXRD, which allows for identification of unincorporated material, which in turn informs solubility of the dopant in the host. CTA was also classified as a dopant vs. inclusion by Raman mapping and tracking CTA signal variation across the sample. Herein, three melt-castable energetics are sensitized to impact stimulus by CTA incorporation (Figure 2.2b).

2.3 Results and Discussion

Three energetic systems were examined to study the effect of CTA doping on host impact sensitivity. Specifically, 2,4,6-trinitrotoluene (TNT) was chosen as a host due to its wide use in military and industrial applications.[18] 2,4-dinitroanisole (DNAN) and 1,3,3-trinitroazetidine (TNAZ) have been considered "greener" (less toxic), melt-castable replacements for TNT.[26] All

host materials were melted in the presence of CTA, just above the melting point of the host, and allowed to crystallize at room temperature.

PXRD was used to determine the mode of dopant incorporation into the host lattice, as well as monitor crystal form retention of the doped host. When molecularly doped, dopants are inserted into the crystal lattice with somewhat regular distribution, retaining the bulk identity of the host. However, dopants can incorporate into pockets or large defects in the crystal, segmented from the host lattice and are referred to as inclusions; these present as physical mixtures of both components in characterization.[27,28] Melt-cast TNT crystallized in the orthorhombic form[29] (Figure A.1) and was retained throughout all loadings of CTA tested in this study. In Figure 2.3a, TNT loaded with 1.0% CTA (moles of CTA relative to moles of host) shows diffraction peaks only from TNT, indicating that all of the CTA is doped into TNT and no crystalline CTA is present; this is indicative of molecular doping. In contrast, samples with 1.5%-12.1% CTA show diffraction peaks from both crystalline CTA and TNT, indicating CTA is not exclusively doped into the lattice but also presents as inclusions. Given the fast crystallization process observed in the melt-cast energetics, CTA incorporation into the lattice of the host is likely dominated by kinetics.[30] However, there is an enthalpic cost for incorporation into the crystal lattice, limiting the level of CTA that can be molecularly doped without lattice disruption. A maximum molecular doping level is confirmed by comparing the area of CTA peaks to the area of a TNT reference peak ($2\theta=12.5°$) as a function of CTA loading, where the x-intercept yields the percent CTA that corresponds to no detectable diffraction signal (Figure 2.3b). Based on the signal to noise achieved for the CTA peaks, the limit of detection for CTA is $\approx 0.1\%$. A two-dimensional PXRD collection technique with Gandolfi moves was used to minimize preferred orientation in the powder patterns (Figure A.2). Analysis of two different

CTA peaks (2θ=11.5° “CTA 1” and 27.7° “CTA 2”) and extrapolating the x-intercept further supports the 1.0 vs 1.5% CTA-doped TNT trend presented in the powder patterns, as maximum molecular dopant loadings were both extrapolated as 1% CTA.

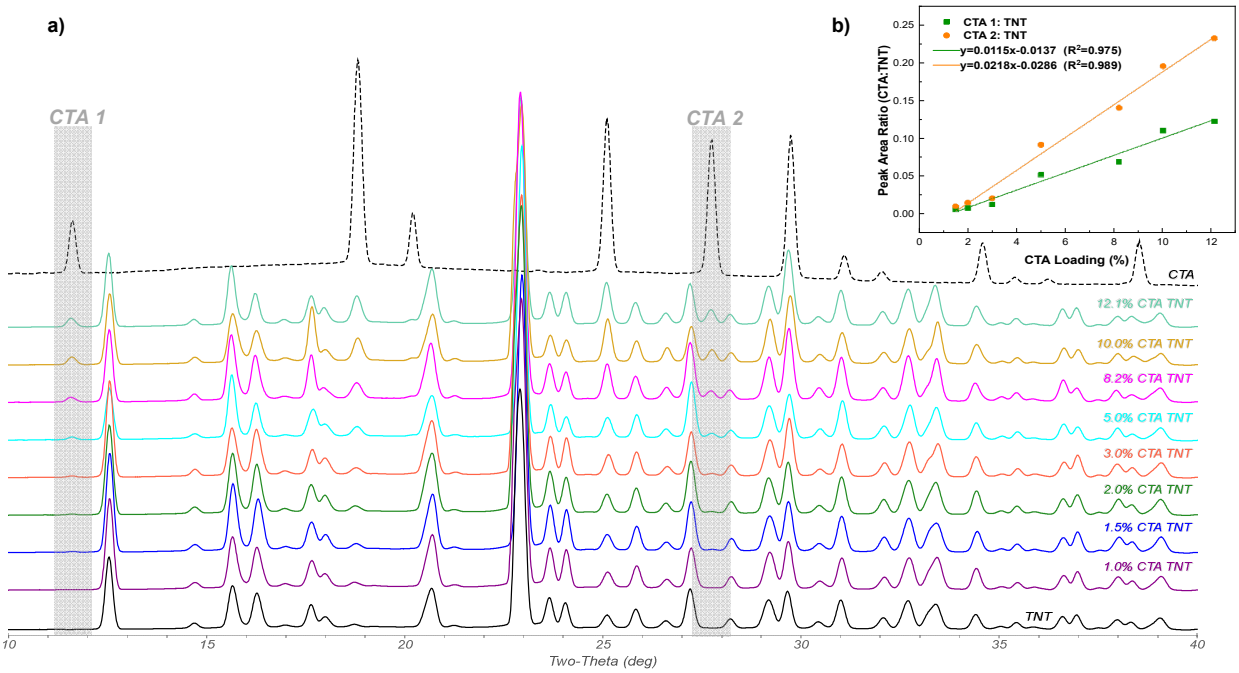


Figure 2.3 a) PXRD patterns of pure TNT, pure CTA, and various loadings of CTA into TNT (grey boxes emphasize unique diffraction peaks of CTA). b) A maximum molecular dopant loading is extrapolated based on peak area ratios of the two CTA peaks to a TNT reference peak.

The same PXRD analysis was performed with DNAN and TNAZ doped with CTA. Melt-cast DNAN crystallized in the β-monoclinic form[31] and was retained throughout all loadings of CTA (Figure A.1). The melt samples with 1.0% CTA and 2.0% CTA in DNAN show diffraction peaks only from DNAN, whereas samples with 2.5%-12.0% CTA show diffraction peaks from both crystalline CTA and DNAN (Figure 2.4). With this compound, three CTA peaks were available for peak area ratio analysis to extrapolate the maximum molecular dopant loading: 1-2% CTA in DNAN. As will be discussed later in this study (Raman mapping), DNAN posed challenging mixing and separation issues as the dopant concentration approached the maximum loading level. TNAZ was melt-cast and crystallized in its only stable form

(orthorhombic)[32], both with and without dopant (Figure A.1). PXRD showed that 1.0% CTA could be molecularly doped into the TNAZ lattice, indicated by a diffraction pattern with peaks only from TNAZ, whereas 1.5-10.0% showed additional crystalline CTA signal (Figure 2.5). A similar maximum dopant calculation using three CTA peaks supports 1% CTA as the limit for molecular doping.

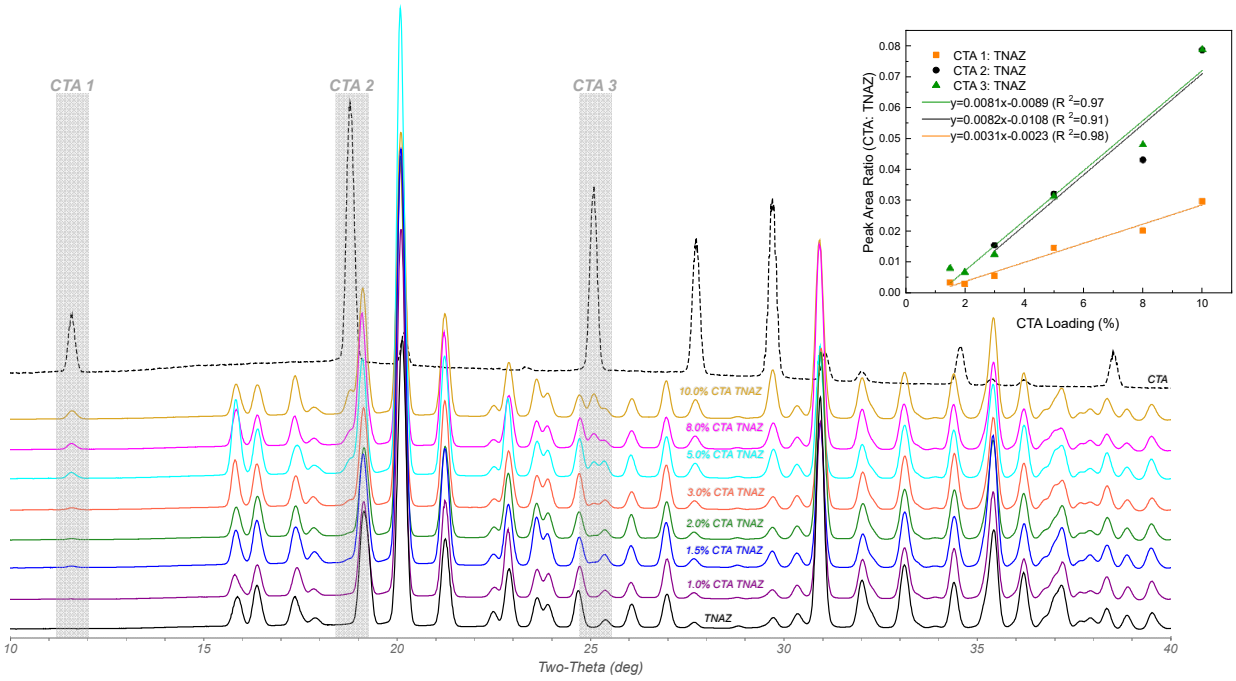


Figure 2.4 PXRD patterns of pure DNAN, pure CTA, and various loadings of CTA into DNAN (grey boxes emphasize unique diffraction peaks of CTA). The inset image represents maximum dopant loading extrapolation based on peak area ratios of three CTA peaks to a DNAN reference peak.

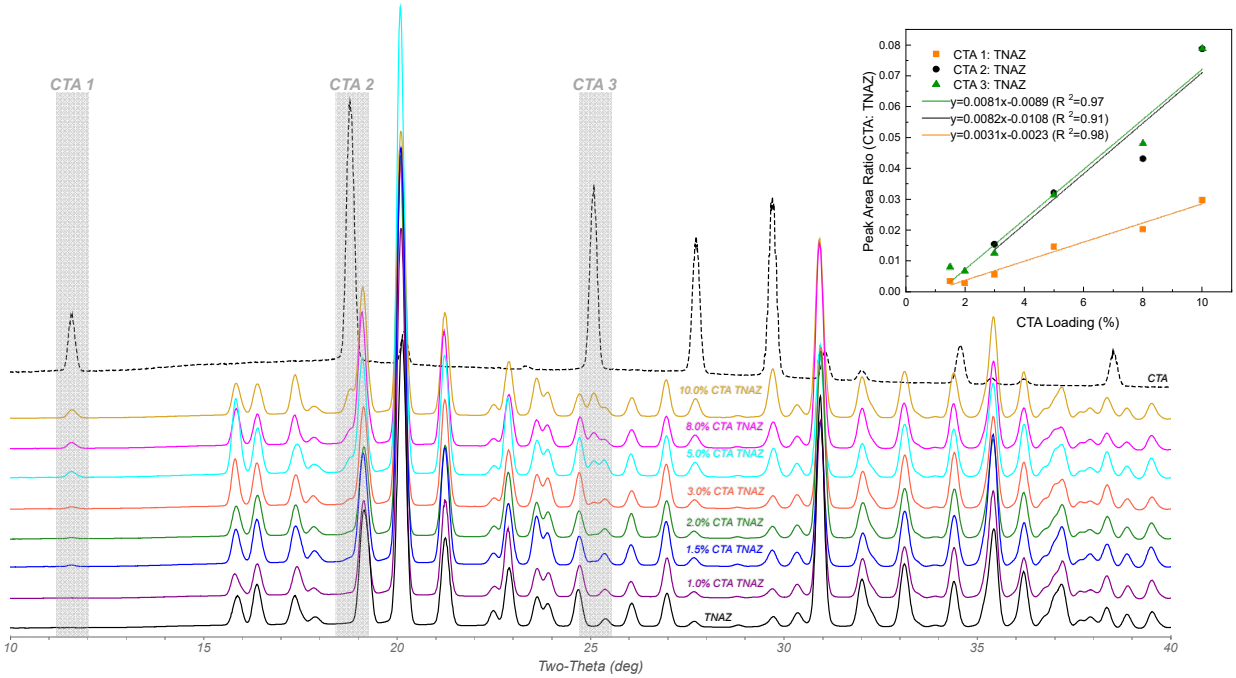


Figure 2.5 PXRD patterns of pure TNAZ, pure CTA, and various loadings of CTA into TNAZ (grey boxes emphasize unique diffraction peaks of CTA). The inset image represents maximum dopant loading extrapolation based on peak area ratios of three CTA peaks to a TNAZ reference peak.

Retention of CTA in the energetic was also verified using a transmission IR microscope. Transmission collection mode with a cooled detector allows for sensitive sampling for low-level dopant detection, often saturating mid-infrared regions. However, by focusing on overtone bands, analysis of the host is still possible (Figure 2.6). From an analytical perspective, CTA is a useful dopant because it possesses unique and strong azide (N_3) stretches in this weak, overtone region of the host energetics.[25] This allows for quick validation that CTA is retained in the samples by the presence of three azide peaks: the symmetric N_3 + C_{aryl}-N_{azide} stretch at 2192 cm^{-1}, asymmetric N_3 stretch at 2158 cm^{-1}, and the ring deformation + C_{aryl}-N_{azide} stretch at 2115 cm^{-1}.

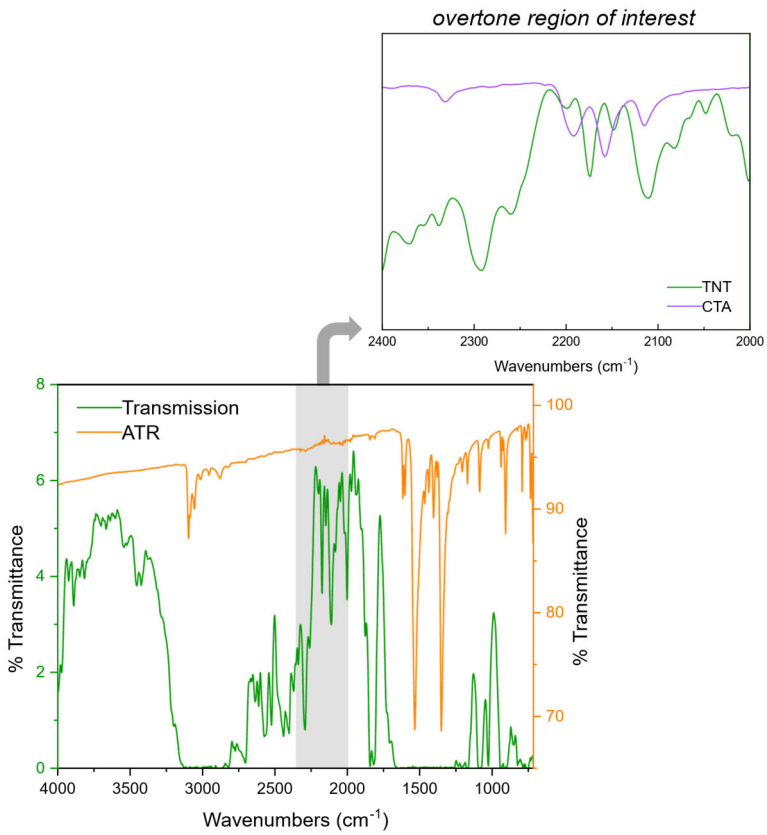


Figure 2.6 Transmission infrared spectroscopy collection mode of TNT (host compound) saturates mid-infrared regions when compared to an ATR collection. CTA is an excellent model dopant because it possesses strong and unique vibrational stretches in the overtone region of the host which are not saturated in transmission mode.

PXRD suggests that 1% CTA was molecularly doped into the crystal lattice of TNT based on the presence of only TNT diffraction peaks (Figure 2.3), and IR mapping confirms that CTA is retained in the crystallized melt (Figure 2.7). Data profiling was used to summarize the mapping output, specifically utilizing a peak area ratio of total azide CTA stretches (≈2200 – 2100 cm^{-1}) to a TNT overtone region (≈2000 cm^{-1}). The uniform color distribution of the profile, representing uniform peak area ratios of the CTA region of interest to TNT overtone, correlates with the sample area in the microscope image. Additional support for molecular doping as the mode of incorporation is found in the positions of the CTA azide bands. A representative 1% CTA in TNT spectrum reveals that the symmetric N_3 + C_{aryl}-N_{azide} stretch is shifted by 3 cm^{-1}, while the asymmetric N_3 stretch is shifted by 2 cm^{-1}, and the ring deformation + Caryl-Nazide

stretch by 1 cm^{-1} (Figure 2.7). The shifts in these bands arise from CTA interacting with the TNT matrix; the TNT overtone band at 2001 cm^{-1} remains in the same position in both the pure and doped spectra.

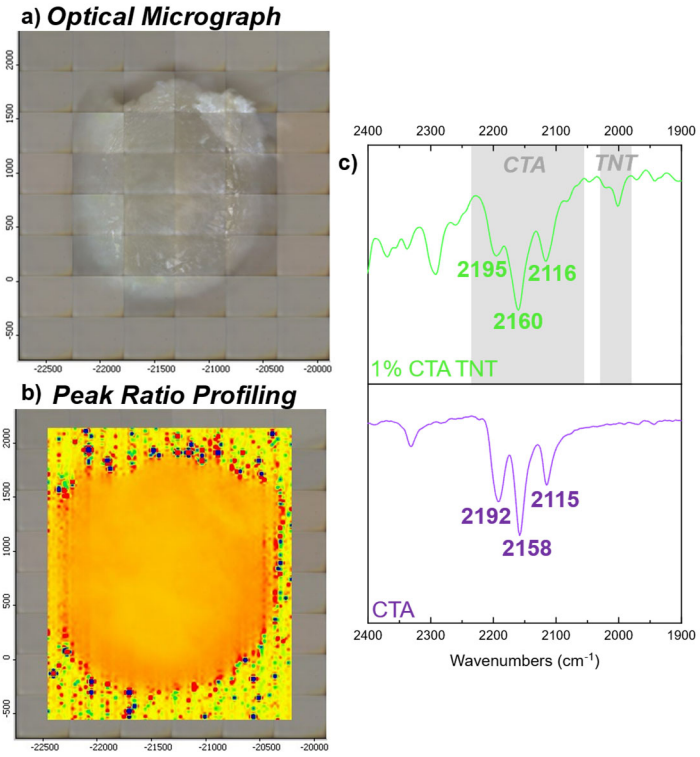


Figure 2.7 a) TNT melt cast with 1% CTA mapped using transmission IR microspectroscopy to verify CTA incorporation into host. b) Peak ratio profiling is used to check for CTA present throughout the entire sample. The uniform color distribution of the profile represents a uniform peak area ratio of the CTA region of interest to a TNT overtone (highlighted in grey boxes). c) A 1% spectrum reveals shifts in CTA primary bands that support molecular doping.

For all three energetic host compounds, the asymmetric N_3 stretch at 2158 cm^{-1} is the strongest and most well-defined azide stretch. It exhibits no overlap with overtone bands, making it a useful starting point for identifying CTA retention in crystallized melts. For DNAN and TNAZ, this band is found to shift 1 cm^{-1} relative to pure CTA, while the symmetric N_3 + C_{aryl}-N_{azide} stretch shifts 1-6 cm^{-1}, and the ring deformation + C_{aryl}-N_{azide} stretch by 1 cm^{-1} (Figures 2.8 and 2.9). Distinct regions of pure, unshifted CTA signal segmented within the host were not

found in the IR maps due to the modest spatial resolution of the IR microscope (25 µm). Thus, a complimentary vibrational technique, Raman microspectroscopy, with a smaller sampling window (5 µm step size) was used to assess CTA incorporation.

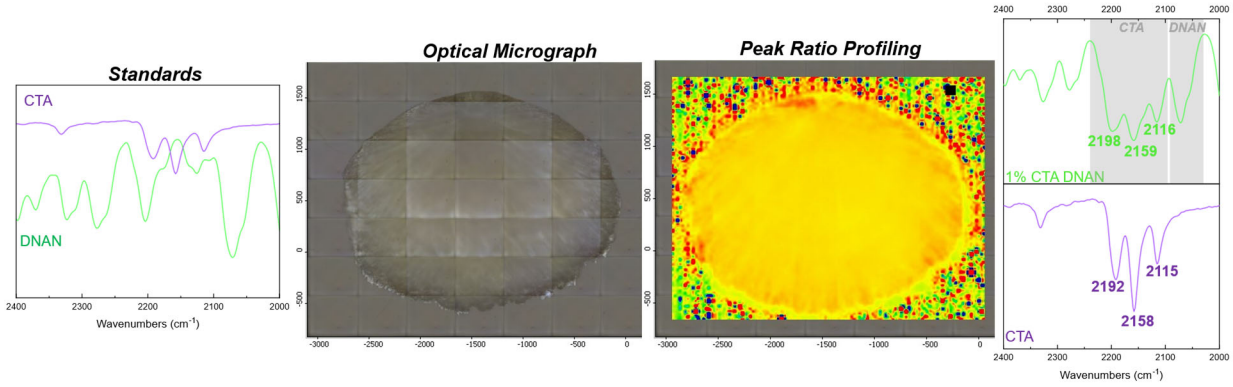


Figure 2.8 DNAN melt cast with 2% CTA is mapped using transmission IR microspectroscopy to verify CTA incorporation into host. Peak ratio profiling is used to check for CTA present throughout the entire sample. The uniform color distribution of the profile represents uniform peak area ratios of the CTA region of interest to DNAN overtone (highlighted in grey boxes). A representative 2% spectrum is analyzed for shifts in CTA primary bands to further support molecular doping.

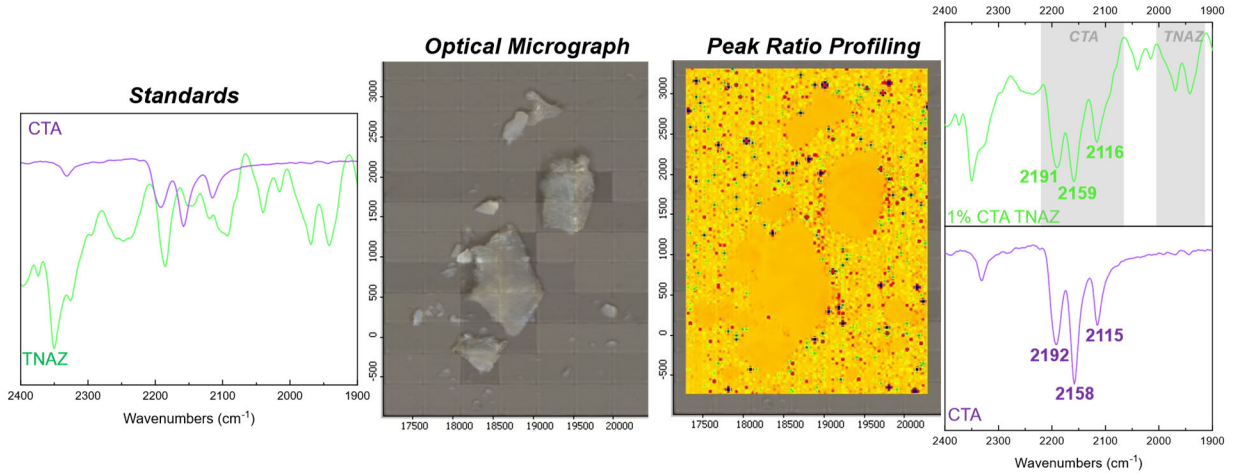


Figure 2.9 TNAZ melt cast with 1% CTA is mapped using transmission IR microspectroscopy to verify CTA incorporation into host. Peak ratio profiling is used to check for CTA present throughout the entire sample. The uniform color distribution of the profile represents uniform peak area ratios of the CTA region of interest to TNAZ overtones (highlighted in grey boxes). A representative 1% spectrum is analyzed for shifts in CTA primary bands to further support molecular doping.

Raman microspectroscopy was useful for not only identifying CTA in the energetic melts but also monitoring dopant distribution as a function of dopant loading. In TNT with 1% doped-

CTA or 10% inclusion-CTA, CTA signal was identified throughout the mapped area, identifying a band from the C_{aryl}-N_{azide} stretch of CTA at 982 cm^{-1} (Figure 2.10; full Raman maps in Figure A.3). However, significant segmentation of CTA was identified in the 10% sample compared to 1% based on clustering of high CTA band intensity. In red regions, there is an increase in CTA signal relative to doped background (black), meaning there is a CTA inclusion. In these intense CTA regions, additional peaks can be found supporting CTA inclusion beyond the ring deformation (i.e., ring breathing at 561 cm^{-1} and ring deformation at 1149 cm^{-1}). The 10% CTA TNT melt sample retains a mix of low and high levels of CTA within a 25 µm space, which is likely why these inclusions were not found with IR analysis, as the pure CTA likely overlaps with the doped signal in the host.

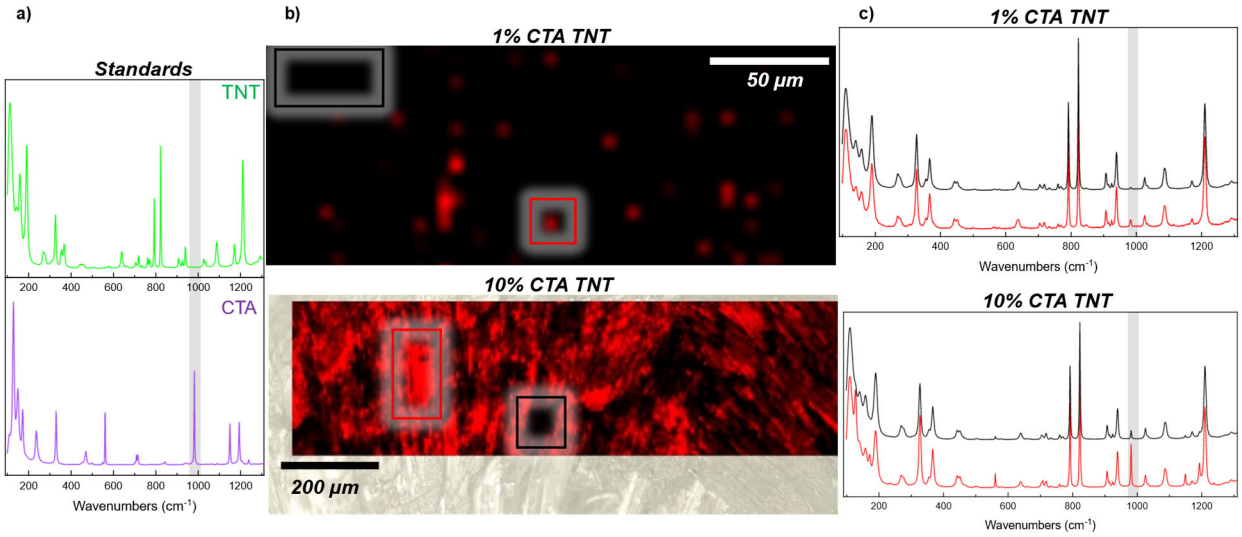


Figure 2.10 a) Raman spectra of TNT vs CTA, with the peak of interest highlighted by a grey box. b) Mapping of 1% vs. 10% CTA in TNT shows distribution of CTA (red) across melt. c) Representative spectra are shown for each loading based on regions of average CTA signal (black) and high CTA signal (red).

Uniformity analysis on 1% doped-CTA and 10% inclusion-CTA in TNAZ revealed similar results to that of TNT discussed above, with significant segmentation of CTA in the higher loaded sample (Figure 2.11). For DNAN, 1% and 2% CTA loadings were analyzed in addition to 10%, given the variability in maximum dopant loading value calculated from PXRD

pattern integration (Figure 2.12). For DNAN, the melt sample with 1% doped-CTA in DNAN showed dramatically less CTA clustering compared to either 2% or 10% inclusion-CTA loading. The 2% CTA in DNAN sample did show some larger areas of CTA incorporation, which was later identified in a spatially distinct region of the PXRD sample. Additional replicates of 2% CTA in DNAN melts showed difficulty achieving a uniformly mixed sample, with separation of the molten components when trying to load and crystallize the sample for PXRD analysis. As this problem did not arise with any of the other energetics, it is likely due to a miscibility issue between molten DNAN and CTA upon cooling, with some rejection occurring upon crystallization. It is important to note, however, that for all samples containing regions of phase separated CTA, there is a stabilizing effect arising from being encased in a layer of melt-cast energetic, minimizing the sensitivity risk relative to bulk CTA as an inclusion. Consideration of the mechanism of energetic detonation is also relevant with this finding, since a practical application of molecular doping is to impart impact sensitivity (a detonation event) to a less sensitive compound. The first stage of the detonation event is ignition often ascribed to hot spots, which are localized regions of heat that are converted to mechanical energy.[33,34] Because the localization of energy is physical, hot spots have been successfully correlated to and modeled by physical features (like heterogeneity from bubbles, impurities, defects, and gaps) in energetic samples.[35–39] Doping CTA into energetic hosts provides an additional model for hot spot ignition, and both incorporation modes (molecular doping and inclusions) provide the physical region needed for concentrating the mechanical energy into small areas for ignition.

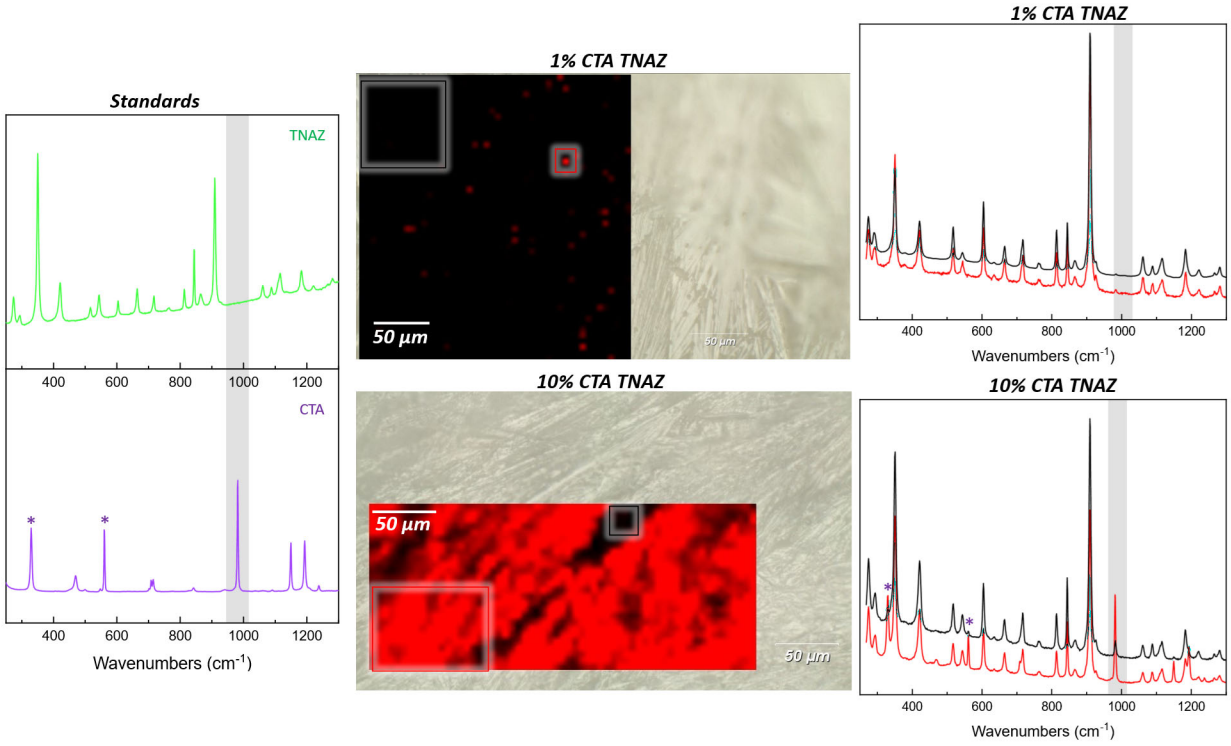


Figure 2.11 Raman spectra of TNAZ vs CTA, with peak of interest highlighted by a grey box. Mapping of 1% vs. 10% CTA in TNAZ shows distribution of CTA across melt. Representative spectra are shown for each loading based on regions of average CTA signal (color-coded black) and high CTA signal (color-coded red). Additional CTA peaks (*) can be found in higher concentration areas.

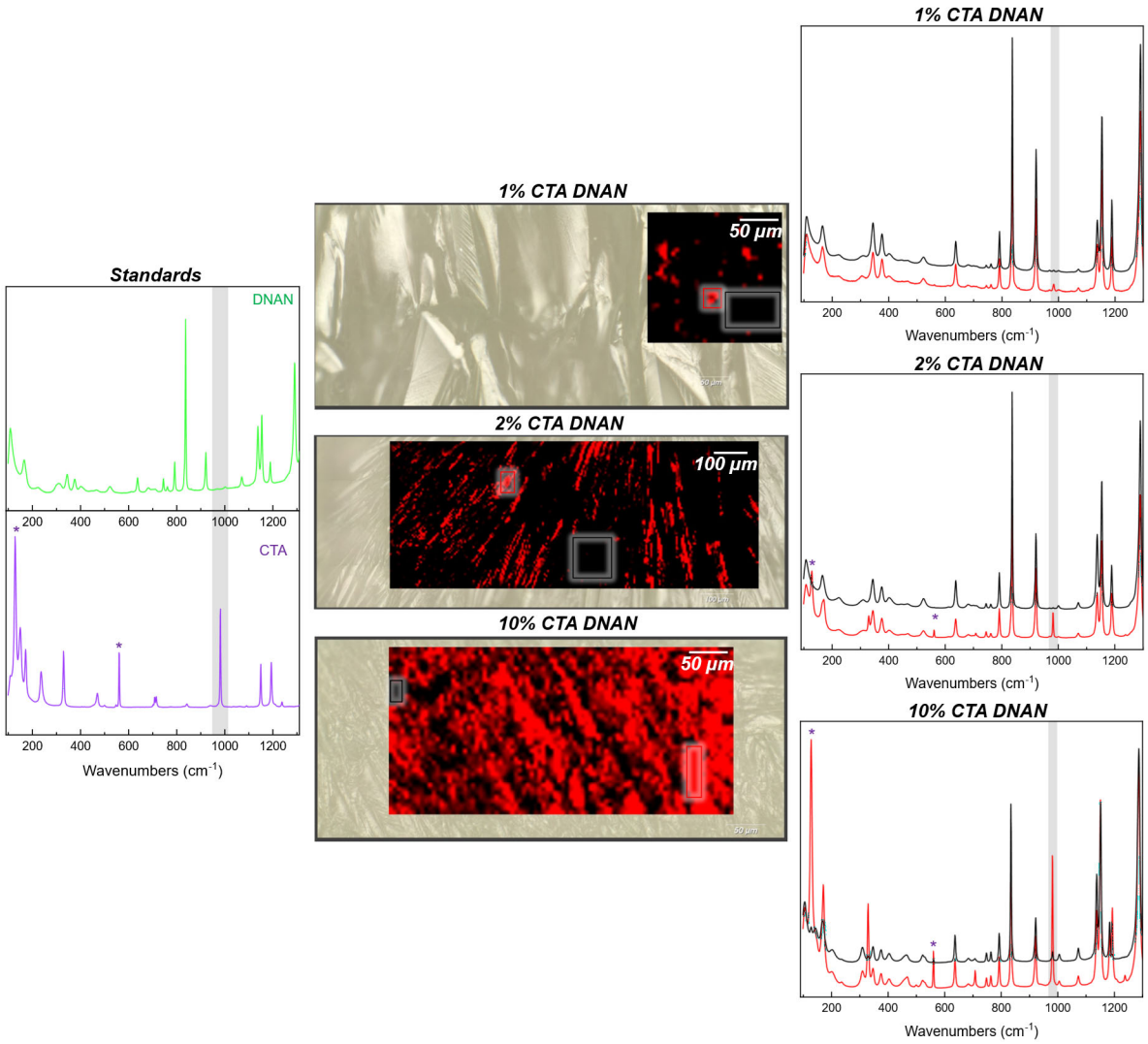


Figure 2.12 Raman spectra of DNAN vs CTA, with peak of interest highlighted by a grey box. Mapping of 1% vs. 2% vs. 10% CTA in DNAN shows distribution of CTA across melt. Representative spectra are shown for each loading based on regions of average CTA signal (color-coded black) and high CTA signal (color-coded red). Additional CTA peaks (*) can be found in higher concentration areas.

To test the hypothesis that impact sensitivity could be imparted to a host energetic by doping, drop testing was performed. Impact sensitivity is reported in terms of a drop height where there is a 50% probability of detonation occurring (termed Dh_{50}). Sensitivity and drop height are inverse, meaning compounds that are highly sensitive to impact can be detonated from low drop heights, whereas low sensitivity compounds are detonated from high drop heights. Understanding sensitivity of compounds is important in the handling and classification of

energetics, dictating their application space as a primary vs. secondary energetic.[40] The threshold for categorizing an energetic as a primary or secondary is a relative comparison of pentaerythritol tetranitrate (PETN), which has a Dh_{50} = 21 cm, to the compound.[41] Successful sensitization of all three energetic systems by molecular doping was confirmed (Figure 2.13). The Dh_{50} for pure TNT crystallized from the melt was 87 cm, while 1% doped-CTA in TNT had increased sensitivity (Dh_{50} = 83 cm). The Dh_{50} for pure TNAZ crystallized from melt was 21 cm, with 1% doped-CTA in TNAZ leading to Dh_{50} = 15 cm. With this example, the secondary energetic TNAZ has now gained the sensitivity to classify its use as a primary explosive based on a Dh_{50} lower than PETN, demonstrating a potential method for making metal-free primary explosives by doping. Melt-cast DNAN standard was not found to detonate on the apparatus tested (Dh_{50} > 141 cm), but impact sensitivity was imparted by molecular doping 1% CTA to achieve a Dh_{50} = 123 cm. Additional sensitivity was imparted with 2% CTA in DNAN (Dh_{50} = 119 cm). High loading levels with more segmented regions of CTA, or inclusions, did impart increased sensitivity beyond that of the sensitivity imparted with the molecular doping level (1%), as 10% CTA in DNAN yielded a Dh_{50} = 63 cm. It is important to reiterate that these properties are still not equivalent to bulk CTA (Dh_{50} = 12 cm)[11], which is a primary energetic that would be used to ignite the entire host system at its sensitivity threshold. This illustrates that sensitivity is synergistic in these multicomponent host-dopant systems.

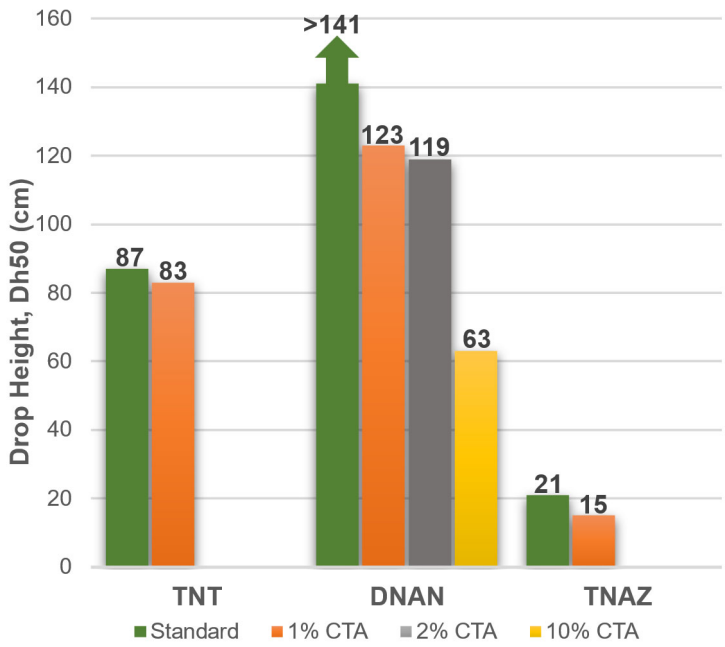


Figure 2.13 Impact sensitivity of pure vs. CTA-loaded compounds reported as Dh50, the drop height where there is a 50% probability of detonation.

2.4 Conclusion

Molecular doping of an impact sensitive primary energetic into a less sensitive secondary energetic increased impact sensitivity. This was achieved in three melt-castable energetics. Incorporation as an inclusion was also successful in sensitization of a secondary host energetic. Although segmentation of the sensitive primary energetic occurred, a stabilizing effect from the melt-cast layer reduced the sensitivity risk relative to bulk CTA. Doping has the potential for a workhorse energetic to be applied to different applications depending on the dopant. For example, with a judicious choice of dopant, tuning of material properties like responses to optical stimuli or improved detonations is possible. Doping would be particularly useful for energetics where identifying coformers has failed, or in instances were an energetic may be too dangerous or expensive to use on its own. Additionally, this approach opens the door for “green” metal-free primary energetics with reduced environmental and health concerns relative to toxic-metal containing primary energetics, which are still widely used. Lastly, this approach provides a way

to engineer a physical model for the hot spot mechanism of explosive ignition, an important field for understanding explosive performance that was established in the 1940s and that is still under active investigation today.[42–44]

2.5 Experimental Details

Warning! Although no unplanned detonations occurred during this work, CTA, TNT, DNAN, and TNAZ are explosives and should be handled appropriately. Proper safety practices are implemented to eliminate detonation from friction, heat, electrostatic discharge, impact, and flame. Extra caution is advised when handling CTA, a primary explosive with previous reports of spontaneous detonations.[45,46]

2.5.1 Sample Preparation

Host compound (TNT, DNAN, or TNAZ) was massed into a polypropylene microcentrifuge tube, and a corresponding amount of CTA (1.0-12.0 mol% CTA relative to host) was delivered on top via a CTA solution in ethyl acetate to minimize safety risks of handling bulk CTA. After evaporation of ethyl acetate with air, the microcentrifuge tube containing both compounds was placed into a pre-heated block, just above the melting point of the host (TNT @ ~88 °C, DNAN @ ~98 °C, TNAZ @ ~100°C). After 2-3 minutes to equilibrate, the contents were mixed with a hot glass rod (to prevent early crystallization before thorough mixing) and transferred onto a glass slide to allow for melt-crystallization to occur at room temperature. Typical sample scale was 2.0 to 55.0 mg.

2.5.2 Two-Dimensional Powder X-ray Diffraction

Melt samples were loaded into 0.31 mm inner diameter Kapton capillaries and mounted inside a Rigaku XtaLAB Synergy-S X-ray diffractometer, equipped with a PhotonJet-S microfocus Cu X-ray source (λ = 1.54184 Å) operated at 50 kV and 1 mA and a HyPix-6000HE

detector held 100 mm from the sample. Two-dimensional powder patterns were collected using Gandolfi moves for powders, with a reduced beam slit to 2% intensity for 2000 seconds in only positive positions for 2θ to 40°. Traditional one-dimensional powder patterns were extracted using CrysAlisPro v42.75a and analyzed in MDI JADE v8.8. Peak areas were calculated with Pseudo-Voigt fitting in small segments for maximum dopant loading calculation. The limit of detection (signal to noise (S/N) = 3/1) for PXRD was extrapolated based on the S/N of 10% CTA signal in TNT using the following equation, where H is the height of the peak and h is the range of the noise.

$$\frac{S}{N} = \frac{2H}{h}$$

2.5.3 Transmission Infrared Microspectroscopy

Infrared (IR) spectra of all samples were collected on calcium fluoride windows in transmission mode using a Thermo Fisher Scientific Nicolet iN10 MX IR Imaging Microscope with a liquid nitrogen cooled imaging IN10 Array detector. Spectra collection time was 5 s (16 scans) at 4 cm^{-1} spectral resolution from 4000 to 715 cm^{-1}, with a spatial resolution of one spectrum every 25 μm. Maps were processed using the OMNIC Picta software package. The data was profiled based on a peak area ratio between a host overtone band and the CTA region of interest (discussed in Section 2.3).

2.5.4 Raman Microspectroscopy

Raman spectra of CTA, TNT, DNAN, TNAZ, and doped DNAN or TNT samples on stainless steel plates were collected using a Renishaw inVia Raman spectrophotometer equipped with a Leica microscope, 633 nm laser, 1800 lines/mm grating, 50 μm slit size, and a Renishaw Centrus 2GRX02 detector. Spectra of pure components were collected in static scan mode from

99 to 1318 cm^{-1}. For doped samples, a static StreamHR map was collected with the same window using a 20× objective and 5 µm × 5 µm step size. Raman spectra of doped-TNAZ samples (also on stainless steel) were collected using a 785 nm laser, to improve signal-to-noise ratio and minimize fluorescence, with a Renishaw inVia Raman spectrophotometer equipped with a Leica microscope, 1200 lines/mm grating, 65 µm slit size, and a Renishaw CCD detector. Static StreamHR maps were collected from 268 to 1445 cm^{-1} using a 20× objective and 5 µm × 5 µm step size. Raman Spectra were analyzed using the WiRE 5.6 software (Renishaw). Non-Negative Least Squares (NNLS) component analysis was performed with a 2nd derivative method.

2.5.5 Impact Sensitivity

The impact sensitivity of each host compound, as well as the CTA-doped samples, were determined using an in-house apparatus utilizing a Bruceton-like up and down approach.[47] A 5 lb stainless-steel weight was dropped inside a polyvinyl chloride pipe-guided system from varying heights onto aluminum DSC pans containing ~2 mg of sample to subject the sample to impact force. Prior to testing, the ~2 mg samples were remelted and crystalized in the DSC pans to standardize sample morphology being impacted. The response of the sample was determined as "go" (sign of detonation) or "no-go" (no sign of detonation) based primarily on a visual light response, recorded with a phototransistor monitored by a Tektronix TBS1064 oscilloscope. At least 25 samples of each material were tested to calculate the Dh_{50}, the drop height where there was a 50% probability of detonation.

2.6 Acknowledgements

This work was supported by the ONR (Grant no. N00014-22-1-2101). S. T. Nicolau acknowledges the Science, Mathematics, and Research for Transformation (SMART) program for their support.

2.7 References

(1) Schultheiss, N.; Newman, A. Pharmaceutical Cocrystals and Their Physicochemical Properties. *Cryst. Growth Des.* **2009**, *9* (6), 2950–2967. https://doi.org/10.1021/cg900129f.

(2) Yadav, A. V.; Shete, A. S.; Dabke, A. P.; Kulkarni, P. V.; Sakhare, S. S. Co-Crystals: A Novel Approach to Modify Physicochemical Properties of Active Pharmaceutical Ingredients. *Indian J. Pharm. Sci.* **2009**, *71* (4), 359–370. https://doi.org/10.4103/0250-474X.57283.

(3) Kavanagh, O. N.; Croker, D. M.; Walker, G. M.; Zaworotko, M. J. Pharmaceutical Cocrystals: From Serendipity to Design to Application. *Drug Discov. Today* **2019**, *24* (3), 796–804. https://doi.org/10.1016/j.drudis.2018.11.023.

(4) Yousef, M. A. E.; Vangala, V. R. Pharmaceutical Cocrystals: Molecules, Crystals, Formulations, Medicines. *Cryst. Growth Des.* **2019**, *19* (12), 7420–7438. https://doi.org/10.1021/acs.cgd.8b01898.

(5) Duggirala, N. K.; Perry, M. L.; Almarsson, Ö.; Zaworotko, M. J. Pharmaceutical Cocrystals: Along the Path to Improved Medicines. *Chem. Commun.* **2015**, *52* (4), 640–655. https://doi.org/10.1039/C5CC08216A.

(6) Berry, D. J.; Steed, J. W. Pharmaceutical Cocrystals, Salts and Multicomponent Systems; Intermolecular Interactions and Property Based Design. *Adv. Drug Deliv. Rev.* **2017**, *117*, 3–24. https://doi.org/10.1016/j.addr.2017.03.003.

(7) Guo, M.; Sun, X.; Chen, J.; Cai, T. Pharmaceutical Cocrystals: A Review of Preparations, Physicochemical Properties and Applications. *Acta Pharm. Sin. B* **2021**, *11* (8), 2537–2564. https://doi.org/10.1016/j.apsb.2021.03.030.

(8) Rodrigues, M.; Baptista, B.; Lopes, J. A.; Sarraguça, M. C. Pharmaceutical Cocrystallization Techniques. Advances and Challenges. *Int. J. Pharm.* **2018**, *547* (1), 404–420. https://doi.org/10.1016/j.ijpharm.2018.06.024.

(9) Zaworotko, M. J. Molecules to Crystals, Crystals to Molecules ... and Back Again? *Cryst. Growth Des.* **2007**, *7* (1), 4–9. https://doi.org/10.1021/cg0680172.

(10) Desiraju, G. R. Supramolecular Synthons in Crystal Engineering—A New Organic Synthesis. *Angew. Chem. Int. Ed. Engl.* **1995**, *34* (21), 2311–2327. https://doi.org/10.1002/anie.199523111.

(11) Foroughi, L. M.; Wiscons, R. A.; Bois, D. R. D.; Matzger, A. J. Improving Stability of the Metal-Free Primary Energetic Cyanuric Triazide (CTA) through Cocrystallization. *Chem. Commun.* **2020**, *56* (14), 2111–2114. https://doi.org/10.1039/C9CC09465B.

(12) Bellas, M. K.; Matzger, A. J. Achieving Balanced Energetics through Cocrystallization. *Angew. Chem. Int. Ed.* **2019**, *58* (48), 17185–17188. https://doi.org/10.1002/anie.201908709.
(13) Landenberger, K. B.; Matzger, A. J. Cocrystal Engineering of a Prototype Energetic Material: Supramolecular Chemistry of 2,4,6-Trinitrotoluene. *Cryst. Growth Des.* **2010**, *10* (12), 5341–5347. https://doi.org/10.1021/cg101300n.
(14) Aakeröy, C. B.; Wijethunga, T. K.; Desper, J. Crystal Engineering of Energetic Materials: Co-Crystals of Ethylenedinitramine (EDNA) with Modified Performance and Improved Chemical Stability. *Chem. – Eur. J.* **2015**, *21* (31), 11029–11037. https://doi.org/10.1002/chem.201501721.
(15) Ungnade, H. E.; Roberts, E. M.; Kissinger, L. W. Hydrogen Bonding in Nitro Compounds1. *J. Phys. Chem.* **1964**, *68* (11), 3225–3228. https://doi.org/10.1021/j100793a024.
(16) Gamekkanda, J. C.; Sinha, A. S.; Aakeröy, C. B. Cocrystals and Salts of Tetrazole-Based Energetic Materials. *Cryst. Growth Des.* **2020**, *20* (4), 2432–2439. https://doi.org/10.1021/acs.cgd.9b01620.
(17) Liu, Y.; Li, S.; Xu, J.; Zhang, H.; Guan, Y.; Jiang, H.; Huang, S.; Huang, H.; Wang, Z. Three Energetic 2,2′,4,4′,6,6′-Hexanitrostilbene Cocrystals Regularly Constructed by H-Bonding, π-Stacking, and van Der Waals Interactions. *Cryst. Growth Des.* **2018**, *18* (4), 1940–1943. https://doi.org/10.1021/acs.cgd.8b00019.
(18) Bennion, J. C.; Matzger, A. J. Development and Evolution of Energetic Cocrystals. *Acc. Chem. Res.* **2021**. https://doi.org/10.1021/acs.accounts.0c00830.
(19) Bolton, O.; Matzger, A. J. Improved Stability and Smart-Material Functionality Realized in an Energetic Cocrystal. *Angew. Chem.* **2011**, *123* (38), 9122–9125. https://doi.org/10.1002/ange.201104164.
(20) Kent, R. V.; Wiscons, R. A.; Sharon, P.; Grinstein, D.; Frimer, A. A.; Matzger, A. J. Cocrystal Engineering of a High Nitrogen Energetic Material. *Cryst. Growth Des.* **2018**, *18* (1), 219–224. https://doi.org/10.1021/acs.cgd.7b01126.
(21) Chapman, C. J.; Groven, L. J. Evaluation of Solvate and Co-Crystal Screening Methods for CL-20 Containing Energetic Materials. *J. Energ. Mater.* **2022**, *40* (3), 258–272. https://doi.org/10.1080/07370652.2020.1867936.
(22) Capellades, G.; O. Bonsu, J.; S. Myerson, A. Impurity Incorporation in Solution Crystallization: Diagnosis, Prevention, and Control. *CrystEngComm* **2022**, *24* (11), 1989–2001. https://doi.org/10.1039/D1CE01721G.
(23) Urwin, S. J.; Levilain, G.; Marziano, I.; Merritt, J. M.; Houson, I.; Ter Horst, J. H. A Structured Approach To Cope with Impurities during Industrial Crystallization Development. *Org. Process Res. Dev.* **2020**, *24* (8), 1443–1456. https://doi.org/10.1021/acs.oprd.0c00166.
(24) Urwin, S. J.; Yerdelen, S.; Houson, I.; ter Horst, J. H. Impact of Impurities on Crystallization and Product Quality: A Case Study with Paracetamol. *Crystals* **2021**, *11* (11), 1344. https://doi.org/10.3390/cryst11111344.
(25) Shearer, S. J.; Turrell, G. C.; Bryant, J. I.; Brooks, R. L. Vibrational Spectra of Cyanuric Triazide. *J. Chem. Phys.* **1968**, *48* (3), 1138–1144. https://doi.org/10.1063/1.1668774.
(26) Ravi, P.; Badgujar, D. M.; Gore, G. M.; Tewari, S. P.; Sikder, A. K. Review on Melt Cast Explosives. *Propellants Explos. Pyrotech.* **2011**, *36* (5), 393–403. https://doi.org/10.1002/prep.201100047.

(27) Doherty, R. M.; Watt, D. S. Relationship Between RDX Properties and Sensitivity. *Propellants Explos. Pyrotech.* **2008**, *33* (1), 4–13. https://doi.org/10.1002/prep.200800201.
(28) Borne, L.; Ritter, H. HMX as an Impurity in RDX Particles: Effect on the Shock Sensitivity of Formulations Based on RDX. *Propellants Explos. Pyrotech.* **2006**, *31* (6), 482–489. https://doi.org/10.1002/prep.200600066.
(29) Fondren, N. S.; Fondren, Z. T.; Unruh, D. K.; Weeks, B. L. Effects of Solution Conditions on Polymorph Development in 2,4,6-Trinitrotoluene. *Cryst. Growth Des.* **2020,** *20* (2), 568–579. https://doi.org/10.1021/acs.cgd.9b00722.
(30) Meenan, P. A.; Anderson, S. R.; Klug, D. L. 3 - The Influence of Impurities and Solvents on Crystallization. In *Handbook of Industrial Crystallization (Second Edition)*; Myerson, A. S., Ed.; Butterworth-Heinemann: Woburn, 2002; pp 67–100. https://doi.org/10.1016/B978-075067012-8/50005-7.
(31) Denekamp, C.; Meikler, O.; Zelner, M.; Suwinska, K.; Eichen, Y. Controlling the Crystal Morphology and Polymorphism of 2,4-Dinitroanisole. *Cryst. Growth Des.* **2018**, *18* (3), 1350–1357. https://doi.org/10.1021/acs.cgd.7b01199.
(32) McKenney, R. L.; Stevens, W. E.; Floyd, T. G. Binary Phase Diagram Series: 1,3,3-Trinitroazetidine (TNAZ)/2,4,6-Trinitrotoluene (TNT). *J. Energ. Mater.* **1998**, *16* (4), 245–277. https://doi.org/10.1080/07370659808230234.
(33) Field, J. E. Hot Spot Ignition Mechanisms for Explosives. *Acc. Chem. Res.* **1992**, *25* (11), 489–496. https://doi.org/10.1021/ar00023a002.
(34) Bowden, F. P.; Yoffe, A. D. *Initiation and Growth of Explosion in Liquids and Solids*; CUP Archive, 1985.
(35) Afanas'ev, G. T.; Bobolev, V. K.; Kazarova, Yu. A.; Karabanov, Yu. F. Formation of Local Hot Spots during the Fracture of Thin Layers under Shock. *Combust. Explos. Shock Waves* **1972**, *8* (2), 241–246. https://doi.org/10.1007/BF00740454.
(36) Coffey, C. S. Phonon Generation and Energy Localization by Moving Edge Dislocations. *Phys. Rev. B* **1981**, *24* (12), 6984–6990. https://doi.org/10.1103/PhysRevB.24.6984.
(37) Mintmire, J. W.; Robertson, D. H.; White, C. T. Molecular-Dynamics Simulations of Void Collapse in Shocked Model-Molecular Solids. *Phys. Rev. B* **1994**, *49* (21), 14859–14864. https://doi.org/10.1103/PhysRevB.49.14859.
(38) Shi, Y.; Brenner, D. W. Molecular Simulation of the Influence of Interface Faceting on the Shock Sensitivity of a Model Plastic Bonded Explosive. *J. Phys. Chem. B* **2008**, *112* (47), 14898–14904. https://doi.org/10.1021/jp805690w.
(39) Armstrong, R. W. Dislocation Viscoplasticity Aspects of Material Fracturing. *Eng. Fract. Mech.* **2010**, *77* (8), 1348–1359. https://doi.org/10.1016/j.engfracmech.2010.02.019.
(40) *Recommendations on the Transport of Dangerous Goods - Manual of Tests and Criteria.* Hauptbd., 5., rev. ed.; Vereinte Nationen, Ed.; ST/SG/AC.10; United Nations: New York, 2009.
(41) Kent, R. V.; Vaid, T. P.; Boissonnault, J. A.; Matzger, A. J. Adsorption of Tetranitromethane in Zeolitic Imidazolate Frameworks Yields Energetic Materials. *Dalton Trans.* **2019**, *48* (22), 7509–7513. https://doi.org/10.1039/C9DT01254K.
(42) Blum-Sorensen, C. J.; Duarte, C. A.; Drake, J. D.; Kerschen, N. E.; Fezzaa, K.; Koslowski, M.; Chen, W. W.; Son, S. F. Phase Contrast X-Ray Imaging of the Collapse of an Engineered Void in Single-Crystal HMX. *Propellants Explos. Pyrotech.* **2022**, *47* (10), e202100297. https://doi.org/10.1002/prep.202100297.

(43) Armstrong, M.; Bukovsky, E.; Shaw, W.; Austin, R.; Grivickas, P.; Hodgin, R.; Sinclair, N.; Klug, J.; Willey, T.; Zaug, J. *Time-resolved X-ray Imaging of Void Collapse in Silicone and TNT*. https://www.osti.gov/biblio/1489458.
(44) McGrane, S. D.; Grieco, A.; Ramos, K. J.; Hooks, D. E.; Moore, D. S. Femtosecond Micromachining of Internal Voids in High Explosive Crystals for Studies of Hot Spot Initiation. *J. Appl. Phys.* **2009**, *105* (7), 073505. https://doi.org/10.1063/1.3091270.
(45) Matyáš, R.; Pachman, J. *Primary Explosives*; Springer: Berlin, Heidelberg, 2013. https://doi.org/10.1007/978-3-642-28436-6.
(46) *Engineering Design Handbook Explosives Series Properties of Explosives of Military Interest*. https://apps.dtic.mil/sti/tr/pdf/AD0764340.pdf (accessed 2023-10-10).
(47) Bennion, J. C.; Chowdhury, N.; Kampf, J. W.; Matzger, A. J. Hydrogen Peroxide Solvates of 2,4,6,8,10,12-Hexanitro-2,4,6,8,10,12-Hexaazaisowurtzitane. *Angew. Chem. Int. Ed*. **2016**, *55* (42), 13118–13121. https://doi.org/10.1002/anie.201607130.

Chapter 3 An Evaluation of Resolution, Accuracy, and Precision in FT-IR Spectroscopy

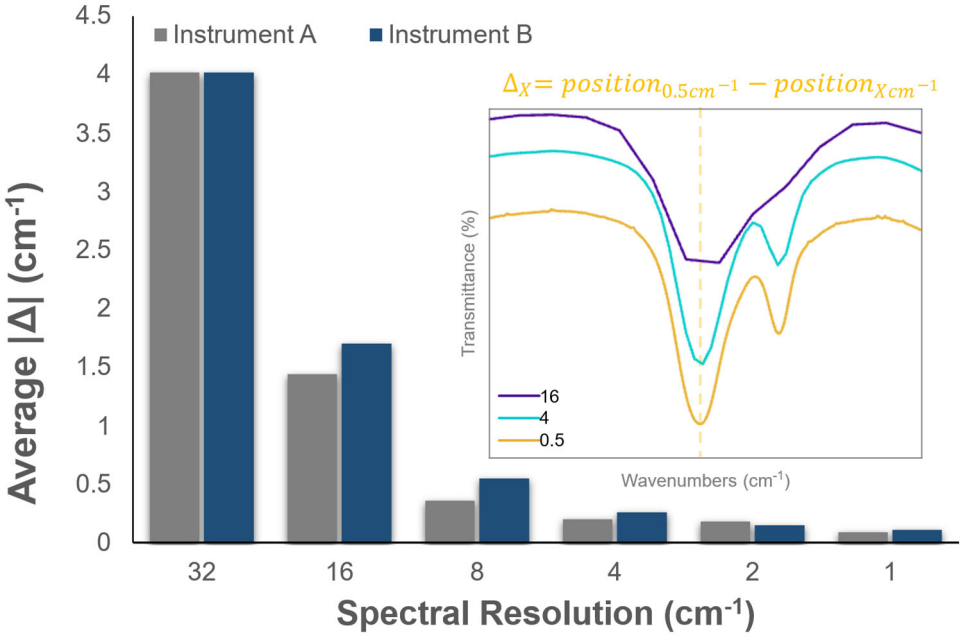


Figure 3.1 An experimental study of polystyrene and acetaminophen determined resolution and instrument variation have minor effects on well-resolved peak positions.

3.1 Publication of Chapter

Nicolau, S. T.; Matzger, A. J. An Evaluation of Resolution, Accuracy, and Precision in FT-IR Spectroscopy. *Spectrochim. Acta. A. Mol. Biomol. Spectrosc.* **2024**, *319*, 124545. https://doi.org/10.1016/j.saa.2024.124545.

3.2 Introduction

For over 100 years infrared spectroscopy has been a foundational technique for the elucidation of chemical structure.[1,2] Since the time of William W. Coblentz (1873-1962), famously known for the collection of infrared spectra of over 130 compounds, major advances have been made not only in the compilation of spectral libraries[3,4] and predictive functional

group trends[5–8] but also in the instrumentation itself.[9,10] The original Coblentz alkali halide prism has long since been replaced; dispersive spectroscopy (prisms and gratings) is now nearly obsolete in reference to the mid infrared region (4000-400 cm^{-1}) due to the advances in interferometric spectroscopy.[11,12] Technological advances have driven down the price and size of infrared spectrometers to the point where they are ubiquitous in areas from introductory teaching labs[13–19] to critical applications in quality control.[20–24]

Perhaps the most fundamental advancement to allow for repeatable collection of infrared spectra with an excellent signal-to-noise ratio (SNR) is the introduction of Fourier transform infrared (FT-IR) spectroscopy in the 1960s.[12] High (>100) SNRs are routinely achieved due to two well documented advantages of FT-IR: the throughput (or Jacquinot's) advantage and the multiplex (Fellgett's) advantage.[12,25,26] In brief, a large circular aperture allows for a higher throughput of radiation compared to traditional slits, while simultaneously recording all frequencies that strike the detector.[27] Aside from improved SNR to permit highly sensitive detection and quantitative accuracy, an additional FT-IR advantage (Connes') allows for high wavenumber precision. This is afforded by calibrating the wavelength scale to that of a precise reference laser frequency, offering, at least in principle, determination of peak positions to within 0.01 cm^{-1}.[11,12,27] Of course, in practice, other factors may limit wavenumber accuracy and one of these that has been mentioned is resolution. To adequately resolve bands, the general rule of thumb is to collect at resolutions smaller than the full width at half maximum of the bands.[11]

It has reasonably been suggested that instrument-to-instrument variation may also lead to additional uncertainties in wavenumber accuracy, although the magnitudes of these differences have not been determined. The United States Pharmacopeia (USP) monograph on general spectroscopy and light scattering principles states in its 2012 and 2014 versions of <851> that

"values may vary as much as 0.1 mm or 10 cm^{-1}, depending upon the particular instrument used".[28] While this chapter of the USP monograph has since been revised to reflect improvements in spectroscopy on a technique-by-technique basis (<854>)[29], any language regarding this type of positional variation has been omitted beyond general statements regarding acceptable tolerances when calibrating to a polystyrene standard.[30] Considering that USP monographs are relied on for regulatory compliance[31], and have been used[32] or needed[33] in legal proceedings to define acceptable measurement error, the lack of clear guidance is problematic. Few textbooks address this issue, with at least two stating that wavenumber accuracy is equal to ± half the spectral resolution (meaning, for a band collected at 4 cm^{-1} resolution, position can be known within ± 2 cm^{-1}).[11,25] However, this conflates accuracy with the digitized data spacing increments.[11] A clear recommendation on determining peak position accuracy and the associated variations that might typically be encountered is needed.

Herein, we conduct an experimental study of the effect of resolution on positional peak accuracy and assess the variation across instruments. We demonstrate that, in most circumstances, resolution has a minor effect on peak position and that the USP <851> estimate for instrument-to-instrument variation is off by an order of magnitude. Furthermore, equating the uncertainty to half the spectral resolution, while generally predicting an accuracy greater than 10 wavenumbers, improperly implies that IR spectroscopy lacks utility in cases where only subtle changes take place, as is often the case for assessing crystal polymorphism and cocrystal or salt formation by IR positional variations.[34–41]

Two substances were employed in this study: polystyrene and acetaminophen. Polystyrene (PS) is used as a NIST traceable film standard to evaluate FT-IR performance[30], which enables discussion of the accuracy and precision of band position, as well as assessment of

instrument variation among some of the leading FT-IR spectrometer manufactures. Acetaminophen (APAP, also known as paracetamol) is a widely used fever and pain modifier with a spectrally dense IR-region to illustrate the power of adequate resolution settings and address reproducibility within the context of a pharmaceutical displaying crystal polymorphism.[42] Additionally, APAP is a useful and easily accessible compound for teaching IR theory and implementation in introductory labs.[43,44]

3.3 Results and Discussion

As accuracy and precision are often used interchangeably in the IR literature, nomenclature centered around current USP language to distinguish between the two is adopted.[45] Accuracy is defined as "the closeness of test results obtained by that procedure to the true value" and is determined by comparison to a reference standard, whereas precision is the "degree of agreement among individual test results when the procedure is applied repeatedly". Here, precision can be measured in two different contexts: reproducibility (in different laboratories/instruments) and repeatability (tolerance in a repeated measurement).

The ability to resolve major bands, as well as define the genuine relationship between resolution and wavenumber accuracy, is presented first with PS surveyed across 7 different spectral resolution settings (Figure 3.2). PS spectra collected on the Nicolet iS50 in the full spectral window are presented in Figure 3.2a, noting that several of the primary bands are nearly saturated for the 1.5 mil film used for calibration. Although there can be benefits to collecting at low resolutions like 32 or 16 cm^{-1} (e.g., fast mapping by IR microspectroscopy or kinetic measurements requiring sub-second temporal resolution), loss of spectral data is possible, as is illustrated in Figure 3.2b where several of the aromatic C-H stretching bands of PS are unresolved. Overlays of the various resolutions demonstrate that, for resolved bands, peak

positions vary little as a function of resolution. For example, the peak position of the aromatic C-H out-of-plane bend for PS at 757 cm^{-1} has a wavenumber variation within 2 cm^{-1}, despite collecting across a wide range of spectral resolutions (Figure 3.2c). Assuming that the accuracy is limited by digital resolution implies a maximum error of 16 cm^{-1} (when collected at the lowest spectral resolution of 32 cm^{-1}), a value much higher than the experimental variation shown for this peak. Adequate spectral resolution can be important in differentiating among polymorphs, illustrated in Figure 3.3. APAP when collected at 32 and 16 cm^{-1} fails to resolve three bands at 1260, 1243, and 1226 cm^{-1}, used to distinguish Form I (vs. two bands in region for Form II). A single a distinguishable band at 1610 cm^{-1} (vs. two bands, Form II) also denotes Form I.[42]

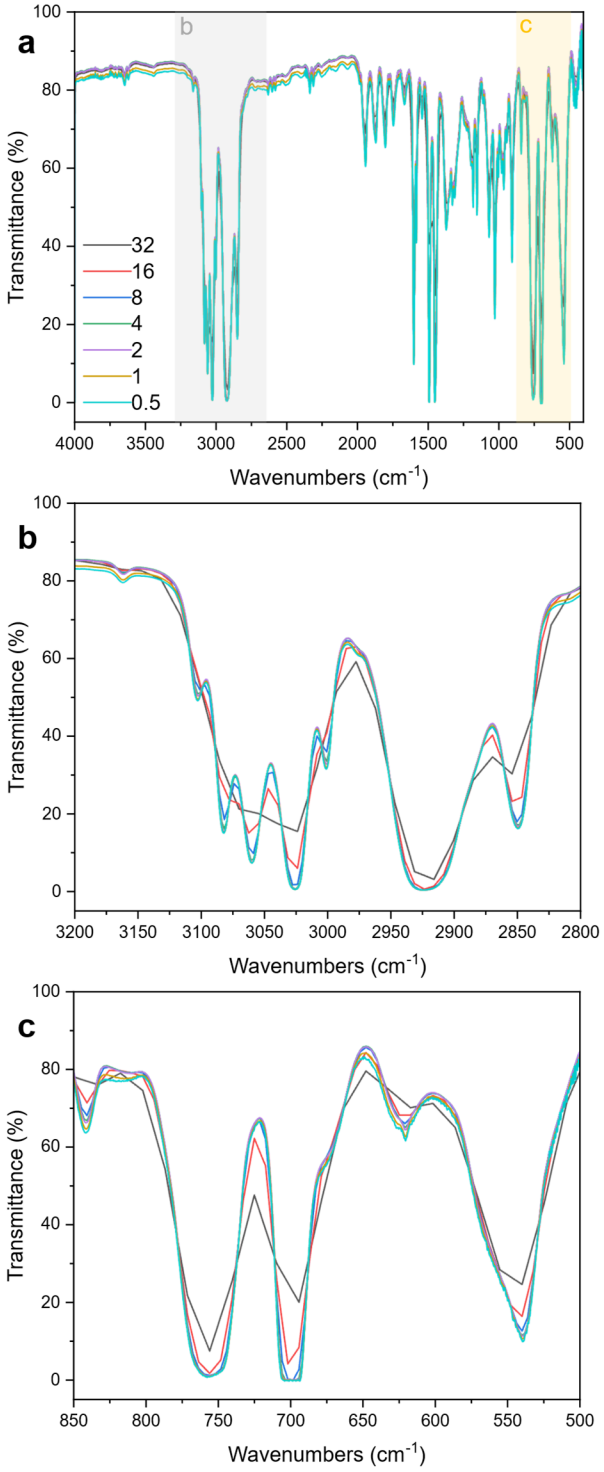


Figure 3.2 Spectral resolution effect on resolving polystyrene (PS) peaks collected by transmission FT-IR. (a) Full spectral window with varied spectral resolutions from 32 – 0.5 cm^{-1}. Boxes highlight zoomed in regions for b and c. (b) PS region with poorly resolved peaks at low resolutions (32, 16 cm^{-1}). (c) PS region with well resolved peaks at all resolutions.

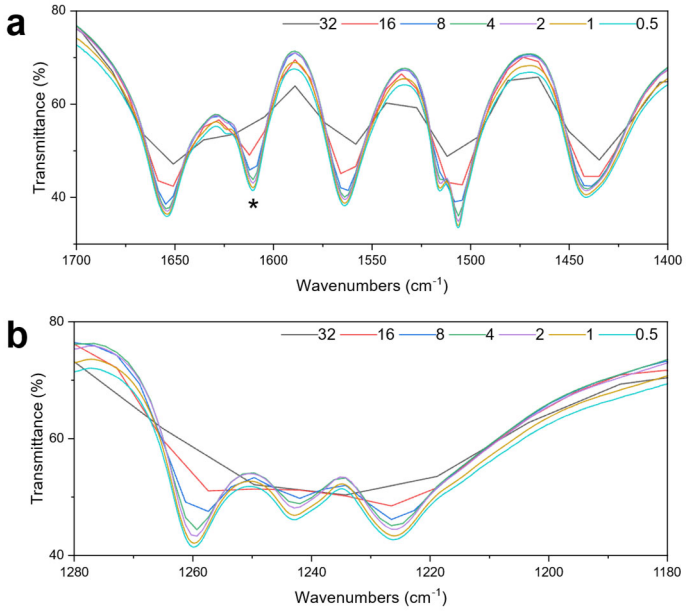


Figure 3.3 Spectral resolution effect (32 – 0.5 cm^{-1}) on resolving acetaminophen (APAP) peaks useful for polymorph differentiation. One (a) single band at 1610 cm^{-1} (denoted by *) and (b) three resolved bands at 1260, 1243, and 1226 cm^{-1} denote Form I, only accomplished at spectral resolutions of 8 cm^{-1} or higher.

Analysis of a NIST traceable secondary PS standard allows for comment on the wavenumber accuracy of several peaks to a standard reference value collected at 4 cm^{-1} spectral resolution. Additionally, the precision of positional variation in this PS standard is tested in terms of reproducibility in three other laboratories, testing instrument-to-instrument variation on Bruker, PerkinElmer, and Shimadzu models. For this study, 9 PS bands were taken into consideration based on the Nicolet and NIST polystyrene standard traceability document (see Appendix B): 3081.87, 3059.71, 3025.64, 2849.28, 1942.64, 1601.15, 1028.41, 906.62, and 539.63 cm^{-1}. When comparing the Nicolet data to the NIST values for the PS standard, the accuracy of the peak positions is within 0.1 cm^{-1} (Table 3-1). This accuracy does not constitute a general recommendation for expected accuracy, however, because there is additional variability in determining peak positions based on instrument models. Bruker and PerkinElmer models have

a larger uncertainty in PS bands positions compared to Nicolet. Accounting for some of the leading competitors in IR spectrometers discussed thus far, including Shimadzu, a general recommendation can be given that the peak position is still precise within 0.6 cm^{-1} for well resolved peaks collected at 4 cm^{-1} spectral resolution. The larger variation in peak 3 when collected on the Shimadzu is the result of a low transmittance region (high absorbance) becoming less Lorentzian and introducing sidelobes (Figure 3.4).[12] The side lobes are inaccurately picked when the peak pick function is applied instead of the peak center. Maintaining transmittance values higher than 10% can help eliminate issues with saturated peaks.[25] However, the introduction of sidelobes was instrument dependent, only occurring in data collected on the Shimadzu system. To standardize any variation in peak positions based on the peak-picking function, all data sets were analyzed in the Nicolet OMNIC software; however, assessment in the instrument's vendor-supplied software under standard parameters leads to a similar conclusion regarding precision and accuracy for PS (Table B-1). To assess peak position variation across resolutions, as well as incorporate APAP (without NIST traceability), a new term was assigned: Δ. The excellent agreement between the NIST data for PS collected on the same instrument suggests that this Δ value closely approximates the difference in accuracy.

Table 3-1 Peak accuracy (cm^{-1})[I] for 9 PS NIST calibration peaks collected on four FT-IR instruments at 4 cm^{-1} spectral resolution. [I]Wavenumbers were determined in OMNIC using the standard peak picking function.

	NIST	**Nicolet**	**Bruker**	**Perkin-Elmer**	**Shimadzu**	**NIST-Nicolet**	**NIST-Bruker**	**NIST-PerkinElmer**	**NIST-Shimadzu**
Peak 1	3081.87	3081.82	3081.35	3082.16	3081.36	0.05	0.52	-0.29	0.51
Peak 2	3059.71	3059.73	3059.38	3060.18	3059.22	-0.02	0.33	-0.47	0.49
Peak 3	3025.64	3025.73	3025.47	3026.18	3023.40[lobed]	-0.09	0.17	-0.54	2.24
Peak 4	2849.28	2849.38	2849.20	2849.85	2848.95	0.10	0.08	-0.57	0.33
Peak 5	1942.64	1942.67	1942.47	1942.98	1942.38	-0.03	0.17	-0.34	0.26
Peak 6	1601.15	1601.15	1600.80	1601.39	1600.88	0.00	0.35	-0.24	0.27
Peak 7	1028.41	1028.41	1028.08	1028.54	1028.26	0.00	0.33	-0.13	0.15
Peak 8	906.62	906.52	906.30	906.64	906.38	0.10	0.32	-0.02	0.24
Peak 9	539.63	539.75	539.67	539.79	539.51	-0.12	-0.04	-0.16	0.12

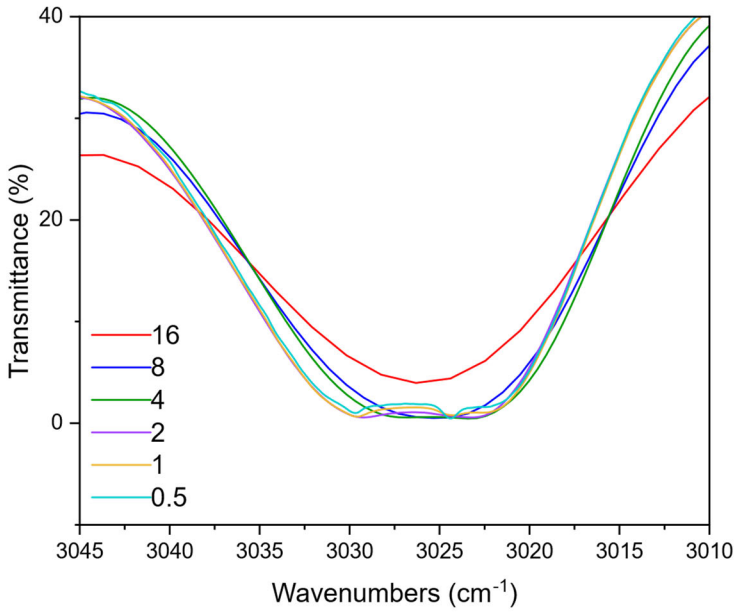


Figure 3.4 Transmission FT-IR of PS collected on a Shimadzu IRTracer-100 of a saturated peak with sidelobe generation at spectral resolutions higher than 8 cm^{-1}, increasing error in peak position at ~3025 cm^{-1}.

If one assumes that the uncertainties in a peak position decrease with increased spectral resolution, then the peak position assigned at 0.5 cm^{-1} should be closest to the true value of the band. Positions of 9 PS bands (labeled in Figure 3.5) were determined in the Nicolet system from 32 – 0.5 cm^{-1} (Table 3-2). If all features in a given region could not be resolved, the peaks were given the notation 'NR.' Peak position as a function of resolution is assessed in Table 3-3, by determining the difference, Δ, in the peak position at a given resolution from the value at 0.5 cm^{-1}. For a spectral resolution of 8 cm^{-1} or higher, Δ is within 1.0 cm^{-1} for PS on the Nicolet system, a number far lower than expected from the limit of digital resolution and consistent with a peak picking algorithm not limited to selecting the highest data point. Successive increases in spectral resolution above 8 cm^{-1} continually improved the uncertainty in the peak positions (peak position within 0.4 cm^{-1} for 4 cm^{-1} spectral resolution, within 0.4 cm^{-1} for 2 cm^{-1}, and within 0.3 cm^{-1} for 1 cm^{-1}). For 16 and 32 cm^{-1} spectral resolutions, Δ is still within 2.7 cm^{-1} and 8.8 cm^{-1}, respectively.

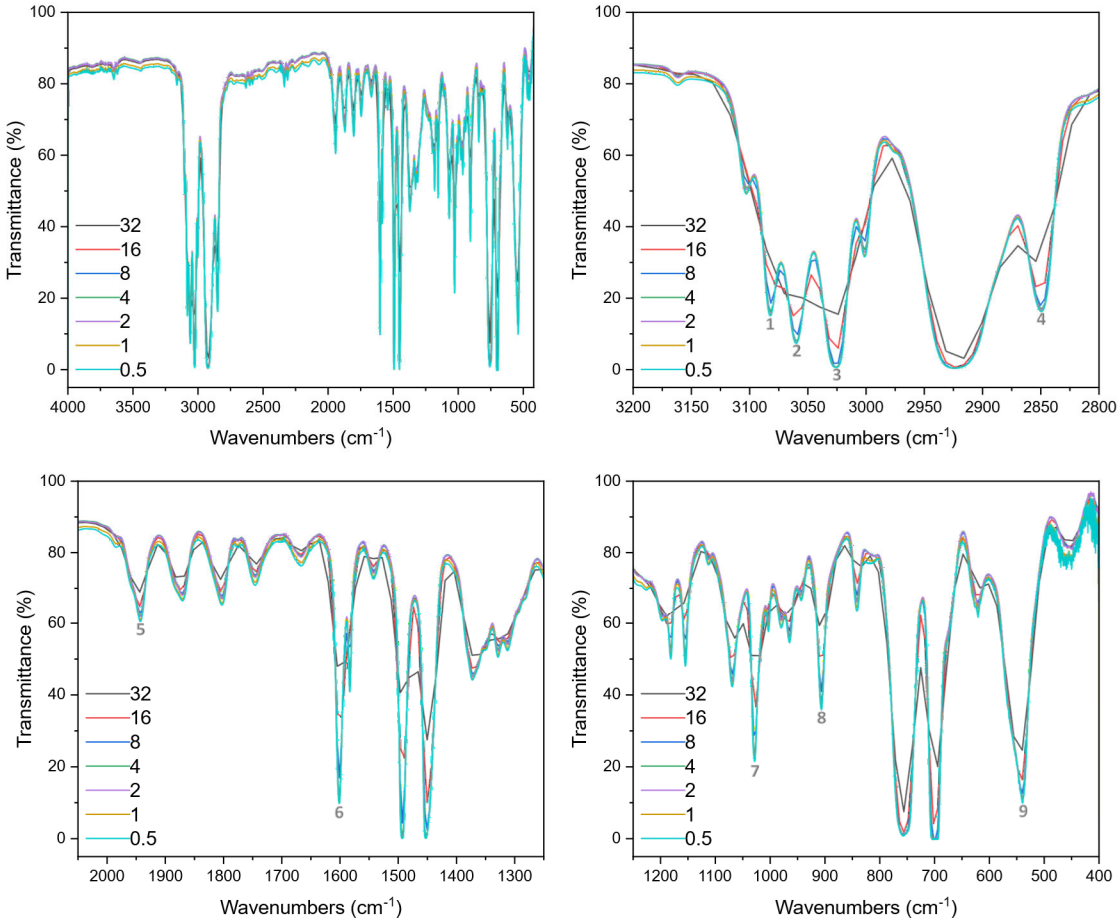


Figure 3.5 Transmission FT-IR spectra of PS collected on a Nicolet iS50 with varied spectral resolutions from 32 – 0.5 cm^{-1}. Numbering denotes peaks in analysis.

Table 3-2 Peak positions (cm^{-1}) [ŧ] for PS collected on a Nicolet iS50 FT-IR at variable spectral resolutions. [ŧ]Wavenumbers were determined in OMNIC using the standard peak picking function. [ǂ]NR denotes peak that were unresolved at said resolution.

	32 cm^{-1}	**16 cm^{-1}**	**8 cm^{-1}**	**4 cm^{-1}**	**2 cm^{-1}**	**1 cm^{-1}**	**0.5 cm^{-1}**
Peak 1	NR [ǂ]	NR	3081.26	3081.82	3081.95	3082.13	3082.25
Peak 2	NR	NR	3059.69	3059.73	3059.74	3059.88	3059.88
Peak 3	NR	NR	3025.93	3025.73	3025.70	3025.77	3025.72
Peak 4	2858.35	2851.04	2849.84	2849.38	2849.34	2849.43	2849.52
Peak 5	1945.81	1944.59	1943.12	1942.67	1942.64	1942.84	1943.02
Peak 6	1597.72	1600.15	1600.95	1601.15	1601.13	1601.20	1601.28
Peak 7	1025.93	1026.74	1028.18	1028.41	1028.27	1028.21	1028.18
Peak 8	907.30	906.59	906.58	906.52	906.50	906.52	906.26
Peak 9	545.33	542.35	540.48	539.75	539.61	539.72	539.69

Table 3-3. Peak position (cm^{-1}) as a function of resolution for PS as assessed by calculating the difference in assigned peak value from the value determined at 0.5 cm^{-1} (e.g. $\Delta 32\ cm^{-1} = peak_{0.5cm\text{-}1} - peak_{32cm\text{-}1}$). [ǂ]NR denotes peak that were unresolved at said resolution.

	Δ32 cm^{-1}	**Δ16 cm^{-1}**	**Δ8 cm^{-1}**	**Δ4 cm^{-1}**	**Δ2 cm^{-1}**	**Δ1 cm^{-1}**	**0.5 cm^{-1}**
Peak 1	NR[ǂ]	NR	0.99	0.43	0.30	0.12	3082.25 cm^{-1}
Peak 2	NR	NR	0.19	0.15	0.14	0.00	3059.88 cm^{-1}
Peak 3	NR	NR	-0.21	-0.01	0.02	-0.05	3025.72 cm^{-1}
Peak 4	-8.83	-1.52	-0.32	0.14	0.18	0.09	2849.52 cm^{-1}
Peak 5	-2.79	-1.57	-0.10	0.35	0.38	0.18	1943.02 cm^{-1}
Peak 6	3.56	1.13	0.33	0.13	0.15	0.08	1601.28 cm^{-1}
Peak 7	2.25	1.44	0.00	-0.23	-0.09	-0.03	1028.18 cm^{-1}
Peak 8	-1.04	-0.33	-0.32	-0.26	-0.24	-0.26	906.26 cm^{-1}
Peak 9	-5.64	-2.66	-0.79	-0.06	0.08	-0.03	539.69 cm^{-1}
Average |Δ|	**4.02**	**1.44**	**0.36**	**0.20**	**0.18**	**0.09**	**-**

A similar trend was established with APAP using the Nicolet system for analysis of 9 selected bands (Figure 3.6, Table 3-4), with spectral resolutions higher than 8 cm^{-1} providing the smallest Δ values. For well resolved bands, Δ was found to be within 1.6 cm^{-1} for resolutions of 8 cm^{-1} or higher, within 2.3 cm^{-1} for 16 cm^{-1}, and within 3.2 cm^{-1} for 32 cm^{-1} spectral resolution (Table 3-5). These numbers represent the extremes of deviation caused by resolution. The average deviations are much lower than this and are expressed in the tables as the average of the absolute values (average |Δ|).

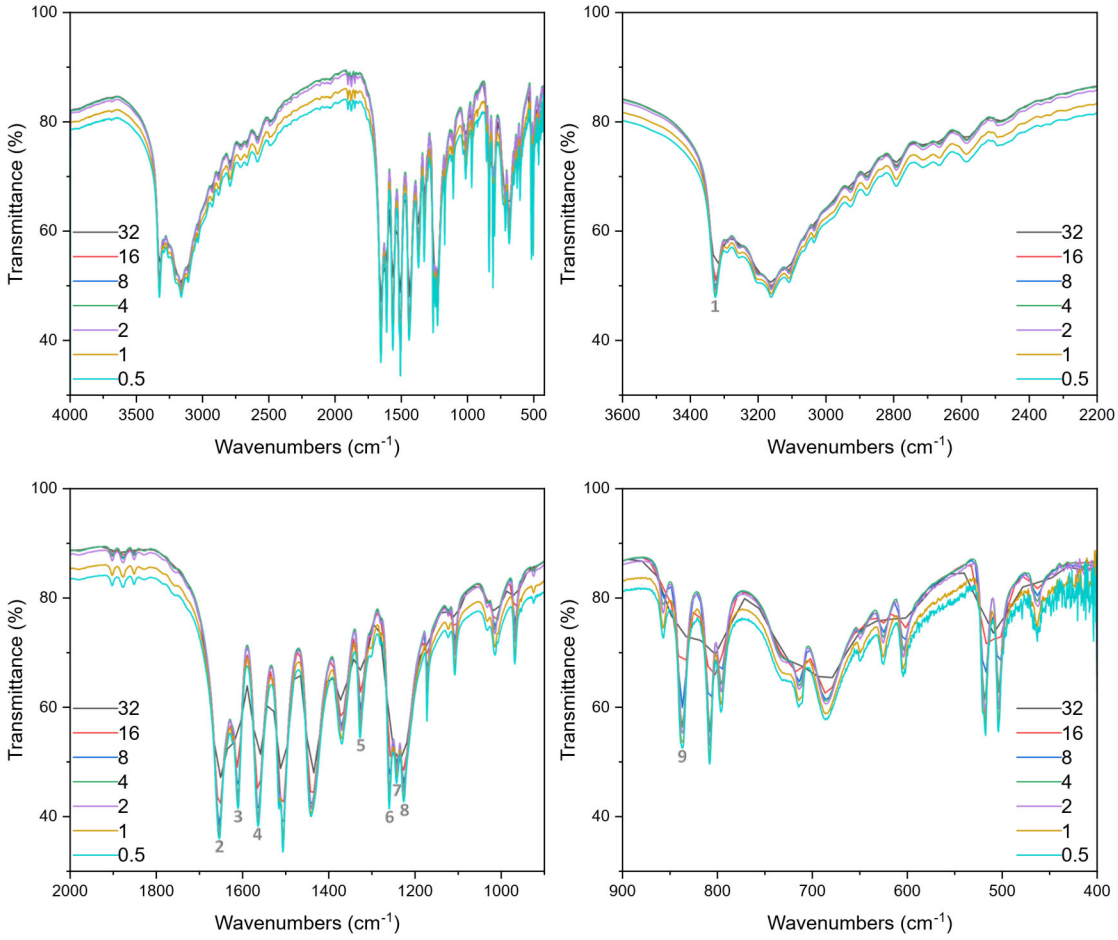


Figure 3.6 Transmission FT-IR spectra of APAP collected on a Nicolet iS50 with varied spectral resolutions from 32 – 0.5 cm^{-1}. Numbering denotes peaks in analysis.

Table 3-4 Peak positions (cm^{-1}) [ǂ] for APAP collected on a Nicolet iS50 FT-IR at variable spectral resolutions. [ǂ]Wavenumbers were determined in OMNIC using the standard peak picking function. [ǂ]NR denotes peak that were unresolved at said resolution.

	32 cm^{-1}	**16 cm^{-1}**	**8 cm^{-1}**	**4 cm^{-1}**	**2 cm^{-1}**	**1 cm^{-1}**	**0.5 cm^{-1}**
Peak 1	3319.64	3324.40	3325.36	3325.67	3325.74	3325.87	3325.92
Peak 2	NR [ǂ]	1653.54	1654.16	1654.03	1653.90	1653.91	1654.30
Peak 3	NR	1612.56	1610.94	1610.56	1610.41	1610.41	1610.47
Peak 4	1560.74	1563.15	1563.52	1563.72	1563.79	1563.86	1563.98
Peak 5	1328.43	1325.25	1326.14	1326.93	1327.32	1327.46	1327.53
Peak 6	NR	NR	1258.25	1259.32	1259.63	1259.76	1259.85
Peak 7	NR	NR	1241.98	1242.36	1242.71	1242.86	1242.85
Peak 8	NR	NR	1225.98	1226.02	1226.00	1226.05	1226.25
Peak 9	NR	836.36	836.90	837.07	836.95	836.67	836.73

Table 3-5 Peak position (cm^{-1}) as a function of resolution for APAP as assessed by calculating the difference in assigned peak value from the value determined at 0.5 cm^{-1} (e.g. Δ32 cm-1 = $peak_{0.5cm-1} - peak_{32cm-1}$). [ǂ]NR denotes peak that were unresolved at said resolution.

	Δ32 cm^{-1}	**Δ16 cm^{-1}**	**Δ8 cm^{-1}**	**Δ4 cm^{-1}**	**Δ2 cm^{-1}**	**Δ1 cm^{-1}**	**0.5 cm^{-1}**
Peak 1	6.28	1.52	0.56	0.25	0.18	0.05	3325.92 cm^{-1}
Peak 2	NR[ǂ]	0.76	0.14	0.27	0.40	0.39	1654.30 cm^{-1}
Peak 3	NR	-2.09	-0.47	-0.09	0.06	0.06	1610.47 cm^{-1}
Peak 4	3.24	0.83	0.46	0.26	0.19	0.12	1563.98 cm^{-1}
Peak 5	-0.90	2.28	1.39	0.60	0.21	0.07	1327.53 cm^{-1}
Peak 6	NR	NR	1.60	0.53	0.22	0.09	1259.85 cm^{-1}
Peak 7	NR	NR	0.87	0.49	0.14	-0.01	1242.85 cm^{-1}
Peak 8	NR	NR	0.27	0.23	0.25	0.20	1226.25 cm^{-1}
Peak 9	NR	0.37	-0.17	-0.34	-0.22	0.06	836.73 cm^{-1}
Average |Δ|	**3.47**	**1.31**	**0.66**	**0.34**	**0.21**	**0.12**	**-**

Spectra for PS and APAP were also collected on Bruker, PerkinElmer, and Shimadzu systems (see Appendix B for data and calculations) to assess instrument-to-instrument variation in peak positions (Δ) as a function of resolution. As illustrated above with NIST traceable accuracy, there are different uncertainties for PS (and APAP) peaks collected on the other systems compared to the Nicolet. For example, PS peak positions at a spectral resolution of 16 cm^{-1} exhibit a Δ of less than 2.7 cm^{-1} for the Nicolet, while on Bruker, PerkinElmer, and Shimadzu systems the corresponding value are 4.7, 3.3, and 4.7 cm^{-1}, respectively. At 4 cm^{-1} spectral resolution, the peak position is within 0.4 cm^{-1} for the Nicolet, but 0.4, 0.7, or 1.1 cm^{-1} for the other systems (Bruker, PerkinElmer, and Shimadzu, respectively). For APAP at 16 cm^{-1} spectral resolution, peak positions were within either 2.3, 3.9, 2.4 or 2.0 cm^{-1} (Nicolet, Bruker, PerkinElmer, and Shimadzu, respectively) of the highest resolution value. At 4 cm^{-1}, this peak position variation was within 0.5 – 1.2 cm^{-1}, depending on the system. The ability for a system to deal with water vapor was found to be important when determining peak positions. For APAP collected on the Shimadzu system, water vapor bands prominently interfered above 8 cm^{-1} resolution. This is evident by the introduction of extremely sharp bands overlapping with APAP signals (Figure 3.7). Careful adjustments of the peak sensitivity threshold can deconvolute some APAP and water signals at higher resolution. Despite water interference, peak positions can be known within 2.2 cm^{-1}.

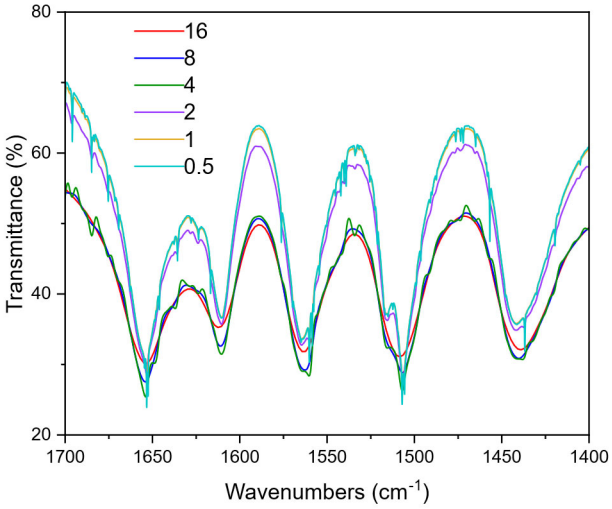


Figure 3.7 Region of intense water vapor interference with APAP bands. Data was collected on a Shimadzu IRTracer-100 FT-IR.

The fact that the Δ values vary somewhat by instrument cannot be ascribed to the sample, because the same samples were measured on each instrument. Furthermore, the use of the same software for peak picking and analysis suggests that the variation arises from the instrument. Although a general Michelson interferometer design is the basis for all FT-IR spectrometers, each company has incorporated subtle differences to deal with issues in the movable mirror and alignment, generally centered around accounting for tilt, shear, and temperature changes. For example, Shimadzu employs a traditional Michelson flat mirror design[46], whereas Nicolet incorporates an additional digital signal processing control onto their flat mirror[47]; both still rely on dynamic alignment. However, PerkinElmer and Bruker models have eliminated the dynamic alignment necessity through engineering designs. PerkinElmer utilizes a pivoting mirror pair claimed to be immune to tilt and shear[48], while Bruker is fit with dual retroreflective cube corner mirrors that are claimed to eliminate tilt and shear, as well as vibrational and thermal effects.[49] Experimentally, these subtle differences in interferometer design are likely responsible for variation in peak positions. It is also important to note that there was not a noticeable trend in

decreased accuracy with any one brand, nor was a trend based on peak intensity discerned (assuming saturation is avoided, vide infra). Analysis of each system with native software, that is presumably better designed to account for instrument-specific variations, did not drastically improve peak position accuracy either (see Appendix B). Overall, a general recommendation accounting for most sources of variation (resolution, instrument, etc.) is that the position of a peak can be known within 1.1 cm^{-1} for well resolved bands at a spectral resolution of 4 cm^{-1} or higher, and within 2.2 cm^{-1} at 8 cm^{-1} resolution. For spectral resolutions where bands are poorly (or not at all) resolved, the uncertainty can be as high as 4.7 or 10.4 cm^{-1} (for 16 and 32 cm^{-1} resolutions, respectively). However, these uncertainties are still much lower than expectation for wavenumber accuracy based on data spacing.[11,25]

Wavenumber accuracy can also be influenced by peak shapes as a result of high absorbance, giving rise to less accurate peak positions as a result of loss in Lorentzian character; this often generates sidelobes (see Table 3-1) or plateaued peaks. As absorbance scales with increased spectral resolution, this can give rise to a resolution-dependent shift. This concept is important to note especially considering that PS standards typically used for verifying instrument performance are often highly absorbing, yielding five near-to-completely saturated bands (Figure 3.8). This might be expected to lead to a situation where ATR FT-IR spectroscopy leads to less peak position variation for peaks that would otherwise saturate in transmission. However, experimentally this is not borne out.

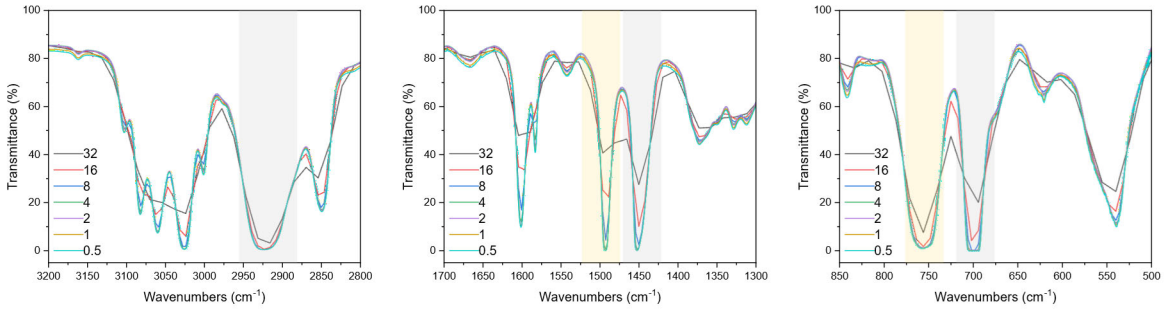


Figure 3.8 Spectral resolution effect (32 – 0.5 cm^{-1}) on resolving saturated PS peaks (highlighted with boxes). Transmission FT-IR spectra were collected on the Nicolet iS50.

Five low transmittance PS peaks (Figure 3.9) were analyzed for wavenumber accuracy (Δ) based on ATR or transmission collection modes on the Nicolet system (Tables 3-6 and 3-7, peaks 10-14). At a spectral resolution of 16 cm^{-1}, Δ is within 2.6 cm^{-1} using ATR and 3.6 cm^{-1} using transmission collection. With a spectral resolution of 4 cm^{-1}, however, ATR does not offer improved accuracy; peak positions are within 1.9 and 1.7 cm^{-1} for ATR and transmission, respectively. While 0.5 cm^{-1} spectral resolution was advantageous for wavenumber accuracy in transmission, its utility in ATR wavenumber accuracy is reduced. The spectrometer signal becomes increasingly noisy, introducing choppy features that complicate peak picking and introduce more uncertainty in peak position. Scrutiny of peak shape and its resultant effect on peak picking is needed in some cases. At increased spectral resolutions above 8 cm^{-1}, PS peak 13 is an excellent reminder for continued monitoring of peak shape, as the ATR band appears to be two poorly resolved bands at high resolution (Figure 3.10) and likely contribute error in its position (accounting for this, the wavenumber accuracy improves to within 0.5 cm^{-1} for 4 cm^{-1} resolution). Additional caution should be heeded when determining the positions of saturated bands with multiple data points near zero, introducing features that the peak picking function can mistake for the true peak position. This is evident in PS peak 14, where spectral resolution of 1 or 0.5 cm^{-1} has introduced a misleading shift as a result of poor peak picking of the true center

(Figure 3.10). Peak position accuracy for ATR data is also still subject to instrument variation (Tables B-26 and B-27, Figure B.7).

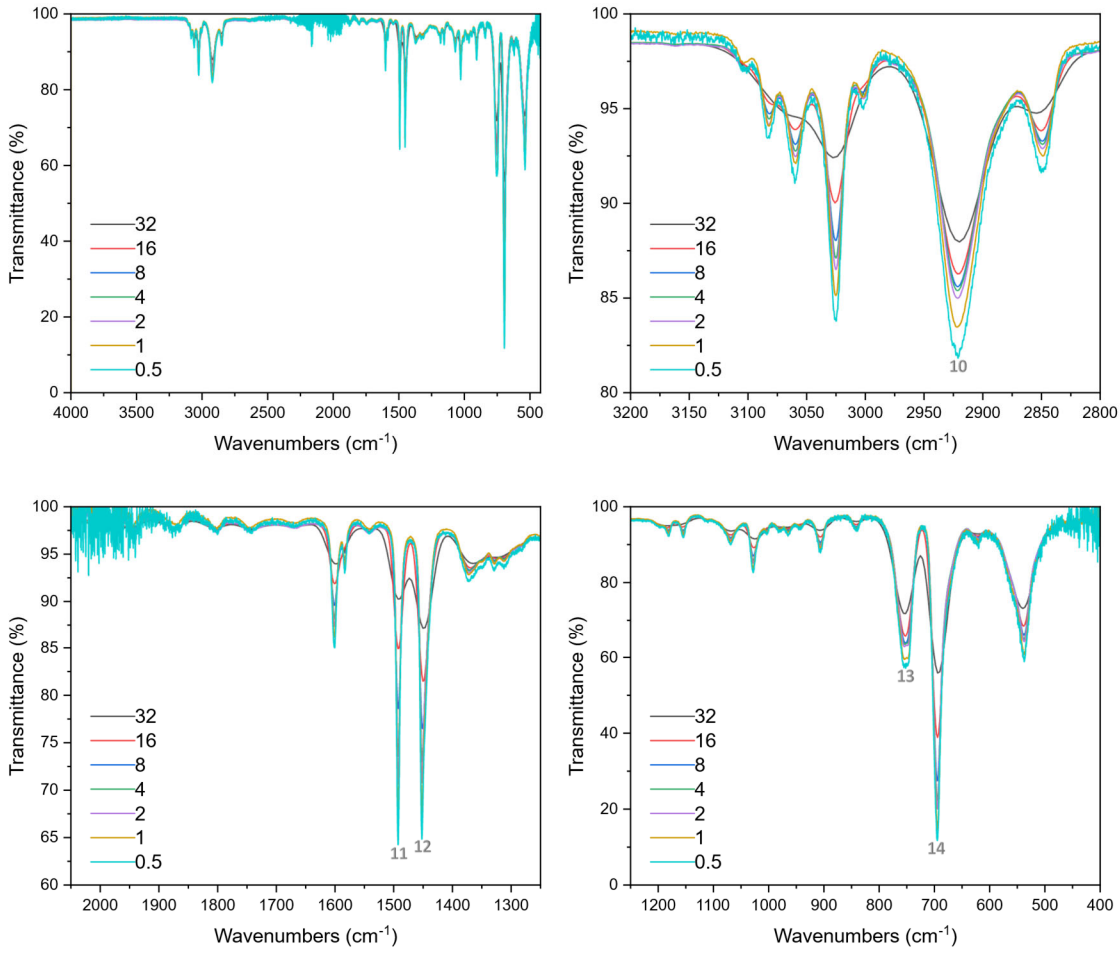


Figure 3.9 ATR FT-IR spectra of PS collected on a Nicolet iS50 with varied spectral resolutions from 32 – 0.5 cm^{-1}. Numbering denotes peaks in analysis.

Table 3-6 Peak positions (cm^{-1}) [I] of PS bands collected on a Nicolet iS50 FT-IR at variable spectral resolutions. [I]Wavenumbers were determined in OMNIC using the standard peak picking function. *Peak pick value varies noticeably from the center of the peak.

	32 cm^{-1}	**16 cm^{-1}**	**8 cm^{-1}**	**4 cm^{-1}**	**2 cm^{-1}**	**1 cm^{-1}**	**0.5 cm^{-1}**
ATR							
Peak 10	2920.16	2920.82	2921.25	2921.47	2921.25	2922.10	2921.01*
Peak 11	1491.14	1491.88	1492.20	1492.35	1492.38	1492.43	1492.47
Peak 12	1448.60	1449.37	1450.69	1451.51	1451.75	1451.85	1451.98
Peak 13	753.74	752.57	752.05	753.76*	754.19*	754.60*	751.85
Peak 14	692.74	694.45	694.77	694.58	694.49	694.39	694.76
Transmission							
Peak 10	2921.04	2922.48	2923.75	2924.18	2924.19	2924.22	2924.76
Peak 11	1490.98	1491.93	1492.5	1492.87	1492.97	1492.99	1492.92
Peak 12	1450.03	1449.00	1450.32	1451.82	1452.38	1452.49	1452.57
Peak 13	756.83	756.27	756.16	756.76	757.06	758.03	757.74
Peak 14	697.68	699.37	699.81	699.54	698.92	694.31*	701.21*

Table 3-7 Peak position (cm^{-1})[I] as a function of resolution for PS bands collected on a Nicolet iS50 FT-IR, as assessed by calculating the difference in assigned peak value from the value determined at 0.5 cm^{-1} (e.g. Δ32 cm^{-1} = $peak_{0.5cm-1} - peak_{32cm-1}$).

	Δ32 cm^{-1}	**Δ16 cm^{-1}**	**Δ8 cm^{-1}**	**Δ4 cm^{-1}**	**Δ2 cm^{-1}**	**Δ1 cm^{-1}**	**Δ0.5 cm^{-1}**
ATR							
Peak 10	0.85	0.19	-0.24	-0.46	-0.24	-1.09	0*
Peak 11	1.33	0.59	0.27	0.12	0.09	0.04	0
Peak 12	3.38	2.61	1.29	0.47	0.23	0.13	0
Peak 13	-1.89	-0.72	-0.20	-1.91*	-2.34*	-2.75*	0
Peak 14	2.02	0.31	-0.01	0.18	0.27	0.37	0
Average |Δ|	**1.89**	**0.88**	**0.40**	**0.63**	**0.63**	**0.88**	**-**
Transmission							
Peak 10	3.72	2.28	1.01	0.58	0.57	0.54	0
Peak 11	1.94	0.99	0.42	0.05	-0.05	-0.07	0
Peak 12	2.54	3.57	2.25	0.75	0.19	0.08	0
Peak 13	0.91	1.47	1.58	0.98	0.68	-0.29	0
Peak 14	3.53	1.84	1.40	1.67	2.29	6.90*	0*
Average |Δ|	**2.53**	**2.03**	**1.332**	**0.81**	**0.76**	**1.58**	**-**

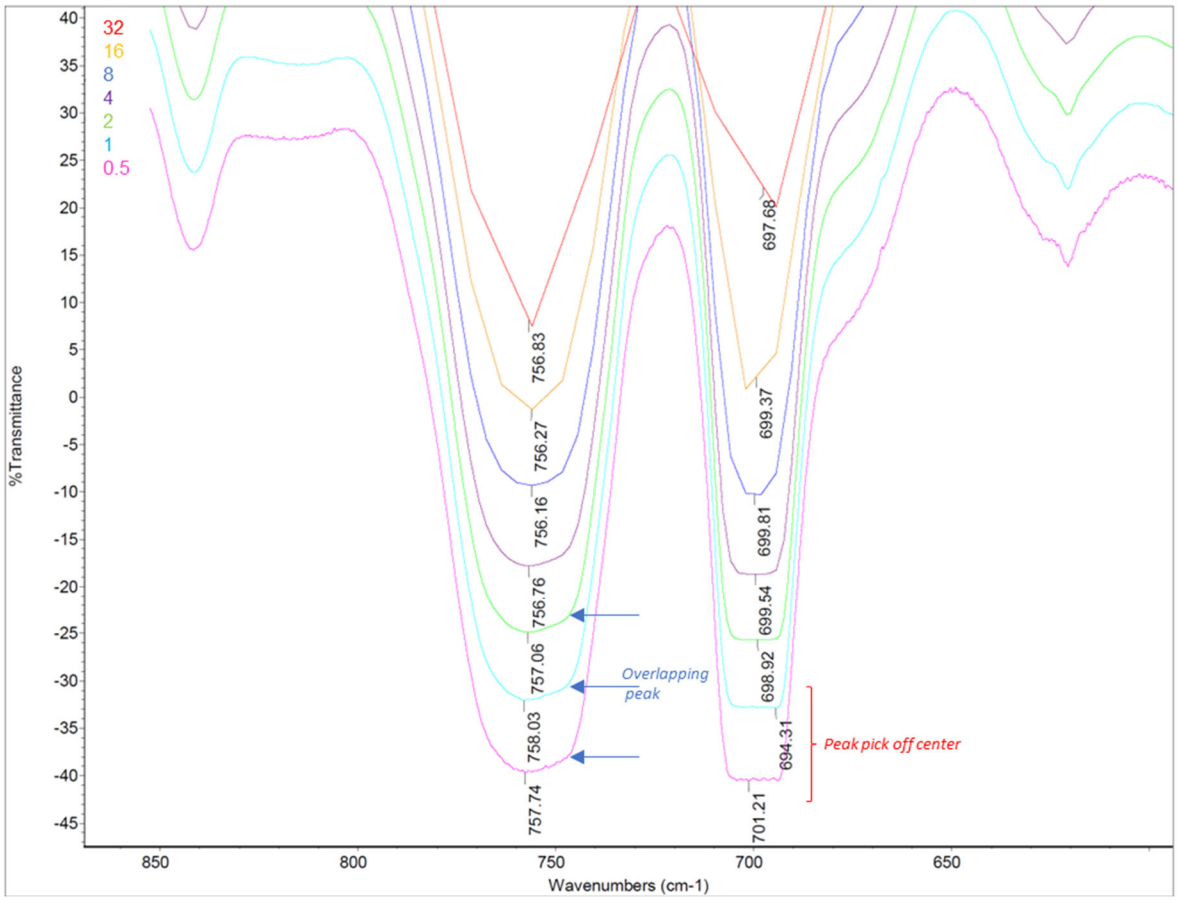


Figure 3.10 Increased spectral resolution can lead to deceptive shifts in peak positions for saturated bands using the standard peak picking function. This is evident by deviation between the picked values and the apparent center of PS peak 14 near ~ 700 cm^{-1}. Additionally, scrutiny of peak shape can also be needed at increased spectral resolution to discern when an apparent band is likely two overlapping peaks, as evident with Peak 13 near ~755 cm^{-1}. Transmission FT-IR plot shown in OMNIC.

3.4 Conclusion

An experimental study was conducted on FT-IR peak position variation as a function of spectral resolution, and the effect of instrument-to-instrument variation was also examined. For well resolved peaks that are not saturated, instrument variation results in a wavenumber accuracy within 1.1 cm^{-1} for spectral resolutions of 4 cm^{-1} or higher and within 2.2 cm^{-1} for spectral resolutions of 8 cm^{-1}. For low resolution data collections (16 or 32 cm^{-1}), wavenumber accuracy is reduced to 4.7 or 10.4 cm^{-1}, respectively. In addition to instrumental effects on wavenumber accuracy, other factors that may influence peak positions are peak intensity (or saturation), water vapor interference, and excessive noise (Table B-30) in the spectrum (Figure 3.11). To balance

accuracy and efficiency, it is recommended that data is collected at a spectral resolution of 4 cm^{-1} and compared to data within the same instrument dataset. With this general guidance, a more judicious and informative interpretation of FT-IR peak positions can be achieved to improve the elucidation of chemical structure and polymorphism, which are important topics found in scientific, industrial, and legal contexts.

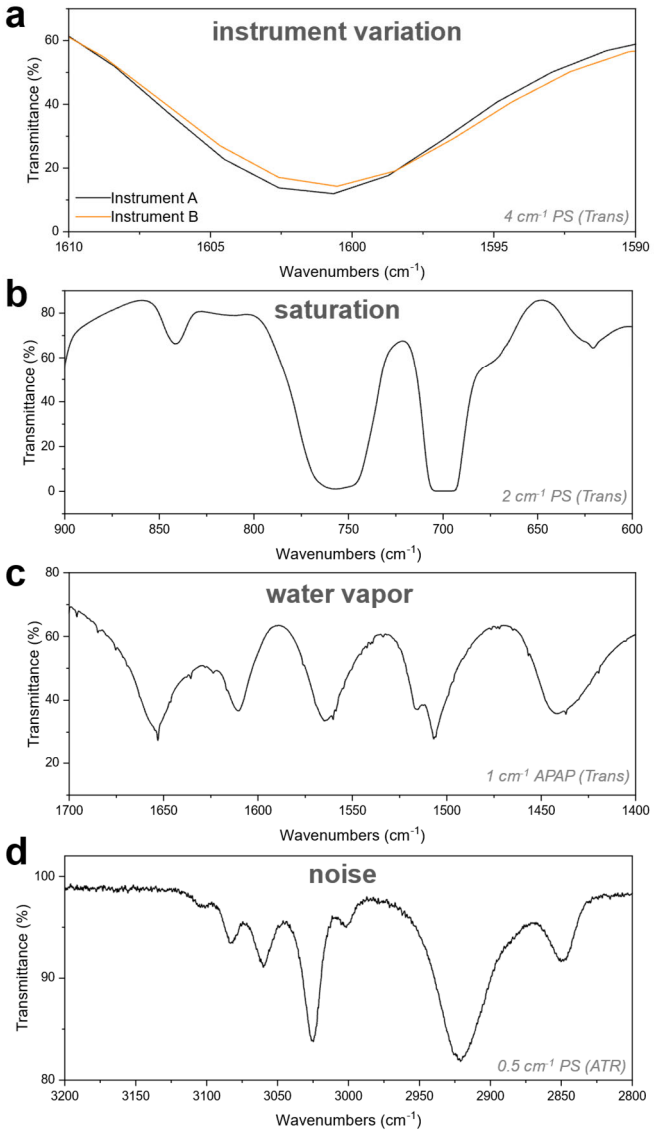


Figure 3.11 In addition to resolution, peak position variation can be influenced by (a) instrument design, (b) absorbance saturation, (c) water vapor interference, and (d) spectral noise.

3.5 Experimental Details

3.5.1 Sample preparation

A NIST-traceable PS film (1.5 mil thickness) from Nicolet was used for both transmission and attenuated total reflection (ATR) FT-IR. APAP (Form I) was purchased from ICN Biomedicals. A 0.4% APAP in KBr sample for transmission FT-IR was prepared by grinding in an agate mortar and pestle. A pellet was pressed in a 13 mm die at 10,000 lbs. See Appendix B for additional details.

3.5.2 FT-IR

Transmission spectra were collected using four different FT-IR spectrophotometers: a Thermo Scientific Nicolet iS50 equipped with a KBr beam splitter, DTGS detector, and Vectra™ interferometer; a Bruker Alpha II equipped with a KBr beam splitter, DLaTGS detector, and RockSolid™ cube corner interferometer; a PerkinElmer Frontier equipped with a KBr beam splitter, DTGS detector, and DynaScan™ interferometer; and a Shimadzu IRTracer-100 equipped with a KBr beam splitter, DLaTGS detector, and Michelson interferometer. The Nicolet iS50 and Bruker Alpha II employed N2 purge during collection. Spectra obtained from 32 scans were collected from 4000 to 400 cm^{-1} at varied spectral resolutions of 32, 16, 8, 4, 2, 1, and 0.5 cm^{-1} unless limited by the instrument (Bruker 32 – 2 cm^{-1}, Shimadzu 16 – 0.5 cm^{-1}). Data collected on all instruments were analyzed in OMNIC to standardize a peak picking function, as well as in their respective native software (Bruker OPUS, PerkinElmer Spectrum, Shimadzu Lab Solutions) for comparison. Default peak picking parameters were used.

For ATR FT-IR, spectra were collected using the same parameters established above on the Thermo Scientific Nicolet iS50 with an integrated diamond ATR module, as well as on the Bruker Alpha II using a diamond/ZnSe UATR attachment. Data collected on both instruments

were analyzed in OMNIC without ATR correction using standard peak picking parameters. Bruker data were also analyzed similarly in OPUS.

3.6 Acknowledgements

This work was supported by the ONR (Grant no. N00014-22-1-2101). S. T. Nicolau acknowledges the Science, Mathematics, and Research for Transformation (SMART) program for their support.

3.7 References

(1) Smith, B. C. *Infrared Spectral Interpretation: A Systematic Approach*; CRC Press: Boca Raton, 1998. https://doi.org/10.1201/9780203750841.
(2) Aldrich, D. S.; Smith, M. A. Pharmaceutical Applications of Infrared Microspectroscopy. *Appl. Spectrosc. Rev.* **1999**, *34* (4), 275–327. https://doi.org/10.1081/ASR-100101218.
(3) *AIST:Spectral Database for Organic Compounds*, SDBS. https://sdbs.db.aist.go.jp/sdbs/cgi-bin/cre_index.cgi (accessed 2024 -01 -11).
(4) *NIST Chemistry WebBook.* https://webbook.nist.gov/chemistry/ (accessed 2024 -02 -21).
(5) *IR Spectrum Table.* https://www.sigmaaldrich.com/US/en/technical-documents/technical-article/analytical-chemistry/photometry-and-reflectometry/ir-spectrum-table (accessed 2024 -01 -11).
(6) Silverstein, R. M.; Webster, F. X.; Kiemle, D. *Spectrometric Identification of Organic Compounds*, 7th Edition; Wiley, 2005.
(7) Larkin, P. J. Chapter 6 - IR and Raman Spectra–Structure Correlations: Characteristic Group Frequencies. In *Infrared and Ra-man Spectroscopy (Second Edition)*; Larkin, P. J., Ed.; Elsevier, 2018; pp 85–134. https://doi.org/10.1016/B978-0-12-804162-8.00006-9.
(8) Lin-Vien, D.; Colthup, N. B.; Fateley, W. G.; Grasselli, J. G. *The Handbook of Infrared and Raman Characteristic Frequencies of Organic Molecules*; Elsevier, 1991.
(9) Michelson, A. A.; Morley, E. W. On the Relative Motion of the Earth and the Luminiferous Ether. *Am. J. Sci.* **1887**, *s3-34* (203), 333–345. https://doi.org/10.2475/ajs.s3-34.203.333.
(10) Griffiths, P. R. Fourier Transform Infrared Spectrometry: Theory and Instrumentation. In *Transform Techniques in Chemistry*; Griffiths, P. R., Ed.; Modern Analytical Chemistry; Springer US: Boston, MA, 1978; pp 109–139. https://doi.org/10.1007/978-1-4684-2403-4_5.
(11) Tasumi, M. *Introduction to Experimental Infrared Spectroscopy: Fundamentals and Practical Methods*; John Wiley & Sons, Incorporated: Newark, UNITED STATES, 2014.
(12) Griffiths, P. R.; de Haseth, J. A. *Fourier Transform Infrared Spectroscopy*, 2nd ed.; John Wiley & Sons, Inc.: Hoboken, New Jersey, 2007.
(13) Morrill, L. A.; Kammeyer, J. K.; Garg, N. K. Spectroscopy 101: A Practical Introduction to Spectroscopy and Analysis for Undergraduate Organic Chemistry Laboratories. *J. Chem. Educ.* **2017**, *94* (10), 1584–1586. https://doi.org/10.1021/acs.jchemed.7b00263.

(14) Liotta, L. J.; James-Pederson, M. Identification of an Unknown Compound by Combined Use of IR, 1H NMR, 13C NMR, and Mass Spectrometry: A Real-Life Experience in Structure Determination. *J. Chem. Educ.* **2008**, *85* (6), 832. https://doi.org/10.1021/ed085p832.
(15) Dumancas, G. G.; Carreto, N.; Generalao, O.; Ke, G.; Bello, G.; Lubguban, A.; Malaluan, R. Chemometrics for Quantitative Determination of Terpenes Using Attenuated Total Reflectance–Fourier Transform Infrared Spectroscopy: A Pedagogical Laboratory Exercise for Undergraduate Instrumental Analysis Students. *J. Chem. Educ.* **2023**, *100* (8), 3050–3060. https://doi.org/10.1021/acs.jchemed.3c00358.
(16) Huffman, S. W.; Salido, A. L.; Evanoff, D. D. Quantitative Infrared Spectroscopy in the Undergraduate Laboratory Via Multivariate Mixture Analysis of a Simulated Analgesic. *Spectrosc. Lett.* **2010**, *43* (7–8), 539–544. https://doi.org/10.1080/00387010.2010.510702.
(17) Schuttlefield, J. D.; Grassian, V. H. ATR–FTIR Spectroscopy in the Undergraduate Chemistry Laboratory. Part I: Fundamentals and Examples. *J. Chem. Educ.* **2008**, *85* (2), 279. https://doi.org/10.1021/ed085p279.
(18) Schurter, E. J.; Zook-Gerdau, L. A.; Szalay, P. Analysis of a Suspected Drug Sample. *J. Chem. Educ.* **2011**, *88* (10), 1416–1418. https://doi.org/10.1021/ed101001u.
(19) Byrd, H.; Donnell, S. E. O. A General Chemistry Laboratory Theme: Spectroscopic Analysis of Aspirin. *J. Chem. Educ.* **2003**, *80* (2), 174. https://doi.org/10.1021/ed080p174.
(20) Roggo, Y.; Chalus, P.; Maurer, L.; Lema-Martinez, C.; Edmond, A.; Jent, N. A Review of near Infrared Spectroscopy and Chemo-metrics in Pharmaceutical Technologies. *J. Pharm. Biomed. Anal.* **2007**, *44* (3), 683–700. https://doi.org/10.1016/j.jpba.2007.03.023.
(21) Févotte, G. New Perspectives for the On-Line Monitoring of Pharmaceutical Crystallization Processes Using in Situ Infrared Spectroscopy. *Int. J. Pharm.* **2002**, *241* (2), 263–278. https://doi.org/10.1016/S0378-5173(02)00237-5.
(22) Reich, G. Near-Infrared Spectroscopy and Imaging: Basic Principles and Pharmaceutical Applications. *Adv. Drug Deliv. Rev.* **2005**, *57* (8), 1109–1143. https://doi.org/10.1016/j.addr.2005.01.020.
(23) Song, Y.; Cong, Y.; Wang, B.; Zhang, N. Applications of Fourier Transform Infrared Spectroscopy to Pharmaceutical Preparations. *Expert Opin. Drug Deliv.* **2020**, *17* (4), 551–571. https://doi.org/10.1080/17425247.2020.1737671.
(24) Jamrógiewicz, M. Application of the Near-Infrared Spectroscopy in the Pharmaceutical Technology. J. *Pharm. Biomed. Anal.* **2012**, *66*, 1–10. https://doi.org/10.1016/j.jpba.2012.03.009.
(25) Smith, B. C. *Fundamentals of Fourier Transform Infrared Spectroscopy*, 2nd ed.; CRC Press: Boca Raton, 2011. https://doi.org/10.1201/b10777.
(26) Bell, R. J. CHAPTER TWO - Historical Sketch and Crucial Ideas. In *Introductory Fourier Transform Spectroscopy*; Bell, R. J., Ed.; Academic Press, 1972; pp 16–32. https://doi.org/10.1016/B978-0-12-085150-8.50007-3.
(27) Herres, W.; Gronholz, J. *Understanding FT-IR Data Processing* https://www.ccmr.cornell.edu/wp-content/uploads/sites/2/2015/11/Understanding_FTIR.pdf (accessed 2024 -01 -10).
(28) *USP <851> Spectroscopy and Light Scattering.* https://www.drugfuture.com/Pharmacopoeia/usp35/PDF/0409-

0415%20%5B851%5D%20SPECTROPHOTOMETRY%20AND%20LIGHT-SCATTERING.pdf (accessed 2024-02-22).
(29) *Monographs and General Chapters Affected by Revision to General Chapter Spectrophotometry and Light-Scattering | USP-NF* https://www.uspnf.com/notices/spectrophotometry-light-scattering (accessed 2024 -01 -15).
(30) *USP <854> Mid-Infrared Spectroscopy*. https://online.uspnf.com/uspnf/document/1_GUID-21493947-8F57-4FC7-9338-FD47C1354A3A_4_en-US (accessed 2024-02-22).
(31) Williams, R. L. Official USP Reference Standards: Metrology Concepts, Overview, and Scientific Issues and Opportunities. J. *Pharm. Biomed. Anal.* **2006**, *40* (1), 3–15. https://doi.org/10.1016/j.jpba.2005.07.017.
(32) *In Re Sebela Patent Litigation*; 2017.
(33) *Eisai Co., Ltd. v. Glenmark Pharmaceuticals, Ltd.*; 2015.
(34) Van Eerdenbrugh, B.; Taylor, L. S. Application of Mid-IR Spectroscopy for the Characterization of Pharmaceutical Systems. *Int. J. Pharm.* **2011**, *417* (1), 3–16. https://doi.org/10.1016/j.ijpharm.2010.12.011.
(35) Romañuk, C. B.; Garro Linck, Y.; Chattah, A. K.; Monti, G. A.; Cuffini, S. L.; Garland, M. T.; Baggio, R.; Manzo, R. H.; Olivera, M. E. Crystallographic, Thermal and Spectroscopic Characterization of a Ciprofloxacin Saccharinate Polymorph. *Int. J. Pharm.* **2010**, *391* (1), 197–202. https://doi.org/10.1016/j.ijpharm.2010.03.007.
(36) Norris, T.; Aldridge, P. K.; Sekulic, S. S. Determination of End-Points for Polymorph Conversions of Crystalline Organic Com-pounds Using On-Line Near-Infrared Spectroscopy. *Analyst* **1997**, *122* (6), 549–552. https://doi.org/10.1039/A700782E.
(37) Griesser, U. J.; Auer, M. E.; Burger, A. Micro-Thermal Analysis, FTIR- and Raman-Microscopy of (R,S)-Proxyphylline Crystal Forms. *Microchem. J.* **2000**, *65* (3), 283–292. https://doi.org/10.1016/S0026-265X(00)00124-7.
(38) Harris, R. K.; Yeung, R. R.; Lamont, R. B.; Lancaster, R. W.; Lynn, S. M.; Staniforth, S. E. 'Polymorphism' in a Novel Anti-Viral Agent: Lamivudine. *J. Chem. Soc. Perkin Trans. 2* **1997**, No. 12, 2653–2660. https://doi.org/10.1039/A704709F.
(39) Zhang, G.-C.; Lin, H.-L.; Lin, S.-Y. Thermal Analysis and FTIR Spectral Curve-Fitting Investigation of Formation Mechanism and Stability of Indomethacin-Saccharin Cocrystals via Solid-State Grinding Process. *J. Pharm. Biomed. Anal.* **2012**, *66*, 162–169. https://doi.org/10.1016/j.jpba.2012.03.039.
(40) Aakeröy, C. B.; Wijethunga, T. K.; Desper, J.; Moore, C. Halogen-Bond Preferences in Co-Crystal Synthesis. *J. Chem. Crystallogr.* **2015**, *45* (6), 267–276. https://doi.org/10.1007/s10870-015-0596-9.
(41) Aakeröy, C.B.; Welideniya, D.; Desper, J.; Moore, C. Halogen-Bond Driven Co-Crystallization of Potential Anti-Cancer Com-pounds: A Structural Study. *CrystEngComm* **2014**, *16* (44), 10203–10209. https://doi.org/10.1039/C4CE01614A.
(42) Al-Zoubi, N.; Koundourellis, J. E.; Malamataris, S. FT-IR and Raman Spectroscopic Methods for Identification and Quantitation of Orthorhombic and Monoclinic Paracetamol in Powder Mixes. *J. Pharm. Biomed. Anal.* **2002**, *29* (3), 459–467. https://doi.org/10.1016/S0731-7085(02)00098-5.
(43) Zapata, F.; López-Fernández, A.; Ortega-Ojeda, F.; Quintanilla, G.; García-Ruiz, C.; Montalvo, G. Introducing ATR-FTIR Spectroscopy through Analysis of Acetaminophen

Drugs: Practical Lessons for Interdisciplinary and Progressive Learning for Undergraduate Students. *J. Chem. Educ.* **2021**, *98* (8), 2675–2686. https://doi.org/10.1021/acs.jchemed.0c01231.
(44) Pasquarella, K.; Jardine, K.; Hill, K.; Jones, E.; Elia, R.; Gibbs, G.; Sonntag, M.; Tribe, L. Synthesis and Characterization of Acetaminophen: An Experimental and Theoretical Laboratory for the Undergraduate Curriculum. *J. Chem. Educ.* **2022**, *99* (2), 910–916. https://doi.org/10.1021/acs.jchemed.0c01512.
(45) *USP <1225> Validation of Compendial Procedures.* https://doi.usp.org/USPNF/USPNF_M99945_04_01.html (accessed 2024-02-22).
(46) *IRTracer-100 FTIR Spectrophotometer - Specs* https://www.ssi.shimadzu.com/products/ftir/ftir-spectroscopy/irtracer-100/spec.html (accessed 2024 -01 -29).
(47) Thermo Fisher Scientific. *Advanced FT-IR Spectrosocpy: Principles, Experiments and Applications Based on Research-Grade Nicole FT-IR Spectrometers* https://nicoletcz.cz/app/uploads/2021/07/59ba0832.pdf (accessed 2024 -01 -29).
(48) *PerkinElmer, Inc. What is the Dynascan interferometer, and how is it different from other designs?* https://www.youtube.com/watch?reload=9&app=desktop&v=KhYaBTVb_5g (accessed 2024 -01 -29).
(49) *The Bruker ROCKSOLID Interferometer* http://bc.orgchm.bas.bg/~irlab/Site_BG/Laboratory/rocksolid.pdf (accessed 2024 -01 -29).

Chapter 4 Controlling Energetic Crystal Morphology Using Tailored Polymeric Additives

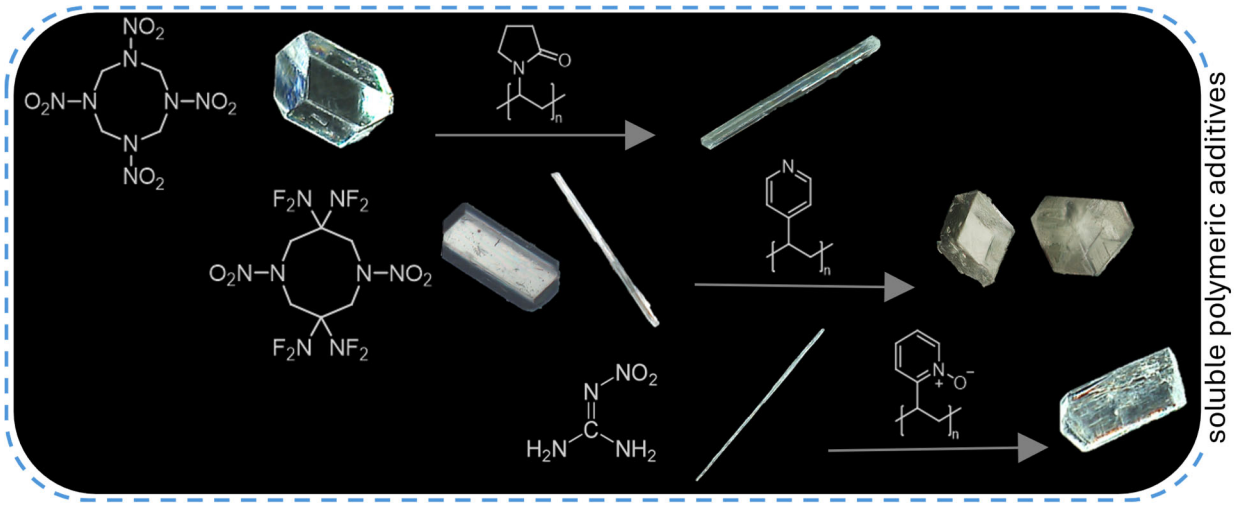


Figure 4.1 Polymeric additives were designed to interact face selectively to control the shape of several energetic crystals.

4.1 Publication of Chapter

Nicolau, S. T.; Matzger, A. J. Controlling Energetic Crystal Morphology Using Tailored Polymeric Additives. *Cryst. Growth Des.* **2025**, *25* (5), 1667–1674. https://doi.org/10.1021/acs.cgd.5c00049.

4.2 Introduction

When selecting a molecule to employ for a given application, chemical structure is the primary consideration in compound selection; properties as diverse as drug efficacy[1] and energetic performance[2–4] are typically directly related to molecular representations that emphasize covalent atomic connectivity. However, chemical structure alone does not dictate properties. How the molecule assembles into a solid with varying arrangements (crystal polymorphism) and/or degrees of crystallinity is also influential. Though often more subtle, the

crystal shape (morphology), affects several general properties including processability,[5,6] flowability,[7–9] and packing density[10,11] that are relevant across fields. Additionally, in energetic materials, morphology can influence explosive sensitivity,[12–15] making it a critical feature to study and control. The terms crystal morphology and shape are often used interchangeably because they both describe the visual appearance of the crystal. However, morphology deals more specifically with the discussion of crystallographic planes whereas shape deals with relative length to width descriptions based on the crystal habit or external appearance.[16]

The morphology of a crystal is not a property readily connected to the chemical identity of a compound. Instead, it is determined for a given polymorph by the relative growth rates of the faces exposed on the crystal surface and is defined by the slowest growing faces.[16] Altering crystal morphology is typically achieved by altering crystallization conditions and commonly employs changes in solvent,[17–19] temperature,[20] and supersaturation[21] with the principle that growth rates are modified by solvation. Less commonly employed, is the use of additives to control morphology that when added intentionally selectively adsorb onto crystal faces to impart morphology control.[22,23] While small-molecule additives have been shown to successfully alter morphology in several pharmaceuticals[16,24–28] and a few energetics[14,29], this design strategy is not without drawbacks. Consideration must be given on how to remove the additive post-crystallization, potentially requiring additional separation and purification steps.[16] Moreover, the concern for impurity incorporation[30] or molecular doping[31] and cocrystallization[32] is ever present if chemical similarity was a design criteria of the additive. With these concerns in mind, tethered additives in polymeric form become more attractive because incorporation risk is minimized. Additionally, polymeric additives can be more effective morphology modifiers than small

molecules because of their high concentration of functional groups that can interact with the intended surface.

Polymeric additives have been utilized in pharmaceuticals[33–36] for morphology control and have also been applied to energetic materials.[29,37–42] Nitroguanidine (NQ), one of those most diversely applied energetics (triple-base gun propellants, rocket propellants, and insensitive munitions[43,44]), crystallizes predominantly in a needle morphology but has seen improved flowability properties with the use of several polymeric additives.[29,39] Additionally, empirical studies of polymeric additives with NQ and 1,3,5,7-tetranitro-1,3,5,7-tetrazocane (HMX, a high performance energetic) have yielded morphology changes towards spherulitic, polycrystalline aggregates.[37,38] While these studies demonstrate successful control over morphology, it is often at the expense of single-crystal character, with most morphology changes accompanied by highly aggregated growth. Moreover, there is still a need to develop a deeper understanding of the additive interactions at play for crystallization control to identify a method for additive selection tailored to specific crystal shapes.

Herein, we report a polymeric additive design strategy for morphology control of energetic crystals based on the dominant interactions observed in cocrystals of these and related compounds. For three explosives (HMX, HNFX, and NQ; Figure 4.2a), we illustrate with several additives (poly(vinylpyrrolidone) (PVP), poly(4-vinylpyridine) (P4VP), and poly(2-vinylpyridine N-oxide) (P2VPNO); Figure 4.2b), that a tailored functionality tethered on a polymeric backbone can interact face selectively to control the overall shape without detectable incorporation into the crystal lattice. This work demonstrates morphology control in a fixed solvent and contributes additional examples of preferential interactions for energetics lacking traditional synthons.

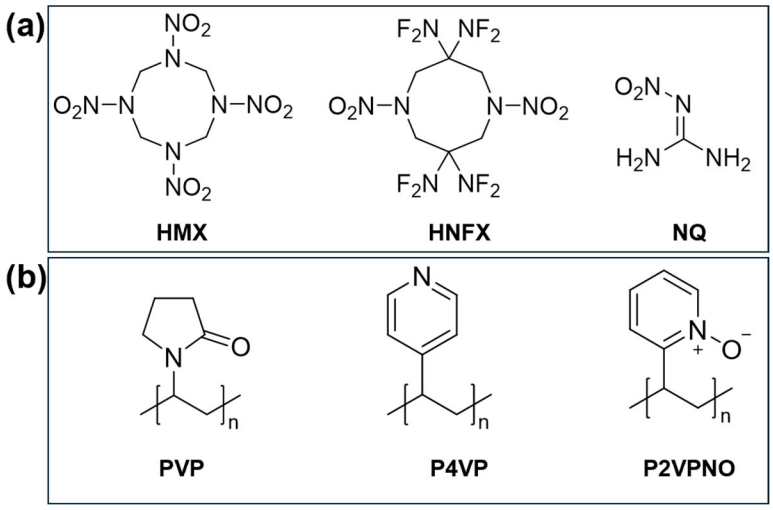


Figure 4.2 Chemical structures of selected (a) explosives and (b) additives.

4.3 Results and Discussion

HMX is a workhorse energetic, often utilized in the military because of its balance between modest explosive sensitivity and high performance. Although HMX crystallizes in four polymorphs, β-HMX is the most favorable and industrially relevant due to its stability and high energy density. β-HMX was selected as the model for this polymeric additive design strategy for three reasons outside of its application relevancy. First, the Bravais Friedel Donnay Harker (BFDH) morphology prediction reveals a blocky crystal morphology of this monoclinic polymorph (Figure 4.3) giving substantial opportunity to alter the morphology of HMX because of the large number of faces that are symmetry unique and expressed with large areas. Additionally, HMX can act as both an acceptor and donor in supramolecular interactions with other molecules, providing a rich basis set to choose interactions for morphology control. Lastly, its structural backbone models that of several other energetics for potentially transferable design control, particularly in the case of the gem-difluoronitramine substituted analog HNFX, which has been plagued by its poorly processable and sensitive morphology.[45,46]

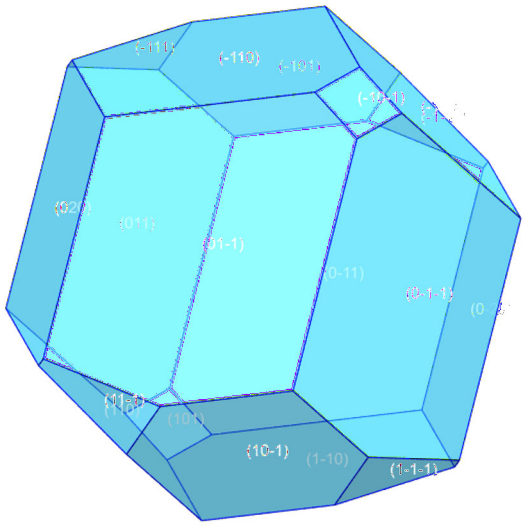


Figure 4.3 BFDH morphology of β-HMX. Computed with Mercury software 2024.1.0 (Build 401958) using cif from reference code OCHTET24.

Chemical functionality of the polymeric additives were selected based on cocrystal interactions reported in the Cambridge Structural Database (CSD) to have short contacts, giving preference to those mimicking commercially available polymers. Currently, 14 cocrystals (defined as multicomponent molecular crystals containing compounds that are solid at room temperature, assembled in stochiometric ratios) exist for HMX in the CSD and these mostly contain nitrogen heterocycles, often with adjacent carbonyl moieties, and aromatic rings with N-oxide or amine functionality (Figure C.1). To favor interactions with the additive, a crystallizing solvent absent of these functionalities was employed, eliminating many of the classical carbonyl-based solvents[47] used to combat the poor solubility of HMX. The system was also designed to utilize the polymer fully solubilized in the crystallizing solvent as opposed to insoluble polymer techniques such as polymer-induced heteronucleation[48,49], which limit interactions to one face. PVP was selected based on the HMX:1,3-dimethylimidazolidin-2-one cocrystal (1:1, reference code IDENEM)[50] and the HMX:pyrrolidine-2-one cocrystal (1:1, ZEZGUI)[51], with the shortest interactions occurring between energetic ring hydrogens (CH_2) and the coformer carbonyl

(C=O), and the energetic nitro group (NO_2) and carbonyl-adjacent CH_2 of the coformer, respectively (Figure C.2). We hypothesized this would be the dominant interaction present between HMX and PVP-modulated crystals.

β-HMX recrystallized from hot acetonitrile via cooling crystallization yields a blocky morphology similar to the predictions from BFDH theory, establishing the preferred morphology under this condition with no additive. With the addition of PVP, the crystal morphology elongated to yield prismatic-shaped crystals (Figure 4.4a). The orientation of crystal growth was determined using single crystal X-ray diffraction (SCXRD). The β polymorph of HMX was retained with the addition of PVP but an elongation along the a-axis (Figure 4.4b) was observed. Thus, PVP interacts to inhibit growth along the *b*- and *c*-axes. Additional BFDH calculations and packing views of dominant faces with contributions from only the *b*- and *c*-axes (for example, the (011), (0-11), (01-1), and (0-1-1) faces) provide likely interaction information for PVP based on the proximity of certain functional groups to each crystal face. This is illustrated in Figure 4.4c, where a packing slice of the (011) face is shown with the atoms closest to the face highlighted in space-filling representation. As hypothesized, the likely interactions occurring between PVP and HMX are the polymer carbonyl with the energetic ring hydrogens, as well as the polymer hydrogens with the energetic nitro-groups, based on the short contact model. It was confirmed using ^{1}H NMR spectroscopy that the polymer is not detectably incorporating into the crystal, consistent with control being exerted due to a reversible, preferential surface adsorption mechanism (see Figure 4.5 for representative NMR experiment). The influence of polymer molecular weight on morphology control was examined for HMX-PVP; substituting 360,000 MW polymer with much shorter PVP (10,000 MW) demonstrated qualitatively the same control in the block-to-needle direction.

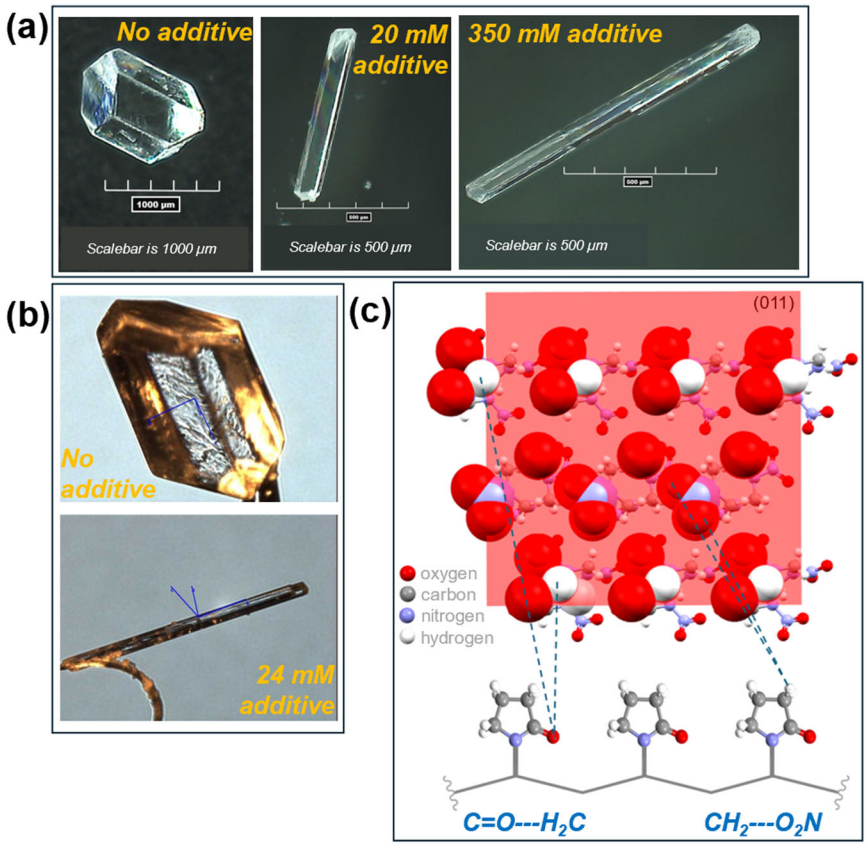


Figure 4.4(a) Morphology control of HMX with the additive poly(vinylpyrrolidone) (PVP) in acetonitrile. (b) Single crystal indexing of HMX morphologies. (c) Proposed PVP-crystal face interactions, demonstrated with (011) slice.

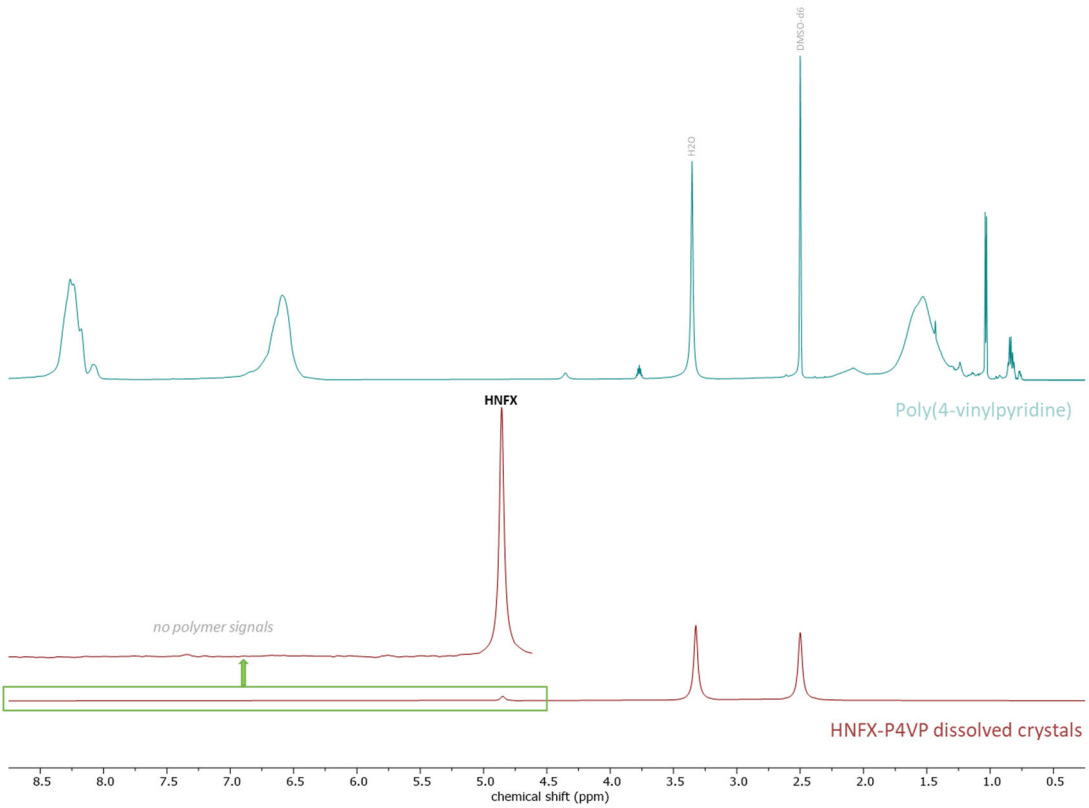


Figure 4.5 Proton NMR indicates that no polymer (P4VP) is detected within the crystal lattice of the morphology-modified energetic (HNFX) crystals upon dissolution of the highest additive concentration tested.

Morphology control by PVP was also tested on HNFX, the analogous gem-difluoronitramine substituted version of HMX, using a similar workflow as above. No stoichiometric cocrystal information currently exists to aid in the selection of additives to exert control on the energetic; identifying potential synthons, particularly interacting with the difluoronitramine functionality, fills an important gap for fluorine-based energetics. HNFX recrystallized from hot ethanol via cooling crystallization yields a short prismatic morphology (Figure 4.6a). The presence of PVP promoted elongation of the prism along the *c*-axis (Figure 4.6b), with increased radial growth as the additive concentration increased to yield a bowtie-like morphology (Figure 4.6a). Again, no incorporation of the polymer was detected. The functionality being tethered to a polymer induced the same changes at a concentration 2 orders of magnitude lower than its monomeric counterpart (Figure 4.7). Based on the structural similarity

and closest atoms prevalent on relevant crystal faces (i.e., (2-10)), we hypothesize similar interactions occur between HNFX-PVP as in HMX-PVP (Figure 4.6c; HNFX has disordered NF_2 groups but the average is shown). However, there is still a large proportion of the crystal faces dominated by fluorine that are likely unaccounted for.

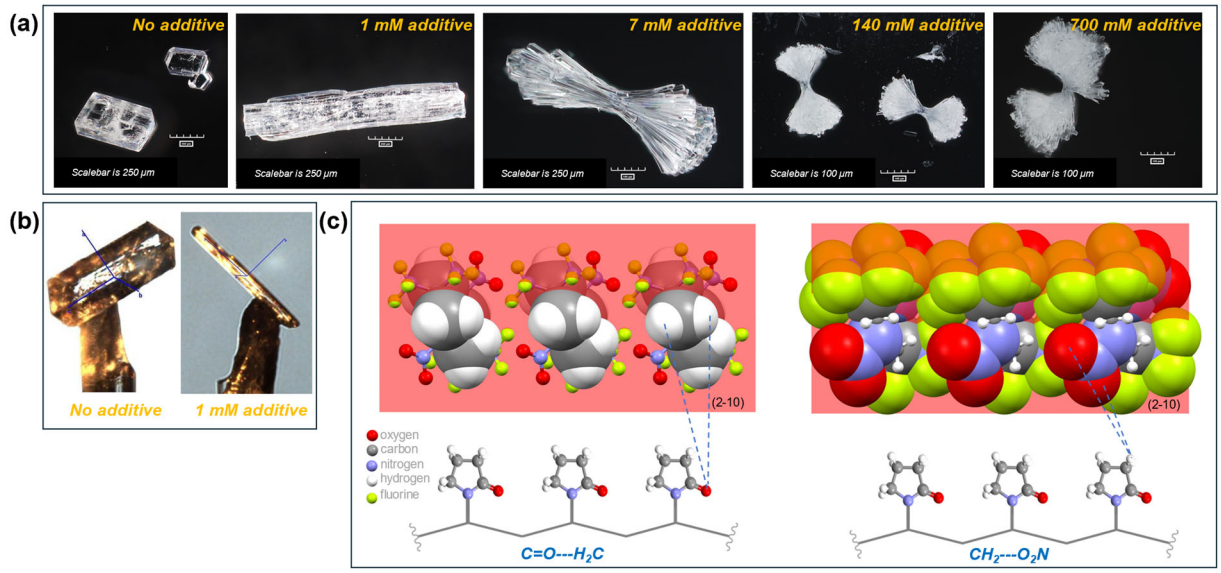


Figure 4.6 (a) Morphology control of HNFX with the additive poly(vinylpyrrolidone) (PVP) in ethanol. (b) Single crystal indexing of HNFX morphologies. (c) Proposed PVP-crystal face interactions, demonstrated with (2-10) slice.

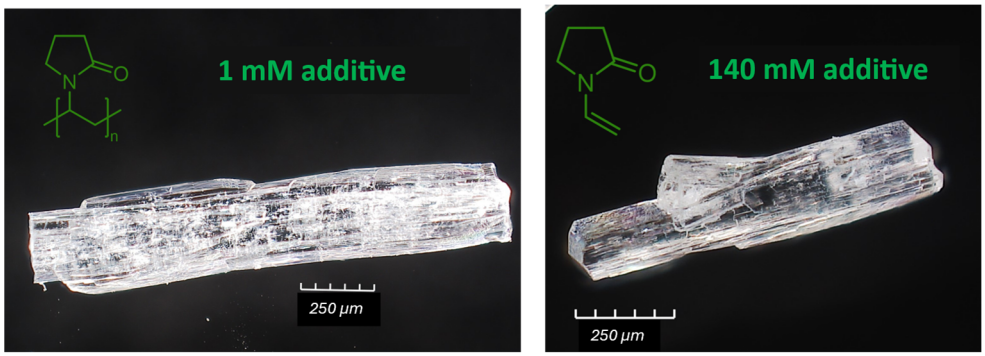


Figure 4.7 Tethering the pyrrolidone moiety to a polymeric backbone imparts similar morphology changes at lower concentrations compared to the monomeric form.

Fluorine is not typically considered a good halogen bond donor due to its small sigma hole (positive electrostatic region), although a few examples of sigma-hole mediated interactions are known for bonded fluorine,[52–56] particularly if the substituent is sufficiently electron

withdrawing. These weak and more negative/neutral fluorine interactions have been termed "fluorine bonds", analogous with hydrogen bonding rather than traditional "halogen bonding".[57] The "bis difluoro-placement" on HNFX does generate a substantially more positive charge than one would expect in organofluorine species (Figure 4.8), improving the likelihood of non-traditional fluorine-bonding. Against this background, poly(4-vinyl pyridine) or P4VP was selected with potential to engage in such interactions, with the additional consideration for the prevalence of nitrogen heterocycles in successful coformers (even outside of HMX).[32,51,58,59]

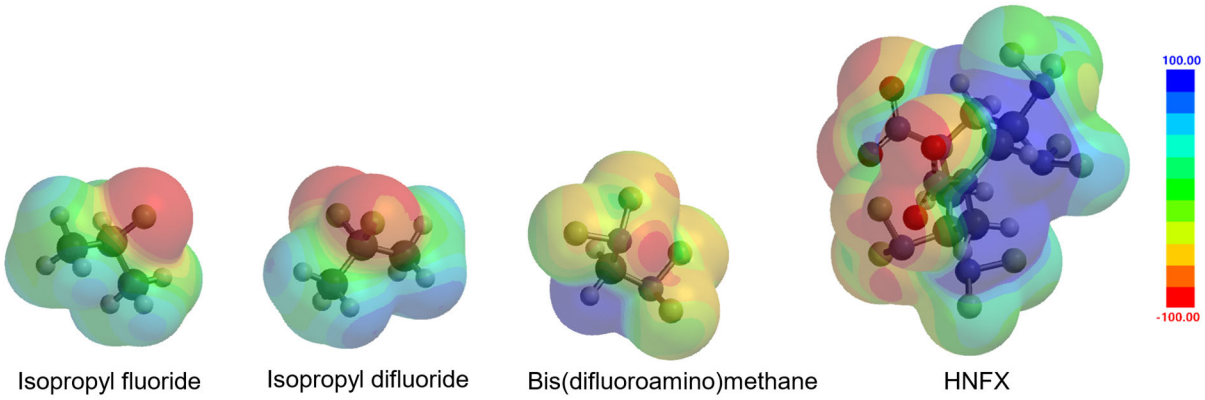


Figure 4.8 Electrostatic potential maps illustrating increased fluorine content in a structure provides more neutral charge character, improving halogen-bonding capability. Spartan '24 v1.2.0 was used to calculate the electrostatic potential map. Equilibrium geometries were optimized by Density Functional Theory (B3LYP) calculations with the 6-31G* basis set.

HNFX recrystallized from hot ethanol via cooling crystallization in the presence of P4VP yields crystals that are truncated along the c-axis, resulting in small cubic morphologies (Figures 4.9a, 4.9b). Often, these truncated crystals are highly intergrown, giving stacked appearances. We hypothesize that the preferential interaction of the polymer to the *c*-axis, is likely due to the accessibility of the difluoramines, extending further on the crystal faces and covering a larger relative proportion of the crystal face compared to competing interactions (Figure 4.10).

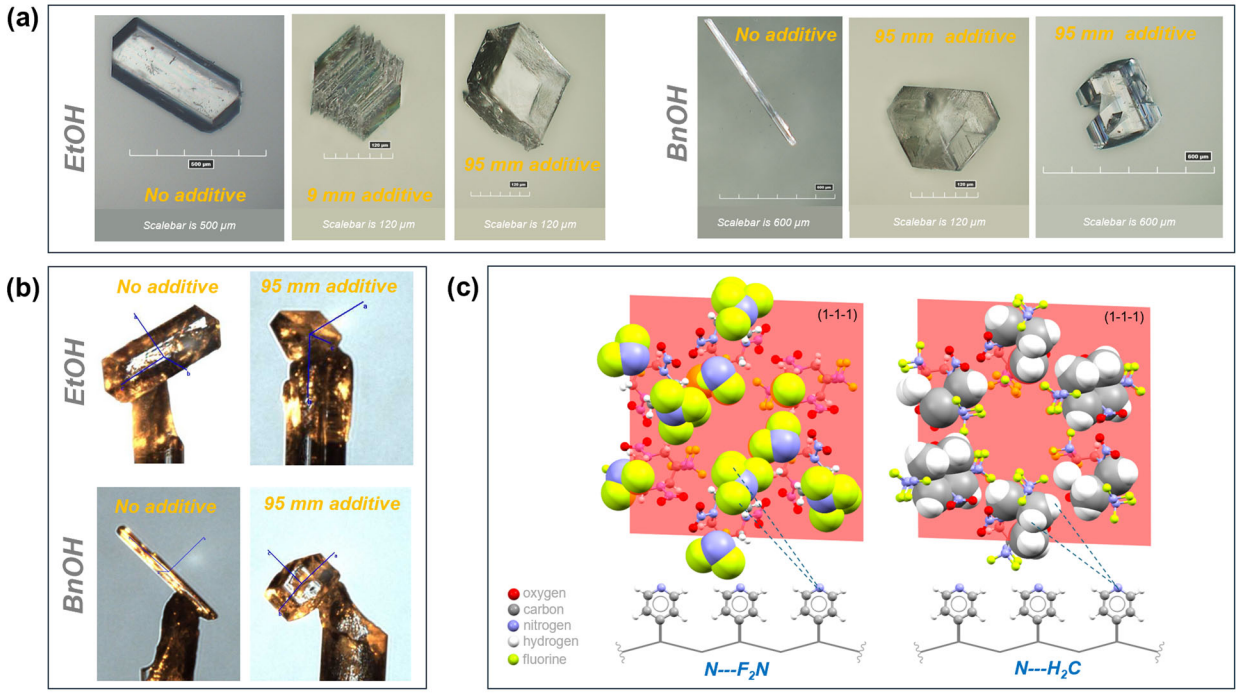


Figure 4.9 (a) Morphology control of HNFX with the additive poly(4-vinylpyridine) (P4VP) in either ethanol (EtOH) or benzyl alcohol (BnOH). (b) Single crystal indexing of HNFX morphologies. (c) Proposed P4VP-crystal face interactions, demonstrated with (1-1-1) slice.

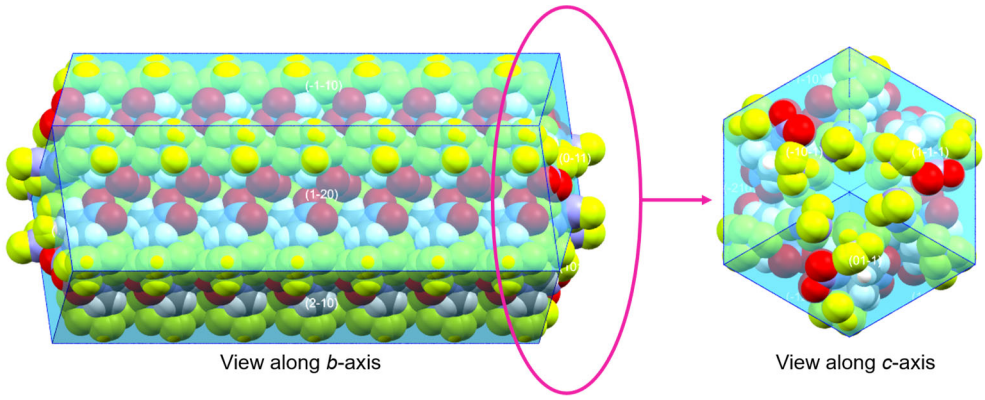


Figure 4.10 BFDH morphology prediction of HNFX (JURHOT) packed with space-filling molecules. We hypothesize that the preferential interaction of the polymer (P4VP) to the c-axis is likely due to the accessibility of the difluoramines, extending further on the crystal faces and covering a larger relative amount of the crystal face compared to competing interactions.

The interaction potential of P4VP and HNFX was further demonstrated in a second solvent system: benzyl alcohol. HNFX recrystallized from benzyl alcohol with no additive

yielded needle-shaped crystals. The addition of P4VP into the crystallizing solvent resulted in morphology truncated along the c-axis to yield a blocky morphology (Figure 4.9a, 4.9b). For both solvent systems, no polymer incorporation was detected. As a control, polystyrene (PS), an analog of P4VP lacking nitrogen functionality, in benzyl alcohol was tested. HNFX retained its needle morphology with PS (Figure 4.11), supporting the specific role that having a more negative region of electrostatic potential in the polymer plays in morphology control, whether it be through fluorine-bonding or frequently observed interactions involving energetic ring hydrogens (CH_2) with sp^2 hybridized nitrogen-based coformers (Figure 4.9c).

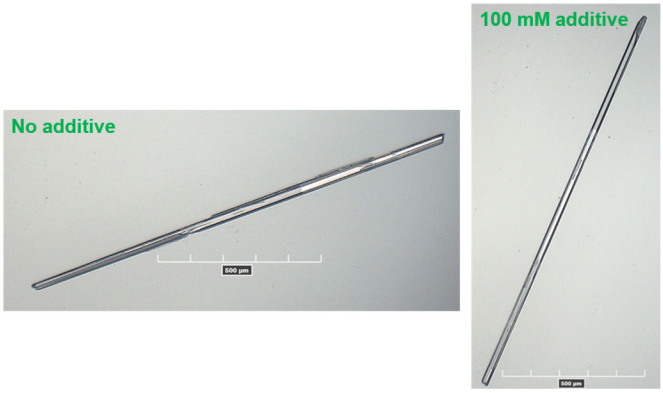


Figure 4.11 HNFX retained its needle morphology when recrystallized from benzyl alcohol with polystyrene additive.

Conversion from needle to block morphology is arguably one of the most important transitions to understand, with potential to rectify many processing issues around persistent needle morphologies causing filtration issues and equipment clogging[60]; in the field of energetic materials the avoidance of needles is even more urgent given that they tend to show increased impact sensitivity.[12] NQ is notable in this context, as it exhibits a needle morphology when crystallized from typical solvents. Here, suppression of NQ's needle morphology with polymeric additives is exerted. The use of a hydrogen bond acceptor is a distinction from previous successes[29] and demonstrates that the additive selection model can be extended to other explosives lacking cocrystal information, as proven successful here with HNFX. When

examining reoccurring coformer motifs in the HMX cocrystal literature, interactions based around an N-oxide (Figure C.3) were found in three of 14 structures (reference codes WEPTAP, ZEZGIW, ETOCOH)[51,61], exhibiting the shortest interactions between the N-oxide and energetic ring hydrogens (CH_2). This led to the selection of P2VPNO as an additive for NQ.

The most common solvent for NQ is water, which results in extremely long and thin needles in the absence of additives (Figure 4.12a). The presence of P2VPNO resulted in significant truncation of NQ crystals to yield blocky prisms. At 41 mM additive concentration, truncation always occurred, with slight morphology variation that was independent of concentration or agitation. Unlike the example of HNFX and PVP, where increased additive concentration resulted in continued growth modification, there is a point where so much polymer is added into the crystallizing system that crystal nucleation is hindered. Indexing showed that NQ crystal growth was being truncated along the *a*-axis (Figure 4.12b), meaning the additive must be interacting with faces perpendicular to that axis to modulate growth (i.e., (111)). The primary amine functionality of NQ and its ability to hydrogen bond with the N-oxide is likely the dominating interaction given the density of these functional groups on the representative plane (Figure 4.12c).

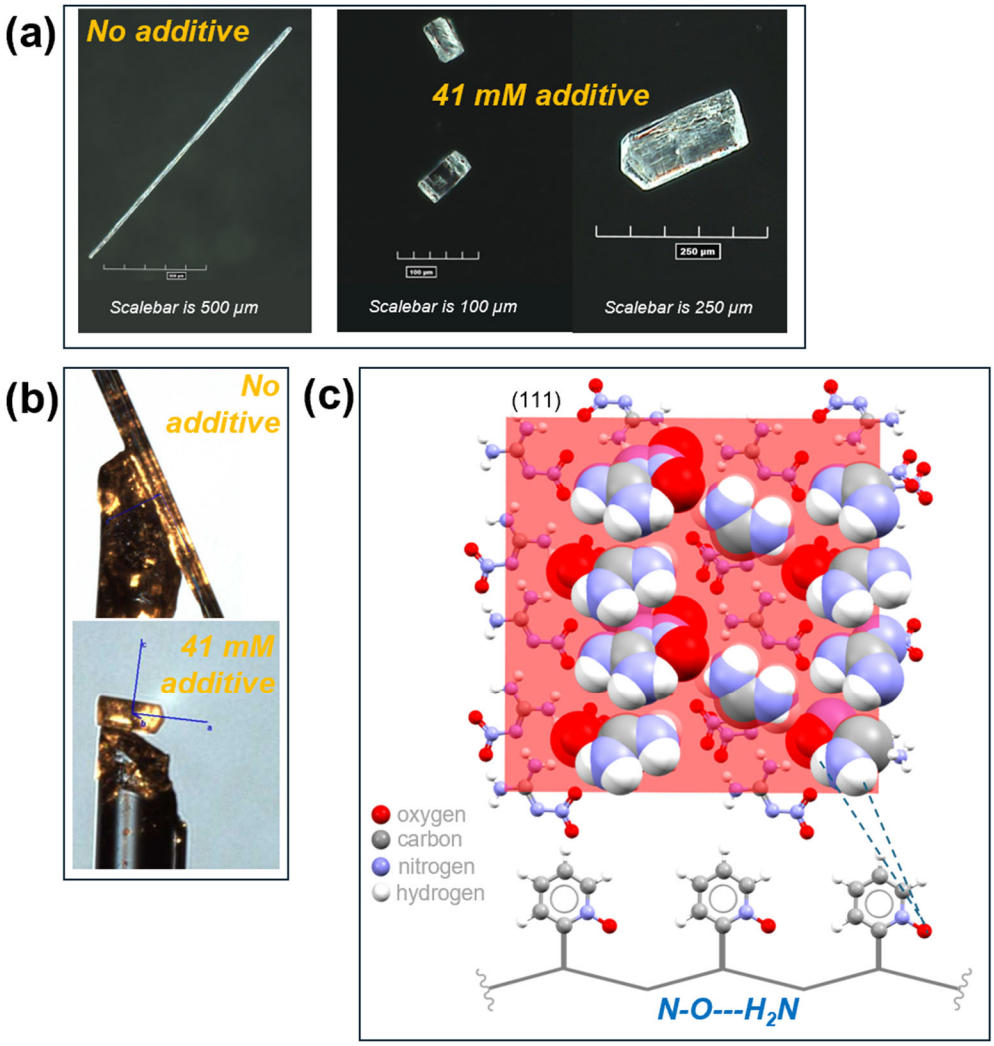


Figure 4.12 (a) Morphology control of NQ with the additive poly(2-vinylpyridine N-oxide) (P2VPNO) in water. (b) Single crystal indexing of NQ morphologies. (c) Proposed P2VPNO-crystal face interactions, demonstrated with (111) slice.

Although the solubility profile of P2VPNO is not compatible with the HMX crystallization condition used above, its utility for the structurally similar HNFX was explored. When benzyl alcohol was utilized as the crystallization solvent, the thin HNFX control needles were modified to much thicker needles (Figure 4.13). However, in ethanol solvent (Figure 4.14a) P2VPNO resulted in elongation of the short control prisms along the *c*-axis (Figure 4.14b) at very low polymer concentration. This means that the polymer interacts along the *a*- and *b*-axes to modulate crystal growth (Figure 4.14c). Based on the short contact cocrystal modeling, the

common motif is the N-oxide interacting with the energetic ring hydrogens (CH_2), as illustrated in the figure with the representative plane (110). However, as demonstrated above with the HNFX-P4VP system, fluorine-bonding is also a likely contributing factor, particularly when considering the N-oxide functionality has a similar electrostatic potential to that of pyridine (Figure 4.15).

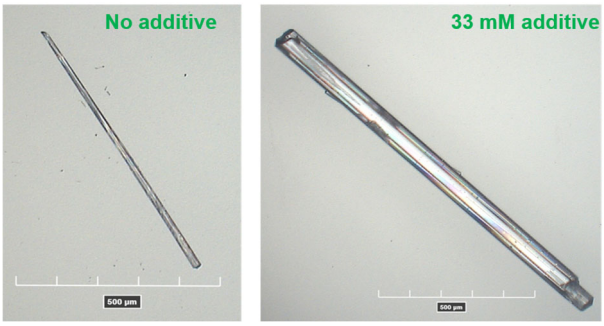


Figure 4.13 The thin HNFX control needle was modified to a much thicker needle, changing the aspect ratio when recrystallized from benzyl alcohol with P2VPNO.

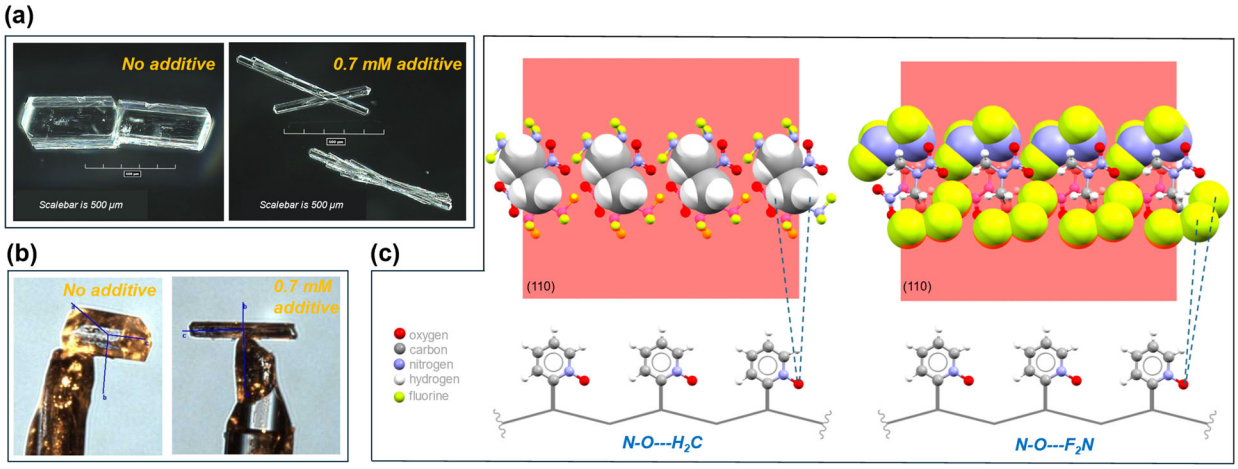


Figure 4.14 (a) Morphology control of HNFX with the additive poly(2-vinylpyridine N-oxide) (P2VPNO) in ethanol. (b) Single crystal indexing of HNFX morphologies. (c) Proposed P2VPNO-crystal face interactions, demonstrated with (110) slice, to emphasize low concentration change.

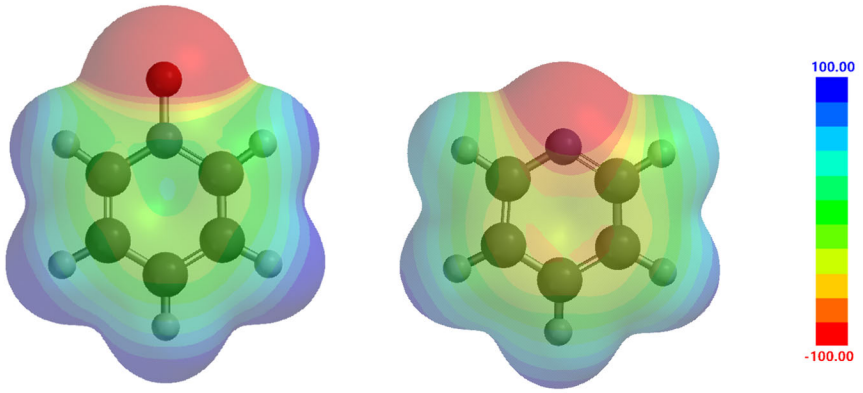


Figure 4.15 Electrostatic potential maps for the motifs of poly(2-vinylpyridine N-oxide) and poly(4-vinylpyridine) (demonstrated as pyridine N-oxide and pyridine, respectively) illustrate a similar propensity for halogen-bonding with fluorine based on the regions of very positive and very negative potentials. Spartan '24 v1.2.0 was used to calculate the electrostatic potential map. Equilibrium geometries were optimized by Density Functional Theory (B3LYP) calculations with the 6-31G* basis set.

4.4 Conclusion

Tailored polymeric additives were designed, informed by dominant interactions observed in cocrystals, to interact face selectively and control the crystal morphology of three energetic materials. This was achieved by utilizing cocrystal motifs found in the HMX cocrystal library, tethering them to a soluble polymer backbone, and applying them to HMX and the structurally similar energetic HNFX. Morphology modifications were made in both desirable (needle-to-block) and undesirable (block-to-needle) directions using H-bond acceptor polymers (e.g. PVP and P4VP). The approach was extended to a less structurally similar system, NQ, that is plagued with a poorly processable needle morphology; unaggregated, blocky crystals were obtained in the presence of the H-bond acceptor P2VPNO. Given the recurrence of certain functional groups within energetics (nitro, nitramine, amine, N-oxide), molecular interactions targeted for one structure may be transferable to others, as demonstrated herein with two energetics lacking interaction information. This design strategy for selecting polymeric additives has the potential to be employed outside of energetics, especially with the rich library of pharmaceutical

cocrystals to gain inspiration for other additives. Because pharmaceuticals have more traditional synthons that promote hydrogen bonding interactions (carboxylic acids, amides, alcohols), there may be greater morphology control based on the number of molecular interactions achievable within one compound. While the polymeric additive approach is the more effective morphology modifier due to the high concentration of functional groups that can interact with the intended surface, one challenge to overcome is the solubility of the additive and its solvent compatibility with the target material. Potential methods for combatting these issues are utilization of tailor-made polymeric additives (as opposed to commercially available) and mixed systems of crystallizing solvents that balance the solubility of both the additive and target material. Additionally, employing the polymeric additive as a swollen gel, in which crystals are grown within, may be a technique to balance solubility issues while still promoting multisite and multisurface interactions. For energetics specifically though, morphology control is useful to generate safer (insensitive) and more efficient munitions and manufacturing practices. Whereas changes in morphology are often coupled with a change in polymorph, being able to independently tune morphology while retaining polymorphic control provides critical tools for understanding the morphology-sensitivity relationship.

4.5 Experimental Details

4.5.1 Materials

Warning! Although no unplanned detonations occurred during this work, HMX, HNFX, and NQ are explosives and should be handled appropriately. Proper safety practices are implemented to eliminate detonation from friction, heat, electrostatic discharge, impact, and flame.

All polymers and solvents were used as received. Poly(vinylpyrrolidone) (PVP, Mw ~360K) was purchased from Scientific Polymer Products. Poly(4-vinylpyridine) (P4VP, Mw ~60K) was purchased from Sigma Aldrich. Poly(2-vinylpyridine N-oxide) (P2VPNO, molecular weight 300,000-400,000) was purchased from Polysciences. Acetonitrile (Optima, Fisher Chemical), ethanol (200 Proof, Decon Labs), benzyl alcohol (99%, Thermo), and water (HPLC grade, Fisher Chemical) were used as crystallization solvents.

4.5.2 Crystallizations

Energetics were recrystallized with and without the presence of polymeric additive utilizing cooling crystallization in either Macherey-Nagel N8 round, crimp neck vials (0.3 mL capacity) sealed with PTFE/silicone/PTFE crimp caps or Macherey-Nagel N10 flat, screw neck vial (1.5 mL capacity) with polypropylene/silicone/PTFE screw caps. Typically, crystallizations were set up on the 1 mg scale; energetics were massed into the vials and then either pure crystallizing solvent (control, no additive) or additive dissolved in the crystallizing solvent (polymer stock at variable concentrations) was added to achieve a specific concentration of energetic in solvent/stock. Crystallizations were placed in a drying oven in pre-heated sand baths and monitored periodically for full dissolution of the energetic. Once all samples were dissolved, vials were removed from the oven and allowed to cool slowly to room temperature in the hot sand bath. The following concentrations and temperatures were used for each energetic/solvent pairing: HMX/acetonitrile [1.0 mg / 40.0 μL] at 60 °C, HNFX/ethanol [1.0 mg/ 40.0 μL] at 80 °C, HNFX/benzyl alcohol [1.0 mg/ 25.0 μL] at 100 °C, and NQ/water [1.0 mg/ 200 μL] at 80 °C.

4.5.3 Optical Microscopy

Crystals were harvested and imaged using a Hirox MXB-2500REZ 3D digital microscope and the accompanying software suite (Hirox RH-2000 Ver 2.0.3.0). Typically,

images were acquired with High-Range or Mid-Range objectives, utilizing a 4.00 µm or 15.00 µm interval 3D multifocus stack, respectively.

4.5.4 Single Crystal Indexing

Crystals were mounted on a thin glass capillary or Nylon loop using cyanoacrylate gel adhesive, and single crystal X-ray diffraction data were collected using a Rigaku XtaLAB Synergy-S X-ray diffractometer with a kappa goniometer geometry configuration. The X-ray source is a PhotonJet-S microfocus Cu source (λ = 1.54184 Å) operated at 50 kV and 1 mA. X-ray intensities were measured with a HyPix-6000HE detector held 34 mm from the sample. The data were processed using CrysAlisPro v42.75a (Rigaku Oxford Diffraction) and matched to known Cambridge Structural Database (CSD) reference codes for identification. Directional axes were overlaid on the single crystal images to establish the orientation of crystal growth. Bravais Friedel Donnay Harker (BFDH) and packing/slicing calculations were completed in Mercury software 2024.1.0 (Build 401958). The following CSD reference codes were used to retrieve cif files for calculations with each explosive: OCHTET24 (HMX), JURHOT (HNFX), and NTRGUA03 (NQ). For NQ, the space group was transformed from Fdd2 to F2dd match current lattice notation.

4.5.5 ^{1}H NMR Spectroscopy

Polymer incorporation into energetic crystals was monitored by dissolving a few crystals from the highest additive concentration condition in deuterated DMSO or water and analyzing with a Varian Vnmrs 600 MHz spectrometer.

4.6 Acknowledgements

This work was supported by the ONR (Grant no. N00014-22-1-2101). S. T. Nicolau acknowledges the Science, Mathematics, and Research for Transformation (SMART) program for their support.

4.7 References

(1) Galandrin, S.; Oligny-Longpré, G.; Bouvier, M. The Evasive Nature of Drug Efficacy: Implications for Drug Discovery. *Trends Pharmacol. Sci.* **2007**, *28* (8), 423–430. https://doi.org/10.1016/j.tips.2007.06.005.

(2) Zeman, S.; Jungová, M. Sensitivity and Performance of Energetic Materials. *Propellants Explos. Pyrotech.* **2016**, *41* (3), 426–451. https://doi.org/10.1002/prep.201500351.

(3) Mathieu, D. Sensitivity of Energetic Materials: Theoretical Relationships to Detonation Performance and Molecular Structure. *Ind. Eng. Chem. Res.* **2017**, *56* (29), 8191–8201. https://doi.org/10.1021/acs.iecr.7b02021.

(4) Zhou, J.; Zhang, J.; Wang, B.; Qiu, L.; Xu, R.; Sheremetev, A. B. Recent Synthetic Efforts towards High Energy Density Materials: How to Design High-Performance Energetic Structures? *FirePhysChem* **2022**, *2* (2), 83–139. https://doi.org/10.1016/j.fpc.2021.09.005.

(5) Pudasaini, N.; Upadhyay, P. P.; Parker, C. R.; Hagen, S. U.; Bond, A. D.; Rantanen, J. Downstream Processability of Crystal Habit-Modified Active Pharmaceutical Ingredient. *Org. Process Res. Dev.* **2017**, *21* (4), 571–577. https://doi.org/10.1021/acs.oprd.6b00434.

(6) Banga, S.; Chawla, G.; Varandani, D.; Mehta, B. R.; Bansal, A. K. Modification of the Crystal Habit of Celecoxib for Improved Processability. *J. Pharm. Pharmacol.* **2007**, *59* (1), 29–39. https://doi.org/10.1211/jpp.59.1.0005.

(7) Shah, U. V.; Karde, V.; Ghoroi, C.; Heng, J. Y. Y. Influence of Particle Properties on Powder Bulk Behaviour and Processability. *Int. J. Pharm.* **2017**, *518* (1), 138–154. https://doi.org/10.1016/j.ijpharm.2016.12.045.

(8) Sun, C.; Grant, D. J. W. Influence of Crystal Shape on the Tableting Performance of L-Lysine Monohydrochloride Dihydrate. *J. Pharm. Sci.* **2001**, *90* (5), 569–579. https://doi.org/10.1002/1520-6017(200105)90:5%3C569::AID-JPS1013%3E3.0.CO;2-4.

(9) Wu, H.; Wang, J.; Xiao, Y.; Huang, X.; Guo, Y.; Zong, S.; Liu, Q.; Hao, Y.; Hao, H. Manipulation of Crystal Morphology of Zoxamide Based on Phase Diagram and Crystal Structure Analysis. *Cryst. Growth Des.* **2018**, *18* (10), 5790–5799. https://doi.org/10.1021/acs.cgd.8b00320.

(10) Suresh, K.; Aulakh, D.; Purewal, J.; Siegel, D. J.; Veenstra, M.; Matzger, A. J. Optimizing Hydrogen Storage in MOFs through Engineering of Crystal Morphology and Control of Crystal Size. *J. Am. Chem. Soc.* **2021**, *143* (28), 10727–10734. https://doi.org/10.1021/jacs.1c04926.

(11) Fiske, T. J.; Railkar, S. B.; Kalyon, D. M. Effects of Segregation on the Packing of Spherical and Nonspherical Particles. *Powder Technol.* **1994**, *81* (1), 57–64. https://doi.org/10.1016/0032-5910(94)02862-1.

(12) Li, G.; Zhang, C. Review of the Molecular and Crystal Correlations on Sensitivities of Energetic Materials. *J. Hazard. Mater.* **2020**, *398*, 122910. https://doi.org/10.1016/j.jhazmat.2020.122910.
(13) Song, X.; Wang, Y.; An, C.; Guo, X.; Li, F. Dependence of Particle Morphology and Size on the Mechanical Sensitivity and Thermal Stability of Octahydro-1,3,5,7-Tetranitro-1,3,5,7-Tetrazocine. *J. Hazard. Mater.* **2008**, *159* (2), 222–229. https://doi.org/10.1016/j.jhazmat.2008.02.009.
(14) Chen, H.; Li, L.; Jin, S.; Chen, S.; Jiao, Q. Effects of Additives on ε-HNIW Crystal Morphology and Impact Sensitivity. *Propellants Explos. Pyrotech.* **2012**, *37* (1), 77–82. https://doi.org/10.1002/prep.201000014.
(15) Li, H.; Zhou, X.; Xu, R.; Hao, S.; Chen, D.; Zhou, X. Anomalous Sensitivity Related to Crystal Characteristics of 2,6-Diamino-3,5-Dinitropyrazing-1-Oxide (LLM-105). *Energ. Mater. Front.* **2020**, *1* (3), 178–185. https://doi.org/10.1016/j.enmf.2020.12.001.
(16) Dandekar, P.; Kuvadia, Z. B.; Doherty, M. F. Engineering Crystal Morphology. *Annu. Rev. Mater. Res.* **2013**, *43* (1), 359–386. https://doi.org/10.1146/annurev-matsci-071312-121623.
(17) van der Heijden, A. E. D. M.; Bouma, R. H. B. Crystallization and Characterization of RDX, HMX, and CL-20. *Cryst. Growth Des.* **2004**, *4* (5), 999–1007. https://doi.org/10.1021/cg049965a.
(18) ter Horst, J. H.; Geertman, R. M.; van der Heijden, A. E.; van Rosmalen, G. M. The Influence of a Solvent on the Crystal Morphology of RDX. *J. Cryst. Growth* **1999**, *198–199*, 773–779. https://doi.org/10.1016/S0022-0248(98)01157-9.
(19) Li, J.-S.; Wu, S.-W.; Lu, K.-T. Study on Preparation of Insensitive and Spherical High Bulk Density Nitroguanidine with Controllable Particle Size. *Propellants Explos. Pyrotech.* **2016**, *41* (2), 312–320. https://doi.org/10.1002/prep.201500153.
(20) Song, L.; Zhao, F.-Q.; Xu, S.-Y.; Ju, X.-H.; Ye, C.-C. Crystal Morphology Prediction and Anisotropic Evolution of 1,1-Diamino-2,2-Dinitroethylene (FOX-7) by Temperature Tuning. *Sci. Rep.* **2020**, *10* (1), 2317. https://doi.org/10.1038/s41598-020-59261-3.
(21) Liang, Z.; Zhang, M.; Wu, F.; Chen, J.-F.; Xue, C.; Zhao, H. Supersaturation Controlled Morphology and Aspect Ratio Changes of Benzoic Acid Crystals. *Comput. Chem. Eng.* **2017**, *99*, 296–303. https://doi.org/10.1016/j.compchemeng.2017.01.010.
(22) Davey, R. J.; Garside, J. *From Molecules to Crystallizers*; Oxford Chemistry Primers; Oxford University Press: Oxford, New York, 2001.
(23) Meenan, P. A.; Anderson, S. R.; Klug, D. L. The Influence of Impurities and Solvents on Crystallization. In *Handbook of Industrial Crystallization*; Elsevier, 2002; pp 67–100.
(24) Weissbuch, I.; Popovitz-Biro, R.; Lahav, M.; Leiserowitz, L.; Rehovot. Understanding and Control of Nucleation, Growth, Habit, Dissolution and Structure of Two- and Three-Dimensional Crystals Using `tailor-Made' Auxiliaries. *Acta Crystallogr. Sect. B* **1995**, *51* (2), 115–148. https://doi.org/10.1107/S0108768194012061.
(25) Weissbuch, I.; Lahav, M.; Leiserowitz, L. Toward Stereochemical Control, Monitoring, and Understanding of Crystal Nucleation. *Cryst. Growth Des.* **2003**, *3* (2), 125–150. https://doi.org/10.1021/cg0200560.
(26) J. Davey, R.; N. Black, S.; Logan, D.; J. Maginn, S.; E. Fairbrother, J.; W. Grant, D. J. Structural and Kinetic Features of Crystal Growth Inhibition: Adipic Acid Growing in the Presence of n -Alkanoic Acids. *J. Chem. Soc. Faraday Trans.* **1992**, *88* (23), 3461–3466. https://doi.org/10.1039/FT9928803461.

(27) Hendriksen, B. A.; Grant, D. J. W.; Meenan, P.; Green, D. A. Crystallisation of Paracetamol (Acetaminophen) in the Presence of Structurally Related Substances. *J. Cryst. Growth* **1998**, *183* (4), 629–640. https://doi.org/10.1016/S0022-0248(97)00488-0.
(28) Poornachary, S. K.; Chow, P. S.; Tan, R. B. H.; Davey, R. J. Molecular Speciation Controlling Stereoselectivity of Additives: Impact on the Habit Modification in α-Glycine Crystals. *Cryst. Growth Des.* **2007**, *7* (2), 254–261. https://doi.org/10.1021/cg060273r.
(29) Luo, Z.; Cui, Y.; Dong, W.; Xu, Q.; Zou, G.; Kang, C.; Hou, B.; Chen, S.; Gong, J. Morphological Diversity of Nitroguanidine Crystals with Enhanced Mechanical Performance and Thermodynamic Stability. *J. Cryst. Growth* **2017**, *480*, 132–140. https://doi.org/10.1016/j.jcrysgro.2017.10.012.
(30) Capellades, G.; O. Bonsu, J.; S. Myerson, A. Impurity Incorporation in Solution Crystallization: Diagnosis, Prevention, and Control. *CrystEngComm* **2022**, *24* (11), 1989–2001. https://doi.org/10.1039/D1CE01721G.
(31) Nicolau, S. T.; Matzger, A. J. Sensitizing Explosives Through Molecular Doping. *ChemPlusChem* **2024**, *89* (6), e202300724. https://doi.org/10.1002/cplu.202300724.
(32) Bennion, J. C.; Matzger, A. J. Development and Evolution of Energetic Cocrystals. *Acc. Chem. Res.* **2021**. https://doi.org/10.1021/acs.accounts.0c00830.
(33) Klapwijk, A. R.; Simone, E.; Nagy, Z. K.; Wilson, C. C. Tuning Crystal Morphology of Succinic Acid Using a Polymer Additive. *Cryst. Growth Des.* **2016**, *16* (8), 4349–4359. https://doi.org/10.1021/acs.cgd.6b00465.
(34) Hatcher, L. E.; Li, W.; Payne, P.; Benyahia, B.; Rielly, C. D.; Wilson, C. C. Tuning Morphology in Active Pharmaceutical Ingredients: Controlling the Crystal Habit of Lovastatin through Solvent Choice and Non-Size-Matched Polymer Additives. *Cryst. Growth Des.* **2020**, *20* (9), 5854–5862. https://doi.org/10.1021/acs.cgd.0c00470.
(35) Pfund, L. Y.; Price, C. P.; Frick, J. J.; Matzger, A. J. Controlling Pharmaceutical Crystallization with Designed Polymeric Heteronuclei. *J. Am. Chem. Soc.* **2015**, *137* (2), 871–875. https://doi.org/10.1021/ja511106j.
(36) Simone, E.; Cenzato, M. V.; Nagy, Z. K. A Study on the Effect of the Polymeric Additive HPMC on Morphology and Polymorphism of Ortho-Aminobenzoic Acid Crystals. *J. Cryst. Growth* **2016**, *446*, 50–59. https://doi.org/10.1016/j.jcrysgro.2016.04.034.
(37) Zhou, X.; Ren, Y.; Li, H.; Zhou, X.; Hao, S.; Xu, R.; Zhang, Q. Polymer-Directed Crystallization of HMX to Construct Nano-/Microstructured Aggregates with Tunable Polymorph and Microstructure. *CrystEngComm* **2022**, *24* (4), 755–764. https://doi.org/10.1039/D1CE01428E.
(38) Yang, J.; Cui, Y.; Chen, M.; Wang, Y.; Xu, S.; Wu, S.; Wang, J.; Gong, J. Transformation between Two Types of Spherulitic Growth: Tuning the Morphology of Spherulitic Nitroguanidine in a Gelatin Solution. *Ind. Eng. Chem. Res.* **2020**, *59* (48), 21167–21176. https://doi.org/10.1021/acs.iecr.0c03039.
(39) Mudryy, R.; Damavarapu, R.; Stepanov, V.; Halder, R. *Crystallization of High Bulk Density Nitroguanidin*e.; ADA545344; Army Armament Research, Development and Engineering Center, Picatinny Arsenal, NJ. Energetics Warheads and Manufacturing Technology Directorate., 2011. https://ntrl.ntis.gov/NTRL/dashboard/searchResults/titleDetail/ADA545344.xhtml (accessed 2023-01-30).

(40) Zhou, X.; Zhang, Q.; Xu, R.; Chen, D.; Hao, S.; Nie, F.; Li, H. A Novel Spherulitic Self-Assembly Strategy for Organic Explosives: Modifying the Hydrogen Bonds by Polymeric Additives in Emulsion Crystallization. *Cryst. Growth Des.* **2018**, *18* (4), 2417–2423. https://doi.org/10.1021/acs.cgd.8b00044.
(41) Li, M.; Wang, Y.; Zhou, X.; Zhang, Q.; Chen, M.; Han, D.; Gong, J.; Li, H. Fabrication of Micro/Nano Spherulitic Hierarchical Energetic Materials via Noncrystallographic Branching Induced by Polymer Additives: A Case Study of 2,2′,4,4′,6,6′-Hexanitrostilbene (HNS). *Chem. Eng. J.* **2023**, *462*, 142162. https://doi.org/10.1016/j.cej.2023.142162.
(42) Zhou, X.; Li, H.; Zhou, X.; Hao, S.; Yan, M.; Zou, P.; Huang, S.; He, X.; Zhang, C. Imparting High Polymorph Transition Resistance to Cyclotetramethylene-Tetranitramine via Spherulitic Aggregation Enabled Crystal Shape Constraint. *Chem. Eng. J.* **2023**, *452*, 139602. https://doi.org/10.1016/j.cej.2022.139602.
(43) Koch, E.-C. Insensitive High Explosives: IV. Nitroguanidine – Initiation & Detonation. *Def. Technol.* **2019**, *15* (4), 467–487. https://doi.org/10.1016/j.dt.2019.05.009.
(44) Sanghavi, R. R.; Pillai, A. G. S.; Velapure, S. P.; Singh, A. Studies on Different Types of Nitrocellulose in Triple Base Gun Propellant Formulations. *J. Energ. Mater.* **2003**, *21* (2), 87–95. https://doi.org/10.1080/713845496.
(45) Chapman, R. D. Organic Difluoramine Derivatives. In *High Energy Density Materials*; Klapötke, T. M., Ed.; Springer: Berlin, Heidelberg, 2007; pp 123–151. https://doi.org/10.1007/430_2007_058.
(46) Degirmenbasi, N.; Peralta-Inga, Z.; Olgun, U.; Gocmez, H.; Kalyon, D. M. Recrystallization of CL-20 and HNFX from Solution for Rigorous Control of the Polymorph Type: Part II, Experimental Studies. *J. Energ. Mater.* **2006**, *24* (2), 103–139. https://doi.org/10.1080/07370650600672090.
(47) Herrmannsdörfer, D.; Stierstorfer, J.; Klapötke, T. M. Solubility Behaviour of CL-20 and HMX in Organic Solvents and Solvates of CL-20. *Energ. Mater. Front.* **2021**. https://doi.org/10.1016/j.enmf.2021.01.004.
(48) Lang, M.; Grzesiak, A. L.; Matzger, A. J. The Use of Polymer Heteronuclei for Crystalline Polymorph Selection. *J. Am. Chem. Soc.* **2002**, *124* (50), 14834–14835. https://doi.org/10.1021/ja0286526.
(49) Price, C. P.; Grzesiak, A. L.; Matzger, A. J. Crystalline Polymorph Selection and Discovery with Polymer Heteronuclei. *J. Am. Chem. Soc.* **2005**, *127* (15), 5512–5517. https://doi.org/10.1021/ja042561m.
(50) Lin, H.; Zhu, S.-G.; Li, H.-Z.; Peng, X.-H. Synthesis, Characterization, AIM and NBO Analysis of HMX/DMI Cocrystal Explosive. *J. Mol. Struct.* **2013**, *1048*, 339–348. https://doi.org/10.1016/j.molstruc.2013.06.013.
(51) Landenberger, K. B.; Matzger, A. J. Cocrystals of 1,3,5,7-Tetranitro-1,3,5,7-Tetrazacyclooctane (HMX). *Cryst. Growth Des.* **2012**, *12* (7), 3603–3609. https://doi.org/10.1021/cg3004245.
(52) Politzer, P.; Murray, J. S.; Concha, M. C. Halogen Bonding and the Design of New Materials: Organic Bromides, Chlorides and Perhaps Even Fluorides as Donors. J. *Mol. Model.* **2007**, *13* (6), 643–650. https://doi.org/10.1007/s00894-007-0176-9.
(53) Metrangolo, P.; Murray, J. S.; Pilati, T.; Politzer, P.; Resnati, G.; Terraneo, G. Fluorine-Centered Halogen Bonding: A Factor in Recognition Phenomena and Reactivity. *Cryst. Growth Des.* **2011**, *11* (9), 4238–4246. https://doi.org/10.1021/cg200888n.

(54) Li, W.; Zeng, Y.; Zhang, X.; Zheng, S.; Meng, L. The Enhancing Effects of Group V σ-Hole Interactions on the F···O Halogen Bond. *Phys. Chem. Chem. Phys.* **2014**, *16* (36), 19282–19289. https://doi.org/10.1039/C4CP02430C.
(55) Lu, Y.-X.; Zou, J.-W.; Yu, Q.-S.; Jiang, Y.-J.; Zhao, W.-N. Ab Initio Investigation of Halogen Bonding Interactions Involving Fluorine as an Electron Acceptor. *Chem. Phys. Lett.* **2007**, *449* (1), 6–10. https://doi.org/10.1016/j.cplett.2007.09.087.
(56) Hua, A. M.; Bidwell, S. L.; Baker, S. I.; Hratchian, H. P.; Baxter, R. D. Experimental and Theoretical Evidence for Nitrogen–Fluorine Halogen Bonding in Silver-Initiated Radical Fluorinations. *ACS Catal.* **2019**, *9* (4), 3322–3326. https://doi.org/10.1021/acscatal.9b00623.
(57) Eskandari, K.; Lesani, M. Does Fluorine Participate in Halogen Bonding? *Chem. – Eur. J.* **2015**, *21* (12), 4739–4746. https://doi.org/10.1002/chem.201405054.
(58) Kent, R. V.; Wiscons, R. A.; Sharon, P.; Grinstein, D.; Frimer, A. A.; Matzger, A. J. Cocrystal Engineering of a High Nitrogen Energetic Material. *Cryst. Growth Des.* **2018**, *18* (1), 219–224. https://doi.org/10.1021/acs.cgd.7b01126.
(59) Bennion, J. C.; McBain, A.; Son, S. F.; Matzger, A. J. Design and Synthesis of a Series of Nitrogen-Rich Energetic Cocrystals of 5,5′-Dinitro-2H,2H′-3,3′-Bi-1,2,4-Triazole (DNBT). *Cryst. Growth Des.* **2015**, *15* (5), 2545–2549. https://doi.org/10.1021/acs.cgd.5b00336.
(60) Civati, F.; O'Malley, C.; Erxleben, A.; McArdle, P. Factors Controlling Persistent Needle Crystal Growth: The Importance of Dominant One-Dimensional Secondary Bonding, Stacked Structures, and van Der Waals Contact. *Cryst. Growth Des.* **2021**, *21* (6), 3449–3460. https://doi.org/10.1021/acs.cgd.1c00217.
(61) Lin, H.; Chen, J.-F.; Zhu, S.-G.; Li, H.-Z.; Huang, Y. Synthesis, Characterization, Detonation Performance, and DFT Calculation of HMX/PNO Cocrystal Explosive. *J. Energ. Mater.* **2017**, *35* (1), 95–108. https://doi.org/10.1080/07370652.2016.1172681.

Chapter 5 Conclusion and Future Directions

In this thesis, tailored additive-based crystallization strategies were utilized to control energetic properties. In *Chapter 2*, molecular doping of an impact sensitive primary explosive into a secondary explosive led to the control of sensitivity. For three energetics, doping imparted increased sensitivity to impact, with one host achieving a sensitivity level to qualify its use as a primary explosive. This specific design of molecular doping is particularly useful when considering the need for "green" metal-free primary explosives, in order to reduce the environmental and health concerns related to toxic-metal containing primary energetics that are still wildly used. Further studies are needed to validate the sensitized material as a potential replacement for lead-based materials, specifically: proper aging studies to ensure stability, additional sensitivity testing (friction and electrostatic discharge) and brisance (the ability to shatter upon detonation) testing.[1–4]

Admittedly, sensitization of the host energetic in Chapter 2 was not as dramatic as expected given the high sensitivity of the dopant. Based on the rapid crystallization from melt, it was hypothesized that the presented doping route is kinetically driven, but it is unclear if doping is an equilibrium product or kinetic. This prompts further studies on the doping mechanism via melt cycling and variable cooling rate studies, and inquiry on if a less kinetically driven crystallization (i.e., solution-based cooling crystallization) would allow for more incorporation and thus likely further sensitization. Additionally, the control over sensitivity may be linked to the dopant itself, and probing other impact sensitive, primary explosive dopants (DiAT, ICM-

103, ANTPA and DDNP; Figure 5.1)[5–9] will allow for better understanding of the sensitization factor. Alteration of the dopant will examine how chemical similarity influences incorporation, and if simply starting with a more sensitive dopant improves sensitivity control. For example, DiAT is structurally similar to CTA and has comparable sensitivity, but DDNP offers new functionality to probe along with increased sensitivity.

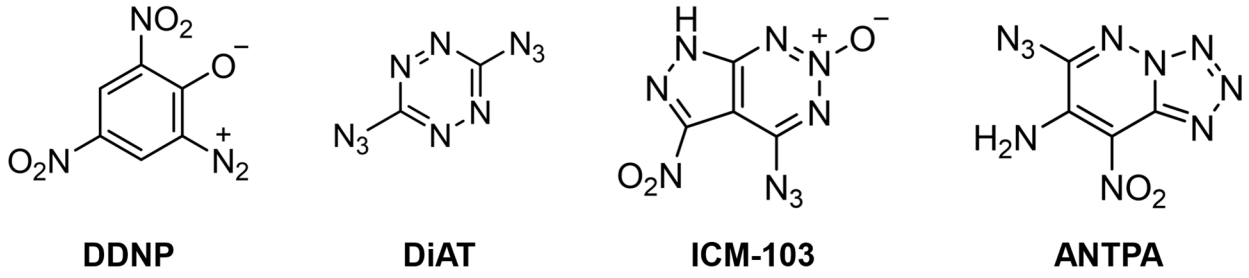


Figure 5.1 Potential primary explosive dopants.

Regardless of dopant choice, an improved understanding on the distribution of dopant in the energetic composite is needed. While Raman offers spatial resolution on the order of 1 μm, features on the nm-μm scale can influence sensitivity via aggregation and hot spot mechanisms.[10–12] Future work should seek to analyze heterogeneity using near-field scanning optical microscopy (NSOM), tip-enhanced Raman spectroscopy (TERS), and/or nano-FTIR spectroscopy, which affords spatial resolution on the nanometer scale.[13–15] Molecular doping also has potential to be used more broadly beyond sensitivity control, serving as a workhorse energetic to be applied to different applications by tailoring the dopant. For example, future work will likely render explosives responsive to optical or thermal stimuli with a judicious choice of dopant. Because molecular doping proceeds as a type of impurity incorporation, these project extensions will be realized at low levels of dopant, relying heavily on proper characterization.

Understanding small nuances in IR datasets is pertinent to improve the elucidation of chemical structure and crystal packing, whether it be rearrangement in polymorphism or lattice

incorporation in molecular doping. One technique proven successful for verifying molecular doping was IR spectroscopy, and in *Chapter 3*, a thorough discussion was presented on resolution, precision, accuracy, and sources of error in the technique. It was concluded that for well resolved peaks that are not saturated, instrument variation results in a wavenumber accuracy within 1.1 cm^{-1} for spectral resolutions of 4 cm^{-1} or higher and within 2.2 cm^{-1} for spectral resolutions of 8 cm^{-1}. However, these values represent the extremes of error in the positions, as the average wavenumber accuracies were within 0.5 cm^{-1} and 0.9 cm^{-1} (at 4 cm^{-1} and 8 cm^{-1} spectral resolution, respectively).

One drawback of transmission IR spectroscopy for dopant analysis is the ability to obtain sufficiently thin samples to avoid saturation; this also becomes particularly important if the dopant bands of interest move out of the overtone region. Shearing to generate a thin sub-sample may not be viable for some sensitive energetic materials, and therefore, exploration of other sampling strategies like ATR IR mapping may be needed. Sensitivity is also a lingering concern for detection of low dopant levels. While IR spectroscopy generally has the sensitivity needed to detect the dopant when utilizing transmission sampling with chilled detectors, the main issue arises from overlap in dopant bands with host bands. Additional advanced post-processing may lead to better subtraction and/or deconvolution of the host from the dopant, but this also motivates the use of cold (sample) IR spectroscopy to monitor dopant, as reduced temperature should lead to higher intensity and narrower bands.[16]

In *Chapter 4,* the theme of tailored additive-based crystallizations was continued, where polymeric additives were designed to interact face selectively and control the crystal morphology, and thus related properties, of explosives. This specific workflow was achieved by utilizing cocrystal motifs found in a specific cocrystal library, tethering them to a soluble

polymer backbone, and applying them to three explosives. For two explosives, morphology was altered from a needle to a more blocky shape that should improve packing density and processability if they were to be loaded into a munition. Explosives that lack the ability to be easily melted into a casting, however, typically require the addition of polymer binders for proper loading (termed polymer-bonded explosive, or PBX). Further studies are needed to test the compatibility of the shape-modified crystals with the binder, particularly if additional polymer remains adsorbed onto the surface below the detectable limits available with NMR spectroscopy. Atomic force microscopy can be used to probe the mechanical properties of the crystal surface to determine if polymer residue is present.[17] Residual polymer could be utilized in scenarios where there are interphase issues with the desired binder and explosive crystals; a blending interaction between an intermediate polymer layer (on the crystal) may promote better adhesion with tailored interfacial chemistry. In either scenario, with or without polymer, blend uniformity of loaded shape-modified crystals into PBX binder should be characterized, likely through micro-computed tomography[18,19], for initial void analysis and delamination studies that mimic material response to stress.

Successful modification of crystal shape in Chapter 4 more generally, however, demonstrated that molecular interactions targeted for one explosive can be transferable to others given the reoccurring functional groups of energetic materials. For example, some explosives developed for insensitive munitions (e.g. LLM-105, HNS) present in needle or blade morphologies[20,21] and could see future application into this workflow; supplementary models with cocrystals (e.g. TNT, CL-20) to draw interaction motif inspiration may be needed. Additionally, utilization of polymeric additives may provide an additional route for desensitization of explosives in future work, particularly if a high enough additive concentration

is utilized to retain polymer on the surface of the crystal as a void buffer. Lastly, although the utility of additives imparting greater shape control than their monomeric counterparts was probed in this work, further mechanistic study is needed to identify what molecular weight regime balances multisite interactions for greater control with better polymer properties.

In summary, additive-based crystal engineering has proven useful in controlling properties of energetic materials. Tunable approaches, like molecular doping and crystallization in the presence of face-selective shape modifiers, can allow for "recycling" of materials that were greatly invested in as superior energetics but fell short of fielding. This seeks to make material discovery a greener process for explosives by reducing additional production of inferior and/or toxic materials while also contributing broadly to new crystallization strategies.

5.1 References

(1) Vogelsanger, B. Chemical Stability, Compatibility and Shelf Life of Explosives. *CHIMIA* **2004**, *58* (6), 401–401. https://doi.org/10.2533/000942904777677740.

(2) Matyáš, R.; Pachman, J. *Primary Explosives*; Springer: Berlin, Heidelberg, 2013. https://doi.org/10.1007/978-3-642-28436-6.

(3) Afanasenkov, A. N. Strength of Explosives. Trauzl Test. *Combust. Explos. Shock Waves* **2004**, *40* (1), 119–125. https://doi.org/10.1023/B:CESW.0000013674.96586.b9.

(4) Sandstrom, M. M.; Brown, G. W.; Preston, D. N.; Pollard, C. J.; Warner, K. F.; Sorensen, D. N.; Remmers, D. L.; Phillips, J. J.; Shelley, T. J.; Reyes, J. A.; Hsu, P. C.; Reynolds, J. G. Variation of Methods in Small-Scale Safety and Thermal Testing of Improvised Explosives. *Propellants Explos. Pyrotech.* **2015**, *40* (1), 109–126. https://doi.org/10.1002/prep.201400108.

(5) *Green Energetic Materials | Wiley*. Wiley.com. https://www.wiley.com/en-us/Green+Energetic+Materials-p-9781118676462 (accessed 2025-03-29).

(6) Huynh, M. H. V.; Hiskey, M. A.; Meyer, T. J.; Wetzler, M. Green Primaries: Environmentally Friendly Energetic Complexes. *Proc. Natl. Acad. Sci. U. S. A.* **2006**, *103* (14), 5409–5412.

(7) Deng, M.; Feng, Y.; Zhang, W.; Qi, X.; Zhang, Q. A Green Metal-Free Fused-Ring Initiating Substance. *Nat. Commun.* **2019**, *10* (1), 1339. https://doi.org/10.1038/s41467-019-09347-y.

(8) Huang, W.; Tang, Y.; Imler, G. H.; Parrish, D. A.; Shreeve, J. M. Nitrogen-Rich Tetrazolo[1,5-b]Pyridazine: Promising Building Block for Advanced Energetic Materials. *J. Am. Chem. Soc.* **2020**, *142* (7), 3652–3657. https://doi.org/10.1021/jacs.0c00161.

(9) Feng, Y.; Zhang, J.; Cao, W.; Zhang, J.; Shreeve, J. M. A Promising Perovskite Primary Explosive. *Nat. Commun.* **2023**, *14*, 7765. https://doi.org/10.1038/s41467-023-43320-0.

(10) Johnson, B. P.; Zhou, X.; Ihara, H.; Dlott, D. D. Observing Hot Spot Formation in Individual Explosive Crystals Under Shock Compression. *J. Phys. Chem. A* **2020**, *124* (23), 4646–4653. https://doi.org/10.1021/acs.jpca.0c02788.
(11) Tarver, C. M.; Chidester, S. K.; Nichols, A. L. Critical Conditions for Impact- and Shock-Induced Hot Spots in Solid Explosives. *J. Phys. Chem.* **1996**, *100* (14), 5794–5799. https://doi.org/10.1021/jp953123s.
(12) Bowden, F. P.; Yoffe, A. Hot Spots and the Initiation of Explosion. *Symp. Combust. Flame Explos. Phenom.* **1948**, *3* (1), 551–560. https://doi.org/10.1016/S1062-2896(49)80074-2.
(13) Dürig, U.; Pohl, D. W.; Rohner, F. Near-field Optical-scanning Microscopy. *J. Appl. Phys.* **1986**, *59* (10), 3318–3327. https://doi.org/10.1063/1.336848.
(14) Zhang, Z.; Sheng, S.; Wang, R.; Sun, M. Tip-Enhanced Raman Spectroscopy. *Anal. Chem.* **2016**, *88* (19), 9328–9346. https://doi.org/10.1021/acs.analchem.6b02093.
(15) Mester, L.; Govyadinov, A. A.; Chen, S.; Goikoetxea, M.; Hillenbrand, R. Subsurface Chemical Nanoidentification by Nano-FTIR Spectroscopy. *Nat. Commun.* **2020**, *11* (1), 3359. https://doi.org/10.1038/s41467-020-17034-6.
(16) Asselin, M.; Sandorfy, C. A Low Temperature Infrared Study of the Band-Width and Frequency in Self-Associated Alcohols. *Chem. Phys. Lett.* **1971**, *8* (6), 601–603. https://doi.org/10.1016/0009-2614(71)80104-5.
(17) Moseson, D. E.; Parker, A. S.; Beaudoin, S. P.; Taylor, L. S. Amorphous Solid Dispersions Containing Residual Crystallinity: Influence of Seed Properties and Polymer Adsorption on Dissolution Performance. *Eur. J. Pharm. Sci.* **2020**, *146*, 105276. https://doi.org/10.1016/j.ejps.2020.105276.
(18) Walters, D. J.; Luscher, D. J.; Yeager, J. D.; Patterson, B. M. Cohesive Finite Element Modeling of the Delamination of HTPB Binder and HMX Crystals under Tensile Loading. *Int. J. Mech. Sci.* **2018**, *140*, 151–162. https://doi.org/10.1016/j.ijmecsci.2018.02.048.
(19) Manner, V. W.; Yeager, J. D.; Patterson, B. M.; Walters, D. J.; Stull, J. A.; Cordes, N. L.; Luscher, D. J.; Henderson, K. C.; Schmalzer, A. M.; Tappan, B. C. In Situ Imaging during Compression of Plastic Bonded Explosives for Damage Modeling. *Materials* **2017**, *10* (6), 638. https://doi.org/10.3390/ma10060638.
(20) Zhou, X.; Shan, J.; Chen, D.; Li, H. Tuning the Crystal Habits of Organic Explosives by Antisolvent Crystallization: The Case Study of 2,6-Dimaino-3,5-Dinitropyrazine-1-Oxid (LLM-105). *Crystals* **2019**, *9* (8), 392. https://doi.org/10.3390/cryst9080392.
(21) Song, L.; Zhao, F.-Q.; Xu, S.-Y.; Ju, X.-H. Crystal Morphology Prediction of 2,2′,4,4′,6,6’-Hexanitrostilbene (HNS) by Molecular Scale Simulation. *J. Mol. Model.* **2020**, *26* (8), 213. https://doi.org/10.1007/s00894-020-04474-6.

Appendices

Appendix A: *From Chapter 2* – Sensitizing Explosives Through Molecular Doping

A.1 Supplementary Data

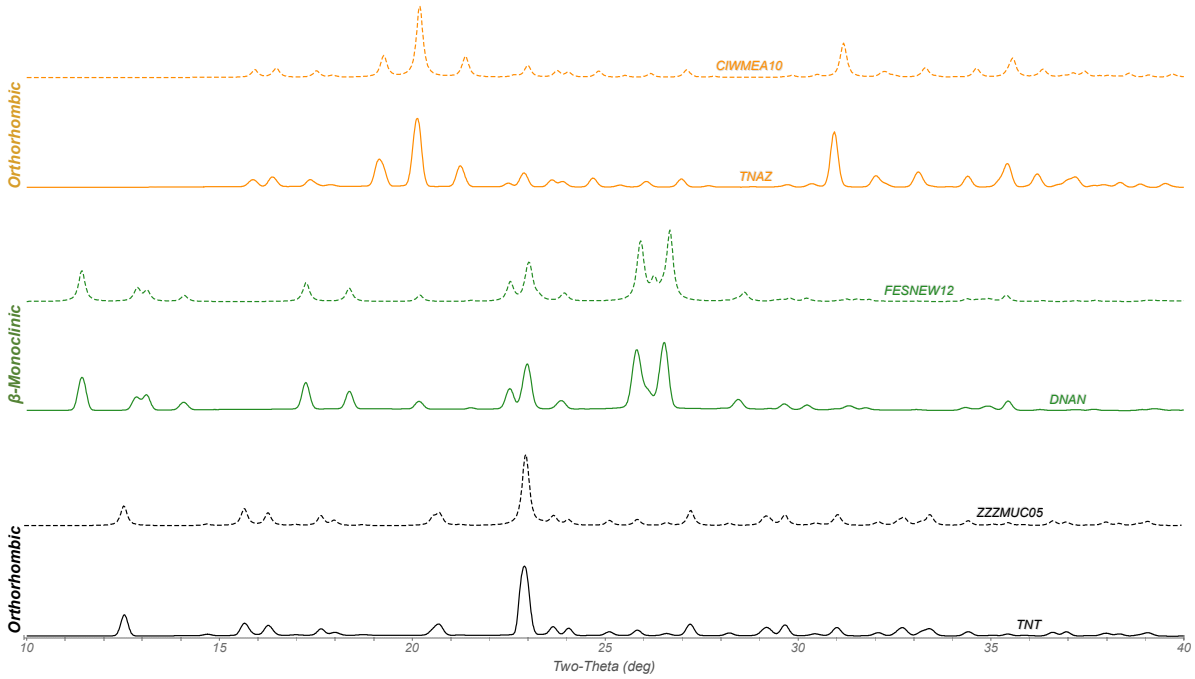


Figure A.1 Secondary energetics crystallized from melt. Each adopts a known form as shown by comparison to simulated PXRD patterns (peak setting FWHM: 0.2) corresponding to the Cambridge Structural Database (CSD) reference codes listed.

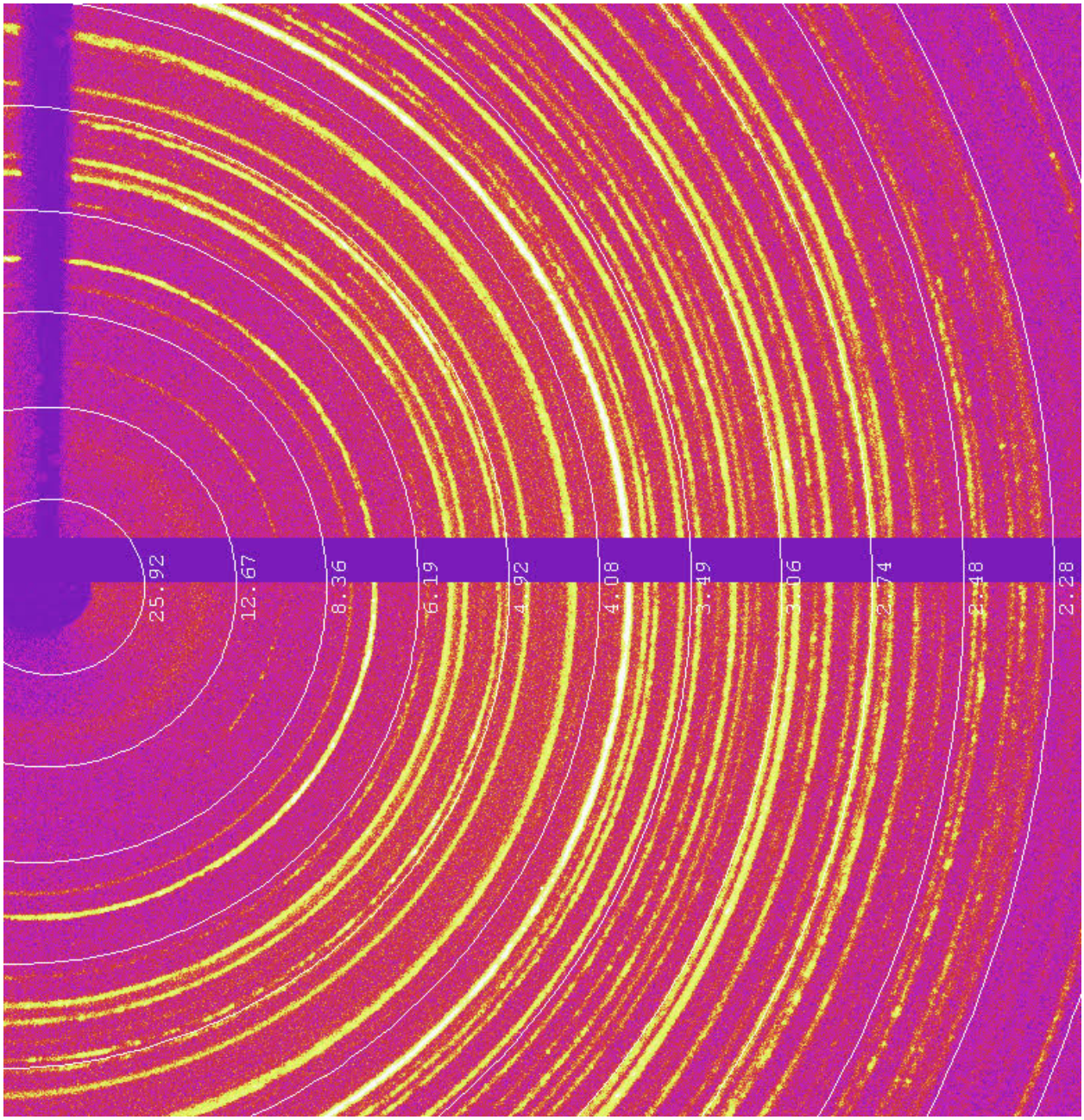


Figure A.2 A representative 2D-powder pattern collected using Gandolfi moves for powders to minimize effects of preferred orientation (sample shown is 10% CTA in TNT). 1D-powder patterns were extracted using CrysAlisPro v42.75a for analysis.

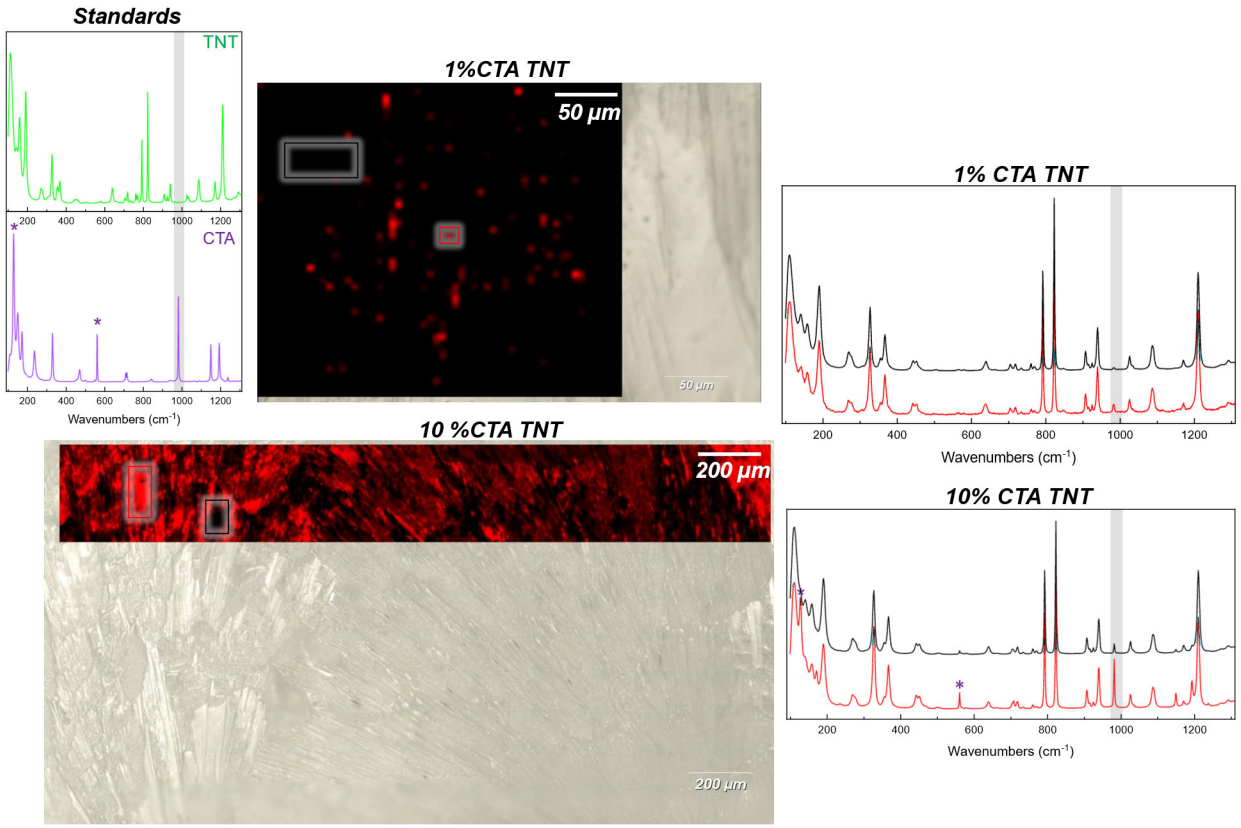


Figure A.3 Raman mapping of 1% vs. 10% CTA in TNT that shows distribution of CTA across melt. Representative spectra are shown for each loading based on regions of average CTA signal (color-coded black) and high CTA signal (color-coded red). In addition to the main CTA peak identified in average signal (grey box), additional CTA peaks (*) can be found in higher concentration areas.

Appendix B: *From Chapter 3* – An Evaluation of Resolution, Accuracy, and Precision in FT-IR Spectroscopy

B.1 Additional Experimental Details

Polystyrene (PS) was obtained as a secondary standard from Nicolet. Acetaminophen (APAP) was obtained from ICN Biomedicals. Potassium bromide (KBr) was obtained from Buck Scientific. Thorough grinding of ~ 1.5 mg of acetaminophen with ~396.8 mg of KBr using an agate mortar and pestle gave a sample loading of ~0.4%. In a 13 mm KBr pellet die, ~150 mg of ground sample was pressed at 10,000 lbs. The acetaminophen KBr pellet was stored under nitrogen between runs/experimental days.

Plots of FT-IR spectra were generated in Origin, unless noted.

B.2 Supplementary Information

B.2.1. Variable Instrument Peak Accuracy Using Native Instrument Software

Table B-1 Peak accuracy (cm^{-1}) for 9 PS NIST calibration peaks collected on four instruments at 4 cm^{-1} spectral resolution. Analysis was completed in the native instrument software using standard peak-picking parameters. [a]NIST values from traceability document provided in Supplementary Reference (1).

Peak	**NIST[a]**	**Nicolet**	**Bruker**	**Perkin-Elmer**	**Shimadzu**	**NIST-Nicolet**	**NIST-Bruker**	**NIST-PerkinElmer**	**NIST-Shimadzu**
1	3081.87	3081.82	3081.41	3082.23	3081.28	0.05	0.46	-0.36	0.59
2	3059.71	3059.73	3059.39	3060.17	3059.10	-0.02	0.32	-0.46	0.61
3	3025.64	3025.73	3025.46	3026.09	**3023.42[lobed]**	-0.09	0.18	-0.45	**2.22**
4	2849.28	2849.38	2849.14	2849.80	2848.86	-0.10	0.14	-0.52	0.42
5	1942.64	1942.67	1942.43	1942.98	1942.32	-0.03	0.21	-0.34	0.32
6	1601.15	1601.15	1600.83	1601.44	1600.92	0.00	0.32	-0.29	0.23
7	1028.41	1028.41	1028.11	1028.56	1028.06	0.00	0.30	-0.15	0.35
8	906.62	906.52	906.29	906.64	906.54	0.10	0.33	-0.02	0.08
9	539.63	539.75	539.60	539.56	539.59	-0.12	0.03	0.07	0.04

B.2.2. Variable Instrument Transmission FT-IR, with OMINC Software Analysis

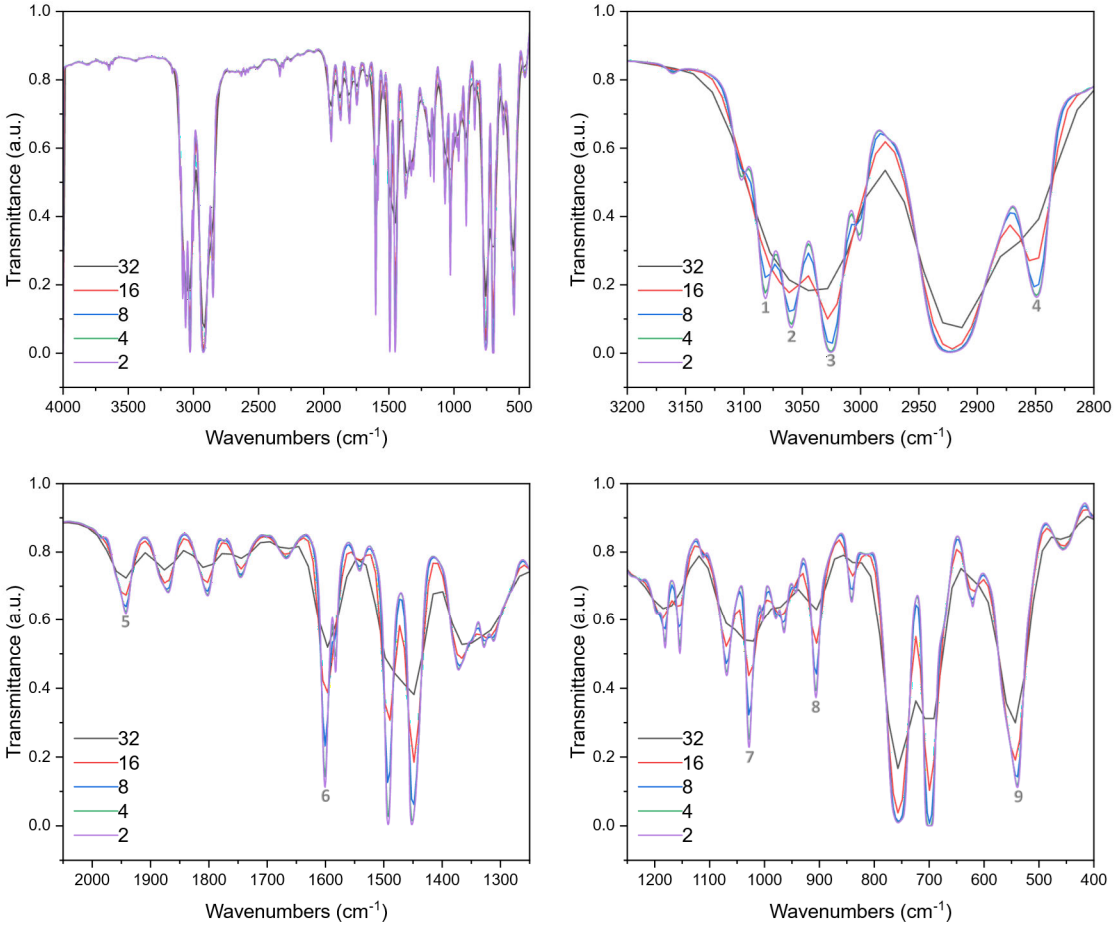


Figure B.1 Transmission FT-IR spectra of PS collected on a Bruker Alpha II with varied spectral resolutions from 32 – 2 cm^{-1}. Numbering denotes peaks in analysis.

Table B-2 Peak positions (cm^{-1})[ǂ] for PS collected on a Bruker Alpha II FT-IR at variable spectral resolutions. [ǂ]Wavenumbers were determined in OMNIC using the standard peak picking function. [ǂ]NR denotes peak that were unresolved at said resolution.

	32 cm^{-1}	**16 cm^{-1}**	**8 cm^{-1}**	**4 cm^{-1}**	**2 cm^{-1}**
Peak 1	NR [ǂ]	NR	3080.19	3081.35	3081.53
Peak 2	NR	NR	3059.43	3059.38	3059.37
Peak 3	NR	NR	3025.89	3025.47	3025.64
Peak 4	NR	2852.20	2849.84	2849.20	2849.04
Peak 5	1945.03	1944.76	1943.11	1942.47	1942.30
Peak 6	1595.98	1598.40	1600.48	1600.80	1600.82
Peak 7	1027.72	1026.51	1027.50	1028.08	1028.09
Peak 8	908.43	906.08	906.32	906.30	906.26
Peak 9	546.45	543.96	540.73	539.67	539.30

Table B-3 Peak position (cm^{-1})[ǂ] as a function of resolution for PS collected on a Bruker Alpha II FT-IR, as assessed by calculating the difference in assigned peak value from the value determined at 2 cm^{-1} (e.g. $\Delta 32\ cm^{-1} = peak_{2cm\text{-}1} - peak_{32cm\text{-}1}$). [ǂ]See Table B-2 for raw data. [ǂ]NR denotes peak that were unresolved at said resolution.

	Δ32 cm^{-1}	**Δ16 cm^{-1}**	**Δ8 cm^{-1}**	**Δ4 cm^{-1}**	**Δ2 cm^{-1}**
Peak 1	NR [ǂ]	NR	1.34	0.18	0
Peak 2	NR	NR	-0.06	-0.01	0
Peak 3	NR	NR	-0.25	0.17	0
Peak 4	NR	-3.16	-0.80	-0.16	0
Peak 5	-2.73	-2.46	-0.81	-0.17	0
Peak 6	4.84	2.42	0.34	0.02	0
Peak 7	0.37	1.58	0.59	0.01	0
Peak 8	-2.17	0.18	-0.06	-0.04	0
Peak 9	-7.15	-4.66	-1.43	-0.37	0
Average |Δ|	**3.45**	**2.26**	**0.63**	**0.13**	**-**

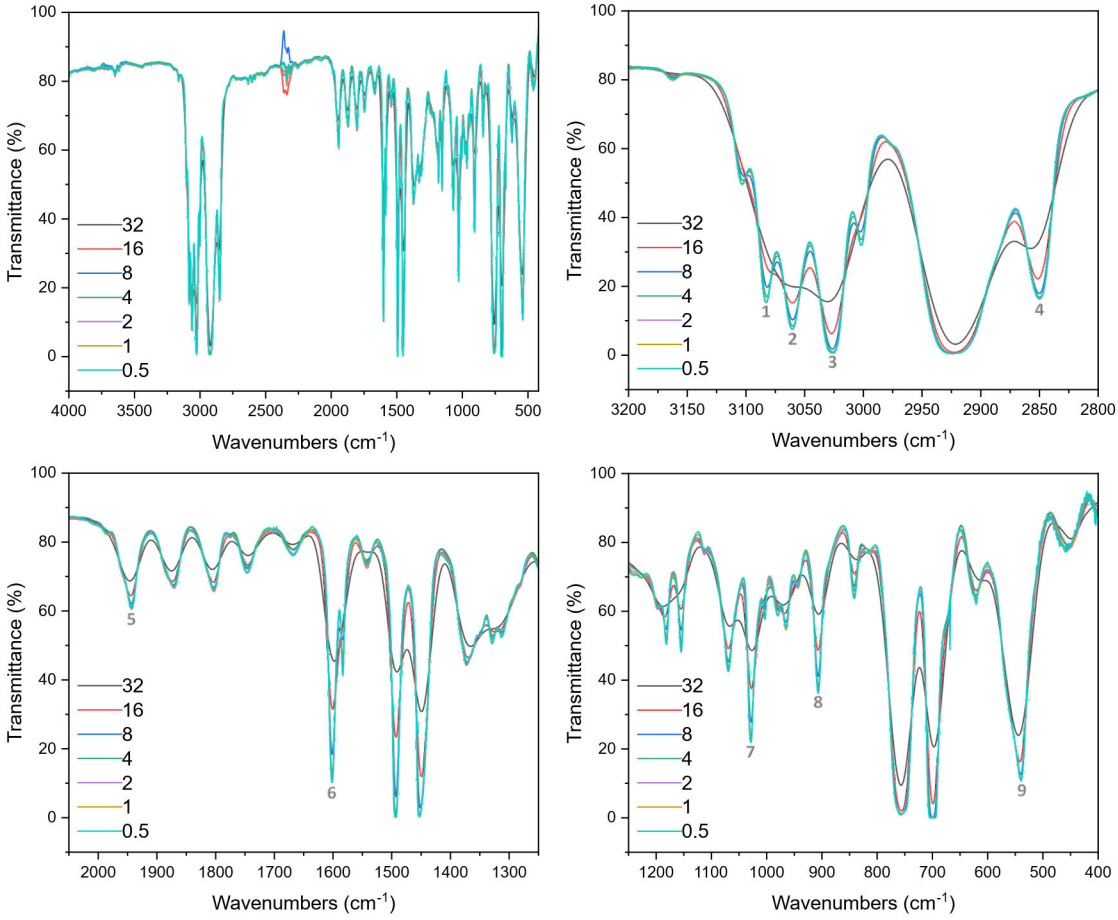


Figure B.2 Transmission FT-IR spectra of PS collected on a PerkinElmer Frontier with varied spectral resolutions from 32 – 0.5 cm^{-1}. Numbering denotes peaks in analysis.

Table B-4 Peak positions (cm^{-1})[ɬ] of PS collected on a PerkinElmer Frontier FT-IR at variable spectral resolutions. [ɬ]Wavenumbers were determined in OMNIC using the standard peak picking function. [ǂ]NR denotes peak that were unresolved at said resolution.

	32 cm^{-1}	**16 cm^{-1}**	**8 cm^{-1}**	**4 cm^{-1}**	**2 cm^{-1}**	**1 cm^{-1}**	**0.5 cm^{-1}**
Peak 1	NR [ǂ]	NR	3081.38	3082.16	3082.63	3082.75	3082.71
Peak 2	NR	NR	3060.15	3060.18	3060.45	3060.50	3060.41
Peak 3	NR	NR	3026.46	3026.18	3026.35	3026.15	3026.25
Peak 4	2860.28	2852.05	2850.38	2849.85	2849.96	2849.98	2849.92
Peak 5	1945.92	1944.96	1943.51	1942.98	1943.06	1943.02	1942.72
Peak 6	1597.74	1600.43	1601.16	1601.39	1601.54	1601.53	1601.48
Peak 7	1027.55	1026.86	1028.23	1028.54	1028.57	1028.42	1028.30
Peak 8	907.30	906.72	906.68	906.64	906.72	906.73	906.79
Peak 9	544.68	542.38	540.53	539.79	539.48	539.23	539.10

Table B-5 Peak position (cm^{-1})[ɬ] as a function of resolution for PS collected on a PerkinElmer Frontier FT-IR, as assessed by calculating the difference in assigned peak value from the value determined at 0.5 cm^{-1} (e.g.Δ32 cm^{-1} = $peak_{0.5cm\text{-}1} - peak_{32cm\text{-}1}$). [ɬ]See Table B-4 for raw data. [ǂ]NR denotes peak that were unresolved at said resolution.

	Δ32 cm^{-1}	**Δ16 cm^{-1}**	**Δ8 cm^{-1}**	**Δ4 cm^{-1}**	**Δ2 cm^{-1}**	**Δ1 cm^{-1}**	**Δ0.5 cm^{-1}**
Peak 1	NR [ǂ]	NR	1.33	0.55	0.08	-0.04	0
Peak 2	NR	NR	0.26	0.23	-0.04	-0.09	0
Peak 3	NR	NR	-0.21	0.07	-0.10	0.10	0
Peak 4	-10.36	-2.13	-0.46	0.07	-0.04	-0.06	0
Peak 5	-3.20	-2.24	-0.79	-0.26	-0.34	-0.30	0
Peak 6	3.74	1.05	0.32	0.09	-0.06	-0.05	0
Peak 7	0.75	1.44	0.07	-0.24	-0.27	-0.12	0
Peak 8	-0.51	0.07	0.11	0.15	0.07	0.06	0
Peak 9	-5.58	-3.28	-1.43	-0.69	-0.38	-0.13	0
Average |Δ|	**4.02**	**1.70**	**0.55**	**0.26**	**0.15**	**0.11**	**-**

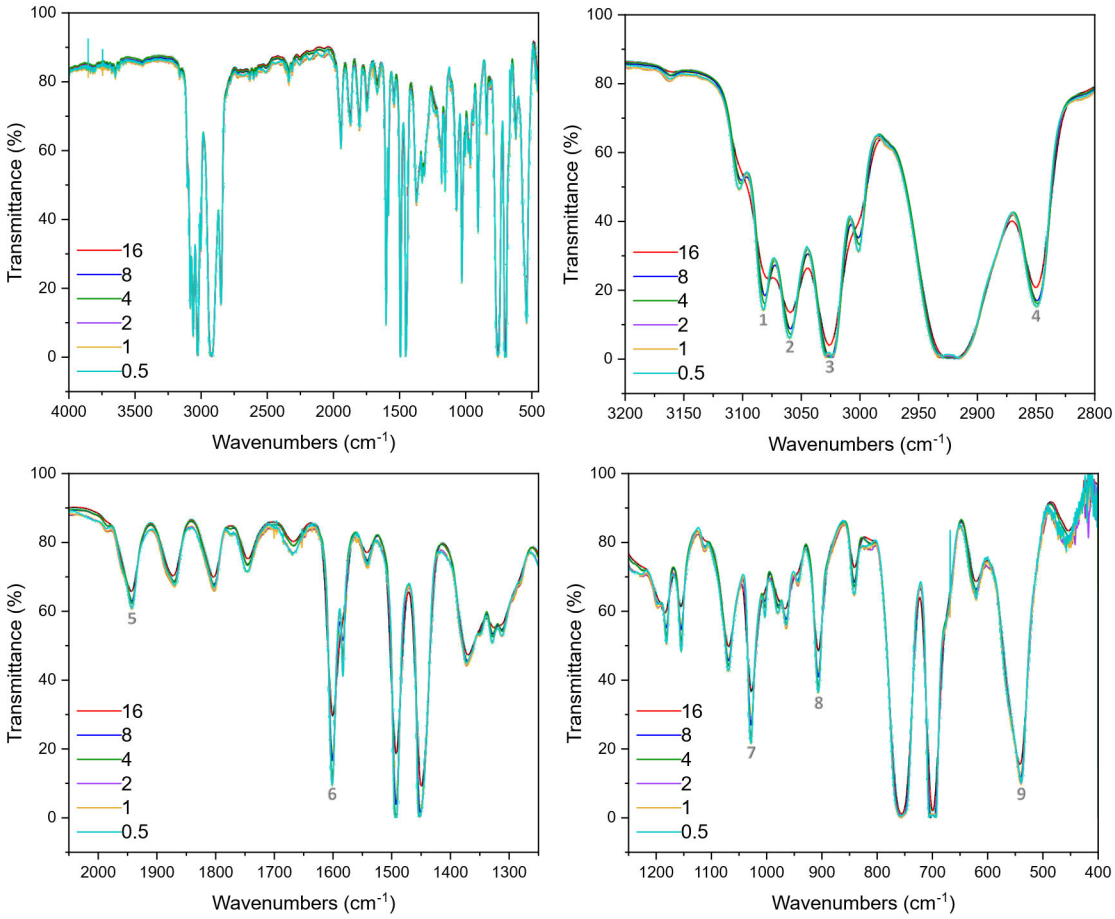


Figure B.3 Transmission FT-IR spectra of PS collected on a Shimadzu IRTracer-100 with varied spectral resolutions from 16– 0.5 cm^{-1}. Numbering denotes peaks in analysis.

Table B-6 Peak positions (cm^{-1})[ɪ] of PS collected on a Shimadzu IRTracer-100 FT-IR at variable spectral resolutions. [ɪ]Wavenumbers were determined in OMNIC using the standard peak picking function. [ǂ]NR denotes peak that were unresolved at said resolution.

	16 cm^{-1}	**8 cm^{-1}**	**4 cm^{-1}**	**2 cm^{-1}**	**1 cm^{-1}**	**0.5 cm^{-1}**
Peak 1	NR [ǂ]	3081.04	3081.36	3082.39	3082.26	3082.42
Peak 2	NR	3059.27	3059.22	3060.17	3060.08	3059.97
Peak 3	NR	3025.24 [lobed]	3023.40 [lobed]	3023.19 [lobed]	3024.24 [lobed]	3024.39 [lobed]
Peak 4	2850.15	2849.18	2848.95	2849.79	2849.59	2849.21
Peak 5	1943.76	1942.60	1942.38	1942.69	1942.63	1942.51
Peak 6	1600.47	1600.83	1600.88	1601.31	1601.19	1601.26
Peak 7	1027.32	1028.09	1028.26	1028.38	1028.24	1028.25
Peak 8	906.39	906.44	906.38	906.62	906.65	906.58
Peak 9	541.55	540.02	539.51	539.57	539.64	539.62

Table B-7 Peak position (cm^{-1})[ɪ] as a function of resolution for PS collected on a Shimadzu IRTracer-100 FT-IR, as assessed by calculating the difference in assigned peak value from the value determined at 0.5 cm^{-1} (e.g. $\Delta 16$ cm^{-1} = $peak_{0.5cm-1} - peak_{16cm-1}$). [ɪ]See Table B-6 for raw data. [ǂ]NR denotes peak that were unresolved at said resolution.

	Δ16 cm^{-1}	**Δ8 cm^{-1}**	**Δ4 cm^{-1}**	**Δ2 cm^{-1}**	**Δ1 cm^{-1}**	**Δ0.5 cm^{-1}**
Peak 1	NR [ǂ]	1.38	1.06	0.03	0.16	0
Peak 2	NR	0.7	0.75	-0.20	-0.11	0
Peak 3 (lobed)	NR	-0.85	0.99	1.20	0.15	0
Peak 4	-0.94	0.03	0.26	-0.58	-0.38	0
Peak 5	-1.25	-0.09	0.13	-0.18	-0.12	0
Peak 6	0.79	0.43	0.38	-0.05	0.07	0
Peak 7	0.93	0.16	-0.01	-0.13	0.01	0
Peak 8	0.19	0.14	0.20	-0.04	-0.07	0
Peak 9	-1.93	-0.40	0.11	0.05	-0.02	0
Average |Δ|	**1.00**	**0.46**	**0.43**	**0.27**	**0.12**	**-**

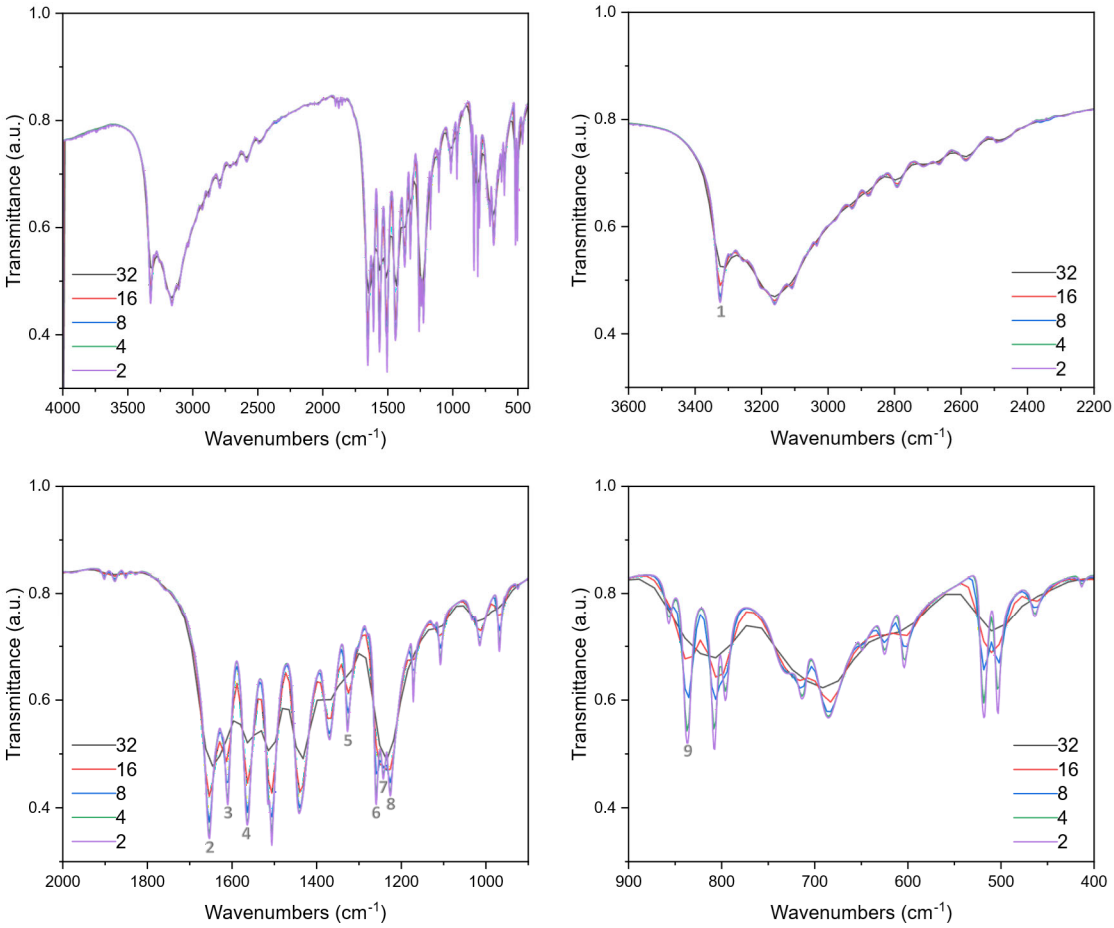


Figure B.4 Transmission FT-IR spectra of APAP collected on a Bruker Alpha II with varied spectral resolutions from 32 – 0.5 cm^{-1}. Numbering denotes peaks in analysis.

Table B-8 Peak positions (cm^{-1})[ɪ] of APAP collected on a Bruker Alpha II FT-IR at variable spectral resolutions. [ɪ]Wavenumbers were determined in OMNIC using the standard peak picking function. [ǂ]NR denotes peak that were unresolved at said resolution.

	32 cm^{-1}	**16 cm^{-1}**	**8 cm^{-1}**	**4 cm^{-1}**	**2 cm^{-1}**
Peak 1	3315.06	3322.55	3324.15	3324.59	3324.68
Peak 2	NR [ǂ]	1652.87	1653.82	1654.09	1653.64
Peak 3	NR	1614.07	1610.98	1610.51	1610.18
Peak 4	1560.27	1562.47	1563.30	1563.45	1563.80
Peak 5	NR	1324.72	1325.37	1326.53	1327.03
Peak 6	NR	NR	1257.30	1258.89	1259.40
Peak 7	NR	NR	1241.57	1242.14	1242.53
Peak 8	NR	NR	1226.15	1225.96	1225.94
Peak 9	NR	835.88	836.41	836.82	836.78

Table B-9 Peak position (cm-1)[ɪ] as a function of resolution for APAP collected on a Bruker Alpha II FT-IR, as assessed by calculating the difference in assigned peak value from the value determined at 2 cm^{-1} (e.g. $\Delta 32\ cm^{-1} = peak_{2cm\text{-}1} - peak_{32cm\text{-}1}$). [ɪ]See Table B-8 for raw data. [ǂ]NR denotes peak that were unresolved at said resolution.

	Δ32 cm^{-1}	**Δ16 cm^{-1}**	**Δ8 cm^{-1}**	**Δ4 cm^{-1}**	**Δ2 cm^{-1}**
Peak 1	9.62	2.13	0.53	0.09	0
Peak 2	NR [ǂ]	0.77	-0.18	-0.45	0
Peak 3	NR	-3.89	-0.80	-0.33	0
Peak 4	3.53	1.33	0.50	0.35	0
Peak 5	NR	2.31	1.66	0.50	0
Peak 6	NR	NR	2.10	0.51	0
Peak 7	NR	NR	0.96	0.39	0
Peak 8	NR	NR	-0.21	-0.02	0
Peak 9	NR	0.9	0.37	-0.04	0
Average |Δ|	**6.58**	**1.89**	**0.81**	**0.30**	**-**

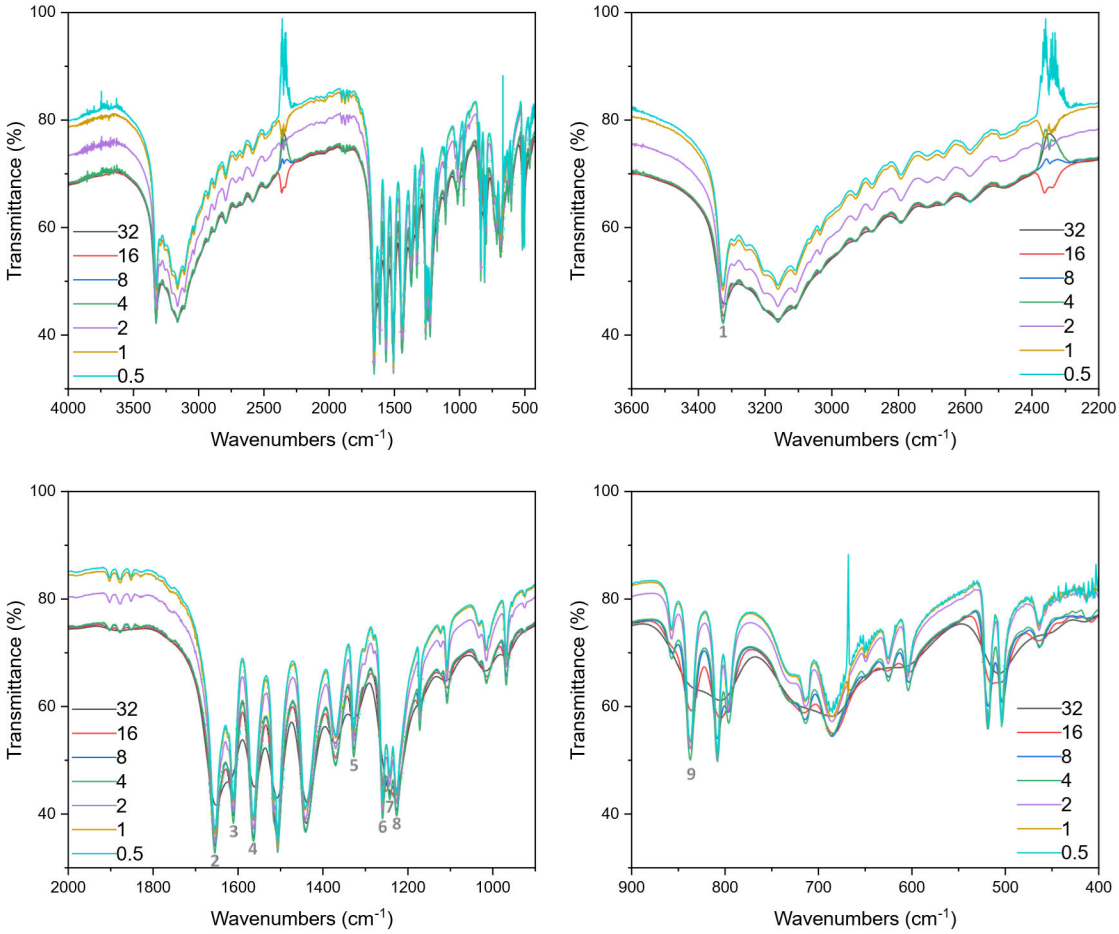


Figure B.5 Transmission FT-IR spectra of APAP collected on a Perkin Elmer Frontier with varied spectral resolutions from 32 – 0.5 cm^{-1}. Numbering denotes peaks in analysis.

Table B-10 Peak positions (cm^{-1})[ɪ] of APAP collected on a PerkinElmer Frontier FT-IR at variable spectral resolutions. [ɪ]Wavenumbers were determined in OMNIC using the standard peak picking function. [ǂ]NR denotes peak that were unresolved at said resolution.

	32 cm^{-1}	**16 cm^{-1}**	**8 cm^{-1}**	**4 cm^{-1}**	**2 cm^{-1}**	**1 cm^{-1}**	**0.5 cm^{-1}**
Peak 1	3319.20	3324.65	3325.79	3326.14	3326.45	3326.27	3326.17
Peak 2	NR [ǂ]	1653.94	1654.54	1654.79	1654.51	1653.41	1654.25
Peak 3	NR	1613.25	1611.49	1610.90	1610.82	1610.63	1610.81
Peak 4	1560.22	1563.57	1563.58	1563.45	1564.21	1564.46	1564.06
Peak 5	1330.62	1325.43	1326.24	1327.10	1327.60	1327.74	1327.65
Peak 6	NR	NR	1258.29	1259.49	1259.97	1260.00	1259.96
Peak 7	NR	NR	1242.06	1242.58	1242.99	1243.08	1243.05
Peak 8	NR	NR	1226.18	1226.26	1226.33	1226.22	1226.19
Peak 9	NR	835.97	836.93	837.20	837.21	836.66	836.42

Table B-11 Peak position (cm^{-1})[ɪ] as a function of resolution for APAP collected on a PerkinElmer Frontier FT-IR, as assessed by calculating the difference in assigned peak value from the value determined at 0.5 cm^{-1} (e.g. $\Delta 32\ cm^{-1} = peak_{0.5cm-1} - peak_{32cm-1}$). [ɪ]See Table B-10 for raw data. [ǂ]NR denotes peak that were unresolved at said resolution.

	Δ32 cm^{-1}	**Δ16 cm^{-1}**	**Δ8 cm^{-1}**	**Δ4 cm^{-1}**	**Δ2 cm^{-1}**	**Δ1 cm^{-1}**	**Δ0.5 cm^{-1}**
Peak 1	6.97	1.52	0.38	0.03	-0.28	-0.10	0
Peak 2	NR [ǂ]	0.31	-0.29	-0.54	-0.26	0.84	0
Peak 3	NR	-2.44	-0.68	-0.09	-0.01	0.18	0
Peak 4	3.84	0.49	0.48	0.61	-0.15	-0.4	0
Peak 5	-2.97	2.22	1.41	0.55	0.05	-0.09	0
Peak 6	NR	NR	1.67	0.47	-0.01	-0.04	0
Peak 7	NR	NR	0.99	0.47	0.06	-0.03	0
Peak 8	NR	NR	0.01	-0.07	-0.14	-0.03	0
Peak 9	NR	0.45	-0.51	-0.78	-0.79	-0.24	0
Average |Δ|	**4.59**	**1.24**	**0.71**	**0.40**	**0.19**	**0.22**	**-**

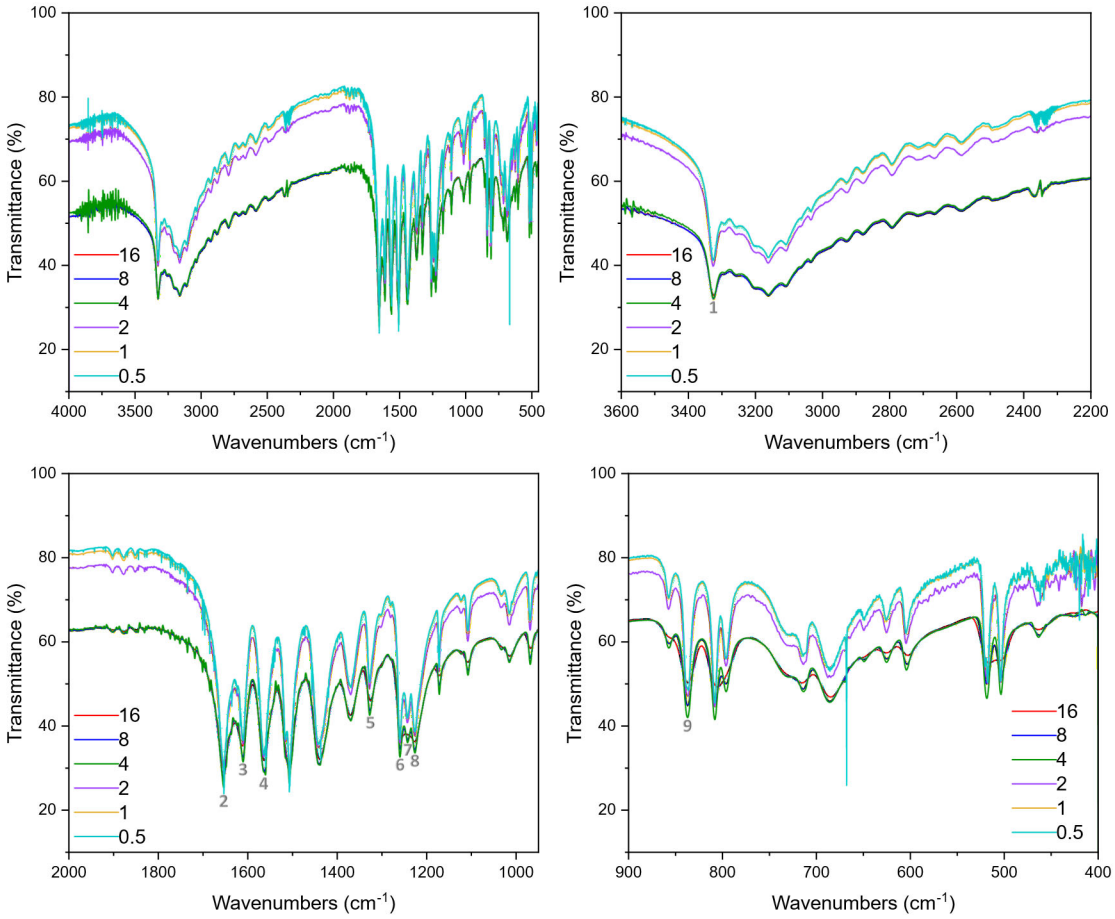


Figure B.6 Transmission FT-IR spectra of APAP collected on a Shimadzu IRTracer-100 with varied spectral resolutions from 32 – 0.5 cm^{-1}. Numbering denotes peaks in analysis.

Table B-12 Peak positions (cm^{-1})[ɪ] of APAP collected on a Shimadzu IRTracer-100 FT-IR at variable spectral resolutions. [ɪ]Wavenumbers were determined in OMNIC using the standard peak picking function. [ǂ]NR denotes peak that were unresolved at said resolution. *Denotes water interference.

	16 cm^{-1}	**8 cm^{-1}**	**4 cm^{-1}**	**2 cm^{-1}**	**1 cm^{-1}**	**0.5 cm^{-1}**
Peak 1	3324.70	3325.20	3325.35	3326.44	3325.74	3326.41
Peak 2	1653.76	1654.07	1653.98*	1653.45*	1653.01*	1653.28*
Peak 3	1612.11	1610.99	1610.52*	1610.48*	1610.52*	1610.53*
Peak 4	1563.34	1562.72	1563.72*	1564.62*	1564.79*	1564.89*
Peak 5	1325.41	1326.55	1327.28	1327.71	1327.66	1327.4
Peak 6	NR [ǂ]	1258.88	1259.57	1259.93	1259.96	1260.15
Peak 7	NR	1242.25	1242.70	1243.03	1243.06	1243.03
Peak 8	NR	1226.12	1226.16	1226.31	1226.25	1225.97
Peak 9	836.71	837.04	837.13	836.90	836.45	836.42

Table B-13 Peak position (cm^{-1})[ɪ] as a function of resolution for APAP collected on a Shimadzu IRTracer-100 FT-IR, as assessed by calculating the difference in assigned peak value from the value determined at 0.5 cm^{-1} (e.g.Δ16 cm^{-1} = $peak_{0.5cm\text{-}1}$ – $peak_{16cm\text{-}1}$). [ɪ]See Table B-12 for raw data. [ǂ]NR denotes peak that were unresolved at said resolution. *Denotes water interference.

	Δ16 cm^{-1}	**Δ8 cm^{-1}**	**Δ4 cm^{-1}**	**Δ2 cm^{-1}**	**Δ1 cm^{-1}**	**Δ0.5 cm^{-1}**
Peak 1	1.71	1.21	1.06	-0.03	0.67	0
Peak 2	-0.48	-0.79	-0.70*	-0.17*	0.27*	0
Peak 3	-1.58	-0.46	0.01*	0.05*	0.01*	0
Peak 4	1.55	2.17	1.17*	0.27*	0.10*	0
Peak 5	1.99	0.85	0.12	-0.31	-0.26	0
Peak 6	NR [ǂ]	1.27	0.58	0.22	0.19	0
Peak 7	NR	0.78	0.33	0.00	-0.03	0
Peak 8	NR	-0.15	-0.19	-0.34	-0.28	0
Peak 9	-0.29	-0.62	-0.71	-0.48	-0.03	0
Average |Δ|	**1.27**	**0.92**	**0.54**	**0.21**	**0.20**	**-**

B.2.3. Variable Instrument Transmission FT-IR, with Native Software Analysis

Table B-14 Peak positions (cm^{-1})[ǂ] of PS collected on a Bruker Alpha II FT-IR at variable spectral resolutions. [ǂ]Wavenumbers were determined in OPUS using the standard peak picking function. [ǂ]NR denotes peak that were unresolved at said resolution.

	32 cm^{-1}	**16 cm^{-1}**	**8 cm^{-1}**	**4 cm^{-1}**	**2 cm^{-1}**
Peak 1	NR [ǂ]	NR	3080.37	3081.41	3081.54
Peak 2	NR	NR	3059.39	3059.39	3059.37
Peak 3	NR	NR	3025.85	3025.46	3025.65
Peak 4	NR	2851.75	2849.70	2849.14	2849.03
Peak 5	1945.59	1944.75	1943.02	1942.43	1942.29
Peak 6	1596.12	1598.77	1600.56	1600.83	1600.82
Peak 7	1027.47	1026.45	1027.54	1028.11	1028.08
Peak 8	907.83	906.12	906.36	906.29	906.25
Peak 9	546.35	543.55	540.61	539.60	539.28

Table B-15 Peak position (cm^{-1})[ǂ] as a function of resolution for PS collected on a Bruker Alpha II FT-IR, as assessed by calculating the difference in assigned peak value from the value determined at 2 cm^{-1} (e.g. $\Delta 32$ cm^{-1} = $peak_{2cm-1}$ – $peak_{32cm-1}$). [ǂ]See Table B-14 for raw data. [ǂ]NR denotes peak that were unresolved at said resolution.

	Δ32 cm^{-1}	**Δ16 cm^{-1}**	**Δ8 cm^{-1}**	**Δ4 cm^{-1}**	**Δ2 cm^{-1}**
Peak 1	NR [ǂ]	NR	1.17	0.13	0
Peak 2	NR	NR	-0.02	-0.02	0
Peak 3	NR	NR	-0.20	0.19	0
Peak 4	NR	-2.72	-0.67	-0.11	0
Peak 5	-3.30	-2.46	-0.73	-0.14	0
Peak 6	4.70	2.05	0.26	-0.01	0
Peak 7	0.61	1.63	0.54	-0.03	0
Peak 8	-1.58	0.13	-0.11	-0.04	0
Peak 9	-7.07	-4.27	-1.33	-0.32	0
Average |Δ|	**3.45**	**2.21**	**0.56**	**0.11**	**-**

Table B-16 Peak positions (cm^{-1})[ǂ] of PS collected on a PerkinElmer Frontier FT-IR at variable spectral resolutions. [ǂ]Wavenumbers were determined in Spectrum using the standard peak picking function. [ǂ]NR denotes peak that were unresolved at said resolution.

	32 cm^{-1}	**16 cm^{-1}**	**8 cm^{-1}**	**4 cm^{-1}**	**2 cm^{-1}**	**1 cm^{-1}**	**0.5 cm^{-1}**
Peak 1	NR [ǂ]	NR	3081.78	3082.23	3082.65	3082.76	3082.73
Peak 2	NR	NR	3060.19	3060.17	3060.44	3060.50	3060.40
Peak 3	NR	NR	3026.37	3026.09	3026.28	3025.57	3025.45
Peak 4	2857.30	2851.41	2850.16	2849.80	2849.96	2849.97	2849.91
Peak 5	1946.06	1944.48	1943.25	1942.98	1943.06	1943.03	1943.30
Peak 6	1597.72	1600.71	1601.37	1601.44	1601.49	1601.51	1601.49
Peak 7	1026.57	1027.32	1028.28	1028.56	1028.50	1028.37	1028.32
Peak 8	905.90	906.67	906.70	906.64	906.73	906.74	906.76
Peak 9	544.31	542.02	540.14	539.56	539.42	539.21	539.09

Table B-17 Peak position (cm^{-1})[ǂ] as a function of resolution for PS collected on a PerkinElmer Frontier FT-IR, as assessed by calculating the difference in assigned peak value from the value determined at 0.5 cm^{-1} (e.g. $\Delta 32$ cm^{-1} = $peak_{0.5cm-1} - peak_{32cm-1}$). [ǂ]See Table B-16 for raw data. [ǂ]NR denotes peak that were unresolved at said resolution.

	Δ32 cm^{-1}	**Δ16 cm^{-1}**	**Δ8 cm^{-1}**	**Δ4 cm^{-1}**	**Δ2 cm^{-1}**	**Δ1 cm^{-1}**	**Δ0.5 cm^{-1}**
Peak 1	NR [ǂ]	NR	0.95	0.50	0.08	-0.03	0
Peak 2	NR	NR	0.21	0.23	-0.04	-0.10	0
Peak 3	NR	NR	-0.92	-0.64	-0.83	-0.12	0
Peak 4	-7.39	-1.50	-0.25	0.11	-0.05	-0.06	0
Peak 5	-2.76	-1.18	0.05	0.32	0.24	0.27	0
Peak 6	3.77	0.78	0.12	0.05	0.00	-0.02	0
Peak 7	1.75	1.00	0.04	-0.24	-0.18	-0.05	0
Peak 8	0.86	0.09	0.06	0.12	0.03	0.02	0
Peak 9	-5.22	-2.93	-1.05	-0.47	-0.33	-0.12	0
Average |Δ|	**3.63**	**1.25**	**0.41**	**0.30**	**0.20**	**0.09**	**-**

Table B-18 Peak positions (cm^{-1})[I] of PS collected on a Shimadzu IRTracer-100 FT-IR at variable spectral resolutions. [I]Wavenumbers were determined in LabSolutions using the standard peak picking function. [ǂ]NR denotes peak that were unresolved at said resolution.

	16 cm^{-1}	**8 cm^{-1}**	**4 cm^{-1}**	**2 cm^{-1}**	**1 cm^{-1}**	**0.5 cm^{-1}**
Peak 1	NR [ǂ]	3081.28	3081.28	3082.30	3082.23	3082.39
Peak 2	NR	3059.10	3059.10	3060.12	3060.05	3059.97
Peak 3	NR	3025.35 [lobed]	3023.42 [lobed]	3023.23 [lobed]	3024.25 [lobed]	3024.42 [lobed]
Peak 4	2850.79	2848.86	2848.86	2849.87	2849.59	2849.59
Peak 5	1944.25	1942.32	1942.32	1942.59	1942.64	1942.49
Peak 6	1600.92	1600.92	1600.92	1601.43	1601.15	1601.25
Peak 7	1028.06	1028.06	1028.06	1028.32	1028.22	1028.23
Peak 8	906.54	906.54	906.54	906.56	906.71	906.61
Peak 9	542.00	540.07	539.59	539.60	539.78	539.64

Table B-19 Peak position (cm^{-1})[I] as a function of resolution for PS collected on a Shimadzu IRTracer-100 FT-IR, as assessed by calculating the difference in assigned peak value from the value determined at 0.5 cm^{-1} (e.g. $\Delta 16$ cm^{-1} = $peak_{0.5cm-1} - peak_{16cm-1}$). [I]See Table B-18 for raw data. [ǂ]NR denotes peak that were unresolved at said resolution.

	Δ16 cm^{-1}	**Δ8 cm^{-1}**	**Δ4 cm^{-1}**	**Δ2 cm^{-1}**	**Δ1 cm^{-1}**	**Δ0.5 cm^{-1}**
Peak 1	NR [ǂ]	1.11	1.11	0.09	0.16	0
Peak 2	NR	0.87	0.87	-0.15	-0.08	0
Peak 3	NR	-0.93	1.00	1.19	0.17	0
Peak 4	-1.2	0.73	0.73	-0.28	0.00	0
Peak 5	-1.76	0.17	0.17	-0.10	-0.15	0
Peak 6	0.33	0.33	0.33	-0.18	0.10	0
Peak 7	0.17	0.17	0.17	-0.09	0.01	0
Peak 8	0.07	0.07	0.07	0.05	-0.10	0
Peak 9	-2.36	-0.43	0.05	0.04	-0.14	0
Average |Δ|	**0.98**	**0.53**	**0.50**	**0.24**	**0.10**	**-**

Table B-20 Peak positions (cm^{-1})[ɪ] of APAP collected on a Bruker Alpha II FT-IR at variable spectral resolutions. [ɪ]Wavenumbers were determined in OPUS using the standard peak picking function. [ǂ]NR denotes peak that were unresolved at said resolution.

	32 cm^{-1}	**16 cm^{-1}**	**8 cm^{-1}**	**4 cm^{-1}**	**2 cm^{-1}**
Peak 1	3316.19	3322.83	3324.26	3324.62	3324.7
Peak 2	NR [ǂ]	1653.06	1653.84	1654.10	1653.57
Peak 3	NR	1613.51	1610.91	1610.46	1610.17
Peak 4	1560.42	1562.52	1563.30	1563.44	1563.83
Peak 5	NR	1324.58	1325.50	1326.60	1327.08
Peak 6	NR	NR	1257.47	1259.00	1259.43
Peak 7	NR	NR	1241.65	1242.15	1242.57
Peak 8	NR	NR	1225.98	1225.96	1225.93
Peak 9	NR	836.00	836.50	836.82	836.77

Table B-21 Peak position (cm^{-1})[ɪ] as a function of resolution for APAP collected on a Bruker Alpha II FT-IR, as assessed by calculating the difference in assigned peak value from the value determined at 0.5 cm^{-1} (e.g. $\Delta 32\ cm^{-1} = peak_{0.5cm-1} - peak_{32cm-1}$). [ɪ]See Table B-20 for raw data. [ǂ]NR denotes peak that were unresolved at said resolution.

	Δ32 cm^{-1}	**Δ16 cm^{-1}**	**Δ8 cm^{-1}**	**Δ4 cm^{-1}**	**Δ2 cm^{-1}**
Peak 1	8.51	1.87	0.44	0.08	0
Peak 2	NR [ǂ]	0.51	-0.27	-0.53	0
Peak 3	NR	-3.34	-0.74	-0.29	0
Peak 4	3.41	1.31	0.53	0.39	0
Peak 5	NR	2.50	1.58	0.48	0
Peak 6	NR	NR	1.96	0.43	0
Peak 7	NR	NR	0.92	0.42	0
Peak 8	NR	NR	-0.05	-0.03	0
Peak 9	NR	0.77	0.27	-0.05	0
Average |Δ|	**5.96**	**1.72**	**0.75**	**0.30**	**-**

Table B-22 Peak positions (cm^{-1})[ɪ] of APAP collected on a PerkinElmer Frontier FT-IR at variable spectral resolutions. [ɪ]Wavenumbers were determined in Spectrum using the standard peak picking function. [ǂ]NR denotes peak that were unresolved at said resolution.

	32 cm^{-1}	**16 cm^{-1}**	**8 cm^{-1}**	**4 cm^{-1}**	**2 cm^{-1}**	**1 cm^{-1}**	**0.5 cm^{-1}**
Peak 1	3321.73	3325.15	3325.93	3326.17	3326.46	3326.26	3326.16
Peak 2	NR [ǂ]	1654.11	1654.4	1654.68	1654.27	1653.47	1654.24
Peak 3	NR	1612.66	1611.32	1610.88	1610.82	1610.62	1610.69
Peak 4	1561.40	1563.43	1563.46	1563.49	1564.23	1564.53	1564.05
Peak 5	1326.70	1325.35	1326.51	1327.27	1327.69	1327.76	1327.74
Peak 6	NR	NR	1258.82	1259.67	1259.96	1260.00	1259.98
Peak 7	NR	NR	1242.28	1242.70	1243.00	1243.07	1243.05
Peak 8	NR	NR	1226.15	1226.27	1226.35	1226.29	1226.24
Peak 9	NR	836.30	837.01	837.22	837.20	836.54	836.43

Table B-23 Peak position (cm^{-1})[ɪ] as a function of resolution for APAP collected on a PerkinElmer Frontier FT-IR, as assessed by calculating the difference in assigned peak value from the value determined at 0.5 cm^{-1} (e.g. $\Delta 32\ cm^{-1} = peak_{0.5cm\text{-}1} - peak_{32cm\text{-}1}$). [ɪ]See Table B-22 for raw data. [ǂ]NR denotes peak that were unresolved at said resolution.

	Δ32 cm^{-1}	**Δ16 cm^{-1}**	**Δ8 cm^{-1}**	**Δ4 cm^{-1}**	**Δ2 cm^{-1}**	**Δ1 cm^{-1}**	**Δ0.5 cm^{-1}**
Peak 1	4.43	1.01	0.23	0.01	-0.30	0.10	0
Peak 2	NR [ǂ]	0.13	-0.16	-0.44	-0.03	0.77	0
Peak 3	NR	-1.97	-0.63	-0.19	-0.13	0.07	0
Peak 4	2.65	0.62	0.59	0.56	-0.18	-0.48	0
Peak 5	1.04	2.39	1.23	0.47	0.05	-0.02	0
Peak 6	NR	NR	1.16	0.31	0.02	-0.02	0
Peak 7	NR	NR	0.77	0.35	0.05	-0.02	0
Peak 8	NR	NR	0.09	-0.03	-0.11	-0.05	0
Peak 9	NR	0.13	-0.58	-0.79	-0.77	-0.11	0
Average |Δ|	**2.71**	**1.04**	**0.60**	**0.35**	**0.18**	**0.18**	**-**

Table B-24 Peak positions (cm^{-1})[ŧ] of APAP collected on a Shimadzu IRTracer-100 FT-IR at variable spectral resolutions. [ŧ]Wavenumbers were determined in LabSolutions using the standard peak picking function. [ǂ]NR denotes peak that were unresolved at said resolution. *Denotes water interference.

	16 cm^{-1}	**8 cm^{-1}**	**4 cm^{-1}**	**2 cm^{-1}**	**1 cm^{-1}**	**0.5 cm^{-1}**
Peak 1	3325.28	3325.28	3325.28	3326.54	3325.73	3326.42
Peak 2	1653.00	1653.96	1653.96*	1653.51*	1652.98*	1653.26*
Peak 3	1612.49	1610.56	1610.56*	1610.59*	1610.55*	1610.53*
Peak 4	1564.27	1562.34	NR*	1564.54*	1564.74*	1564.53*
Peak 5	1325.10	1327.03	1327.51	1327.77	1327.64	1327.4
Peak 6	NR [ǂ]	1258.55	1259.52	1260.02	1259.89	1260.14
Peak 7	NR	1242.16	1242.64	1243.14	1243.02	1243.02
Peak 8	NR	1225.76	1226.24	1226.27	1226.26	1225.97
Peak 9	837.11	837.11	837.11	836.88	836.43	836.4

Table B-25 Peak position (cm^{-1})[ŧ] as a function of resolution for APAP collected on a Shimadzu IRTracer-100 FT-IR, as assessed by calculating the difference in assigned peak value from the value determined at 0.5 cm^{-1} (e.g. $\Delta 16cm^{-1}$ = $peak_{0.5cm\text{-}1} - peak_{16cm\text{-}1}$). [ŧ]See Table B-24 for raw data. [ǂ]NR denotes peak that were unresolved at said resolution. *Denotes water interference.

	Δ16 cm^{-1}	**Δ8 cm^{-1}**	**Δ4 cm^{-1}**	**Δ2 cm^{-1}**	**Δ1 cm^{-1}**	**Δ0.5 cm^{-1}**
Peak 1	1.14	1.14	1.14	-0.12	0.69	0
Peak 2	0.26	-0.70	-0.70*	-0.25*	0.28*	0
Peak 3	-1.96	-0.03	-0.03*	-0.06*	-0.02*	0
Peak 4	0.26	2.19	NR*	-0.01*	-0.21*	0
Peak 5	2.30	0.37	-0.11	-0.37	-0.24	0
Peak 6	NR [ǂ]	1.59	0.62	0.12	0.25	0
Peak 7	NR	0.86	0.38	-0.12	0.00	0
Peak 8	NR	0.21	-0.27	-0.3	-0.29	0
Peak 9	-0.71	-0.71	-0.71	-0.48	-0.03	0
Average |Δ|	**1.11**	**0.87**	**0.50**	**0.20**	**0.22**	**-**

B.2.3. Variable Instrument ATR FT-IR, with OMNIC Software Analysis

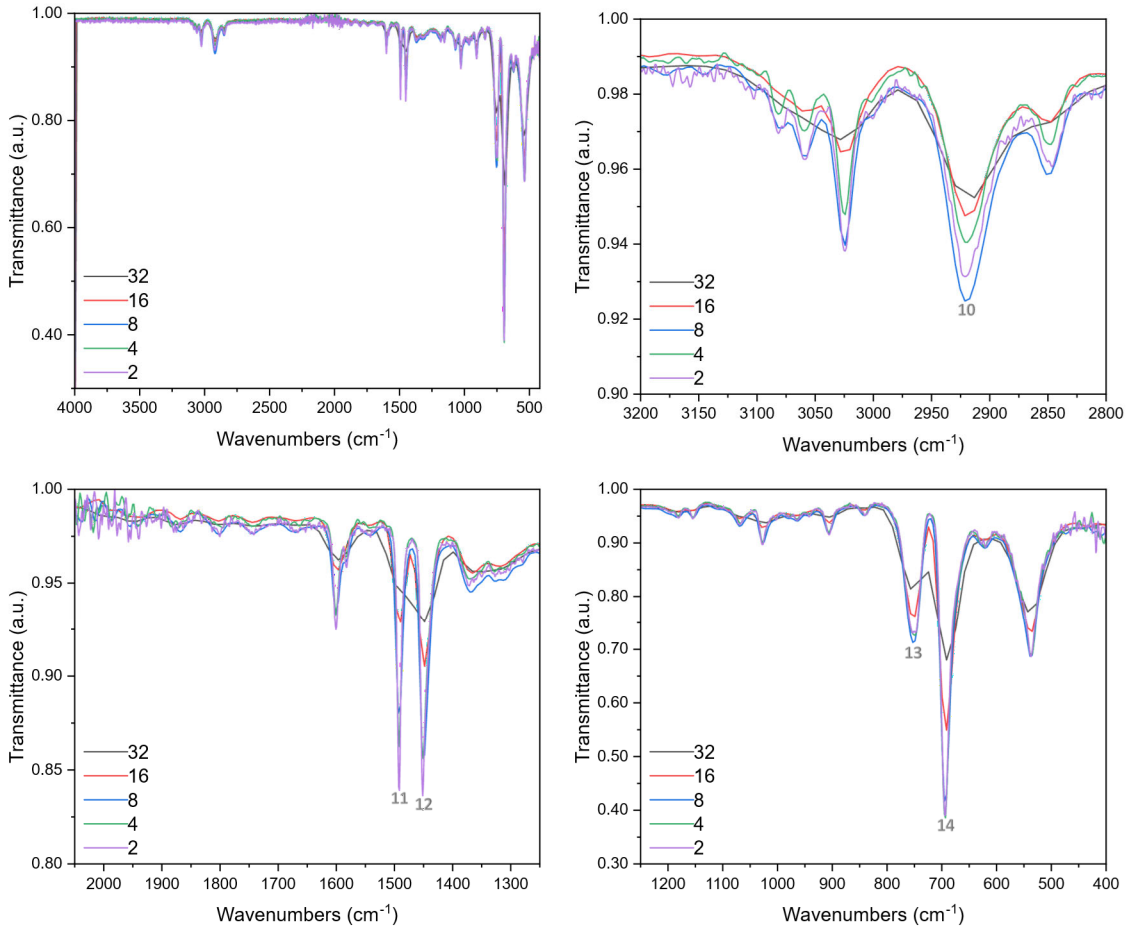


Figure B.7 ATR FT-IR spectra of PS collected on a Bruker Alpha II with varied spectral resolutions from 32 – 2 cm^{-1}. Numbering denotes peaks in analysis.

Table B-26 Peak positions (cm^{-1})[ǂ] of PS bands collected on a Bruker Alpha II FT-IR at variable spectral resolutions. [ǂ]Wavenumbers were determined in OMNIC using standard peak picking function. [ǂ]NR denotes peak that were unresolved at said resolution. *Peak pick value varies noticeably from the center of the peak.

	32 cm^{-1}	**16 cm^{-1}**	**8 cm^{-1}**	**4 cm^{-1}**	**2 cm^{-1}**
ATR					
Peak 10	2916.57	2918.71	2919.89	2920.16	2921.18
Peak 11	NR [ǂ]	1490.96	1491.91	1491.94	1491.92
Peak 12	1450.57	1448.10	1449.99	1450.89	1451.37
Peak 13	752.61	752.22	751.67	749.46*	753.18*
Peak 14	689.74	692.04	693.79	693.97	694.00
Transmission					
Peak 10	2919.21	2921.5	2923.05	2923.54	2923.59
Peak 11	NR	1491.58	1492.2	1492.45	1492.54
Peak 12	1453.47	1448.31	1449.60	1451.37	1451.90
Peak 13	755.53	756.28	755.59	756.33	756.53
Peak 14	699.54	698.63	699.24	698.42	698.87

Table B-27 Peak position (cm^{-1})[ɪ] as a function of resolution for PS bands collected on a Bruker Alpha II FT-IR, as assessed by calculating the difference in assigned peak value from the value determined at 2 cm^{-1} (e.g. Δ32 cm^{-1} = $peak_{2cm-1} - peak_{32cm-1}$). [ɪ]See Table B-26 for raw data. [ǂ]NR denotes peak that were unresolved at said resolution. *Peak pick value varies noticeably from the center of the peak.

	Δ32 cm^{-1}	**Δ16 cm^{-1}**	**Δ8 cm^{-1}**	**Δ4 cm^{-1}**	**Δ2 cm^{-1}**
ATR	4.61	2.47	1.29	1.02	0
Peak 10	NR [ǂ]	0.96	0.01	-0.02	0
Peak 11	0.80	3.27	1.38	0.48	0
Peak 12	0.57	0.96	1.51	3.72	0
Peak 13	4.26	1.96	0.21	0.03*	0*
Peak 14	4.61	2.47	1.29	1.02	0
Average |Δ|	**2.56**	**1.92**	**0.88**	**1.05**	**-**
Transmission					
Peak 10	4.38	2.09	0.54	0.05	0
Peak 11	NR	0.96	0.34	0.09	0
Peak 12	-1.57	3.59	2.30	0.53	0
Peak 13	1.00	0.25	0.94	0.20	0
Peak 14	-0.67	0.24	-0.37	0.45	0
Average |Δ|	**1.91**	**1.43**	**0.90**	**0.26**	**-**

B.2.4. Variable Instrument ATR FT-IR, with Native Software Analysis

Table B-28 Peak positions (cm^{-1})[ǂ] of PS bands collected on a Bruker Alpha II FT-IR at variable spectral resolutions. [ǂ]Wavenumbers were determined in OPUS using standard peak picking function. [ǂ]NR denotes peak that were unresolved at said resolution.*Peak pick value varies noticeably from the center of the peak.

	32 cm^{-1}	**16 cm^{-1}**	**8 cm^{-1}**	**4 cm^{-1}**	**2 cm^{-1}**
ATR					
Peak 10	2917.13	2918.74	2919.92	2920.22	2921.19
Peak 11	NR [ǂ]	1491.21	1491.89	1491.98	1491.91
Peak 12	1449.88	1448.18	1450.15	1450.99	1451.42
Peak 13	753.30	752.21	751.57	749.17*	753.24*
Peak 14	689.49	692.28	693.80	693.99	694.00
Transmission					
Peak 10	2919.73	2921.83	2923.13	2923.62	2923.59
Peak 11	NR	1491.87	1492.17	1492.47	1492.53
Peak 12	1452.70	1448.27	1449.85	1451.45	1451.92
Peak 13	756.35	756.14	755.60	756.39	756.54
Peak 14	698.80	698.64	699.31	697.46	698.86

Table B-29 Peak position (cm^{-1})[I] as a function of resolution for PS bands collected on a Bruker Alpha II FT-IR, as assessed by calculating the difference in assigned peak value from the value determined at 2 cm^{-1} (e.g. Δ32 cm^{-1} = $peak_{2cm-1} - peak_{32cm-1}$). [I]See Table B-28 for raw data. [ǂ]NR denotes peak that were unresolved at said resolution. *Peak pick value varies noticeably from the center of the peak.

	Δ32 cm^{-1}	**Δ16 cm^{-1}**	**Δ8 cm^{-1}**	**Δ4 cm^{-1}**	**Δ2 cm^{-1}**
ATR					
Peak 10	4.06	2.45	1.27	0.97	0
Peak 11	NR [ǂ]	0.70	0.02	-0.07	0
Peak 12	1.54	3.24	1.27	0.43	0
Peak 13	-0.06	1.03	1.67	4.07*	0*
Peak 14	4.51	1.72	0.20	0.01	0
Average |Δ|	**2.54**	**1.83**	**0.89**	**1.11**	**-**
Transmission					
Peak 10	3.86	1.76	0.46	-0.03	0
Peak 11	NR	0.66	0.36	0.06	0
Peak 12	-0.78	3.65	2.07	0.47	0
Peak 13	0.19	0.40	0.94	0.15	0
Peak 14	0.06	0.22	-0.45	1.40	0
Average |Δ|	**1.22**	**1.34**	**0.86**	**0.42**	**-**

B.2.5. Scan Number Effect

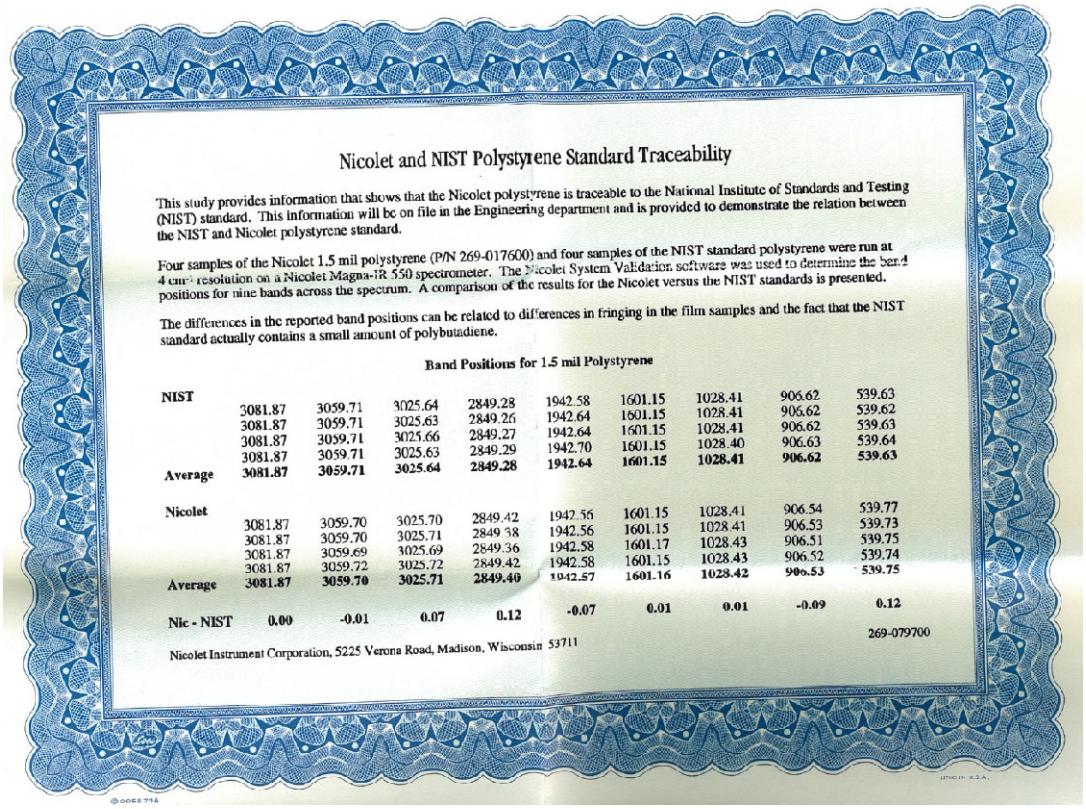
To investigate if 32 scans provided sufficient signal-to-noise, PS spectra were collected with variable scan numbers (Table B-30). The results demonstrate that whether collected with 1 scan or 256 scans, peak position accuracy is maintained. Therefore, 32 scans provide much more than adequate signal-to-noise to comment on peak position accuracy.

Table B-30 Peak position (cm^{-1})[I] of PS bands collected on a Nicolet iS50 FT-IR at variable scan numbers. Spectral resolution was 4 cm^{-1}. [I]Wavenumbers were determined in OMNIC using the standard peak picking function.

	1 scan	**4 scans**	**16 scans**	**32 scans**	**64 scans**	**128 scans**	**256 scans**	**Average Position (cm^{-1})**	**Stdv (±)**
Peak 1	3081.88	3081.89	3081.88	3081.88	3081.88	3081.89	3081.89	3081.88	0.01
Peak 2	3059.74	3059.75	3059.74	3059.74	3059.74	3059.75	3059.75	3059.74	0.01
Peak 3	3025.74	3025.78	3025.74	3025.75	3025.75	3025.75	3025.76	3025.75	0.01
Peak 4	2849.38	2849.39	2849.38	2849.38	2849.38	2849.39	2849.38	2849.38	0.00
Peak 5	1942.62	1942.59	1942.62	1942.61	1942.59	1942.66	1942.60	1942.61	0.02
Peak 6	1601.17	1601.17	1601.16	1601.16	1601.16	1601.16	1601.16	1601.16	0.00
Peak 7	1028.42	1028.42	1028.42	1028.42	1028.49	1028.42	1028.42	1028.43	0.03
Peak 8	906.46	906.53	906.51	906.51	906.52	906.51	906.52	906.51	0.02
Peak 9	539.67	539.62	539.67	539.71	539.67	539.62	539.67	539.66	0.03

B.3 Supplementary References

(1) Nicolet and NIST Polystyrene Standard Traceability Document.



Nicolet and NIST Polystyrene Standard Traceability

This study provides information that shows that the Nicolet polystyrene is traceable to the National Institute of Standards and Testing (NIST) standard. This information will be on file in the Engineering department and is provided to demonstrate the relation between the NIST and Nicolet polystyrene standard.

Four samples of the Nicolet 1.5 mil polystyrene (P/N 269-017600) and four samples of the NIST standard polystyrene were run at 4 cm^{-1} resolution on a Nicolet Magna-IR 550 spectrometer. The Nicolet System Validation software was used to determine the band positions for nine bands across the spectrum. A comparison of the results for the Nicolet versus the NIST standards is presented.

The differences in the reported band positions can be related to differences in fringing in the film samples and the fact that the NIST standard actually contains a small amount of polybutadiene.

Band Positions for 1.5 mil Polystyrene

NIST	3081.87	3059.71	3025.64	2849.28	1942.58	1601.15	1028.41	906.62	539.63
	3081.87	3059.71	3025.63	2849.26	1942.64	1601.15	1028.41	906.62	539.62
	3081.87	3059.71	3025.66	2849.27	1942.64	1601.15	1028.41	906.62	539.63
	3081.87	3059.71	3025.63	2849.29	1942.70	1601.15	1028.40	906.63	539.64
Average	**3081.87**	**3059.71**	**3025.64**	**2849.28**	**1942.64**	**1601.15**	**1028.41**	**906.62**	**539.63**
Nicolet	3081.87	3059.70	3025.70	2849.42	1942.56	1601.15	1028.41	906.54	539.77
	3081.87	3059.70	3025.71	2849.38	1942.56	1601.15	1028.41	906.53	539.73
	3081.87	3059.69	3025.69	2849.36	1942.58	1601.17	1028.43	906.51	539.75
	3081.87	3059.72	3025.72	2849.42	1942.58	1601.15	1028.43	906.52	539.74
Average	**3081.87**	**3059.70**	**3025.71**	**2849.40**	**1942.57**	**1601.16**	**1028.42**	**906.53**	**539.75**
Nic - NIST	**0.00**	**-0.01**	**0.07**	**0.12**	**-0.07**	**0.01**	**0.01**	**-0.09**	**0.12**

Nicolet Instrument Corporation, 5225 Verona Road, Madison, Wisconsin 53711

269-079700

Appendix C: *From Chapter 4* – Controlling Energetic Crystal Morphology Using Tailored Polymeric Additives

C.1 Supplementary Data

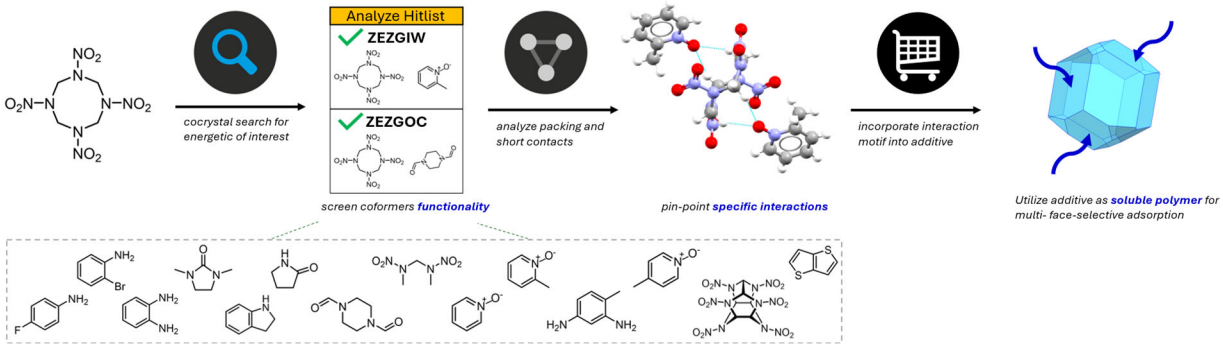
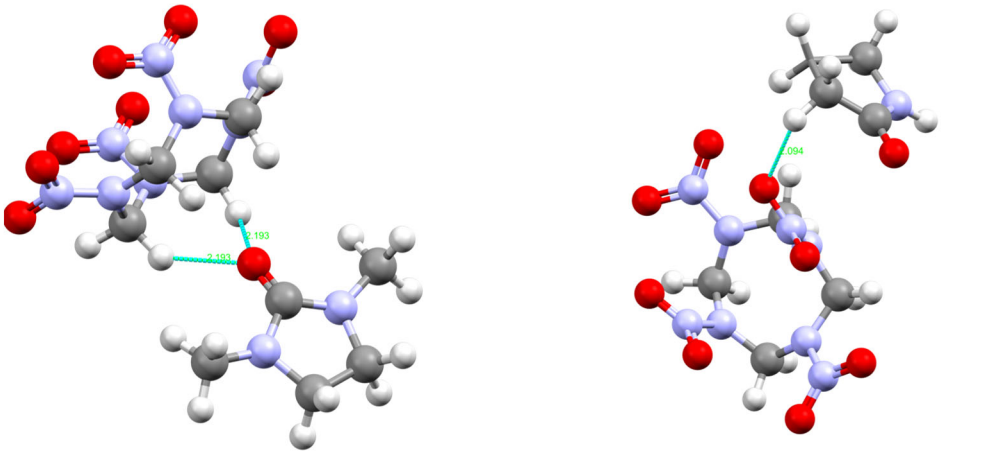


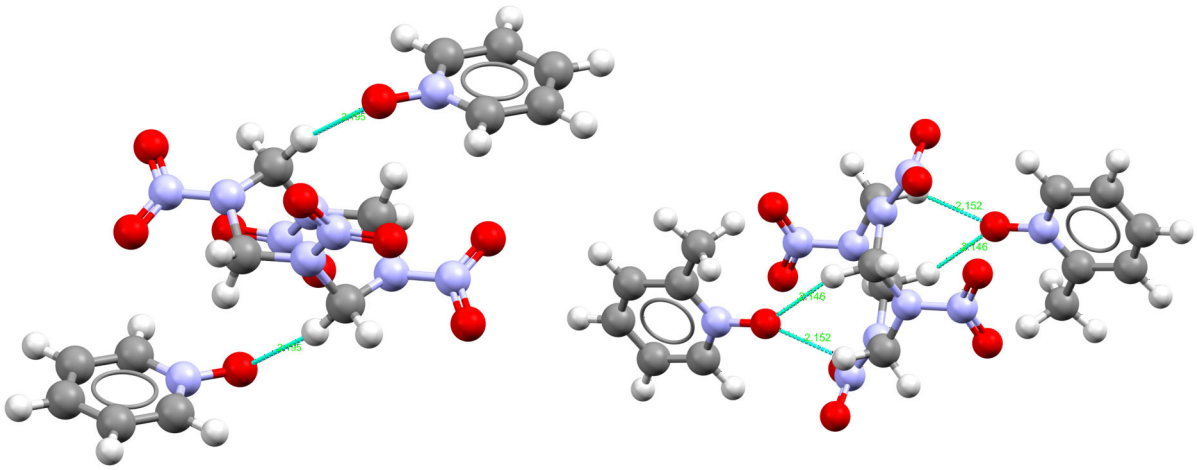
Figure C.1 Workflow for selecting additives, based on HMX cocrystal interaction screening.



1:1 HMX:1,3-dimethylimidazolidin-2-one (IDENEM)

1:1 HMX:pyrrolidin-2-one (ZEZGUI)

Figure C.2 Two HMX cocrystals (REFCODES) with pyrrolidone-based coformers were used to select the additive poly(vinylpyrrolidone) (PVP). The shortest contacts (highlighted in blue) suggest that dominant interactions will be the additive carbonyl with the energetic ring hydrogens (CH_2) and the carbonyl-adjacent CH_2 with the energetic nitro (NO_2) group.



1:1 HMX:pyridine N-oxide
(WEPTAP)

1:2 HMX:bis(2-picoline-N-oxide)
(ZEZGIW)

Figure C.3 Two HMX cocrystals (REFCODES) with N-oxide-based coformers were used to select the additive poly(2-vinylpyridine N-oxide) (P2VPNO). The shortest contacts (highlighted in blue) suggest that dominant interactions will be the additive N-oxide with the energetic ring hydrogens (CH_2). Note, a third HMX/N-oxide cocrystal does exist (ETOCOH) but no coordinates are available.